Morphological evolution and properties of epitaxial GaN nanowall network grown on c-sapphire

A Thesis

Submitted For the Degree of

DOCTOR OF PHILOSOPHY

in the Faculty of Science

by

Varun Thakur

CHEMISTRY AND PHYSICS OF MATERIALS UNIT

JAWAHARLAL NEHRU CENTRE FOR ADVANCED SCIENTIFIC RESEARCH

Bangalore – 560 064, India

JUNE 2016

Dedicated to my mother

DECLARATION

I hereby declare that the matter embodied in the thesis entitled "**Morphological evolution and properties of epitaxial GaN nanowall network grown on c-sapphire**" is the result of investigations carried out by me at the Chemistry and Physics of Materials Unit, Jawaharlal Nehru Centre for Advanced Scientific Research, Bangalore, India under the supervision of Prof. S. M. Shivaprasad and that it has not been submitted elsewhere for the award of any degree or diploma.

In keeping with the general practice in reporting scientific observations, due acknowledgement has been made whenever the work described is based on the findings of other investigators. Any omission that might have occurred by oversight or error of judgment is regretted.

Varun Thakur

CERTIFICATE

I hereby certify that the matter embodied in this thesis entitled "**Morphological evolution and properties of epitaxial GaN nanowall network grown on c-sapphire**" has been carried out by Mr. Varun Thakur at the Chemistry and Physics of Materials Unit, Jawaharlal Nehru Centre for Advanced Scientific Research, Bangalore, India under my supervision and that it has not been submitted elsewhere for the award of any degree or diploma.

Prof. S. M. Shivaprasad
(Research Supervisor)

Acknowledgements

I am fortunate to have wonderful lab mates who have maintained a healthy and cheerful atmosphere in the lab, Praveen, Manoj, Jithesh, Satish, Malleswar, Arpan, Sanjay, Dr. K. K. Nagaraja, Dr. Jay Ghatak, Shivakumar, Sandheep, Sachin, Prateek, Malathi and Aneesh. I have enjoyed many moments with them and will cherish them for many years to come.

Next, I acknowledge all the help and assistance provided by the technical staff without which no experiment would have been possible. Mr. Somashekhar and Mr. Sreenath have been the backbones of the lab who have helped tremendously in keeping the machines working, which in itself is an incredible feat. There are many more people who have helped me in characterizing the samples quickly and efficiently for which I am grateful: Mr. Vasu, Mr. Mahesh, Ms. Selvi, Mr. A. S. Rao, Prajwal, Jagadish. I'm also thankful to the administrative and academic staff who have been extremely helpful for any official assistance during the studentship, especially Mr. A. N. Jayachandra, Mrs. Sudha and Mrs. Sukanya. I acknowledge the library and computer lab staff for their help and support.

My friends have made my stay in JNC enjoyable, and I appreciate all their company and support: Pramod, Kanchan, Sananda, Laxmi, Arpan among many others with whom I have spent many precious moments. My Int. Ph.D. batchmates gave me excellent company over the years and I acknowledge all of them for their friendship: Arpan, Chidambar, Dileep, Gayatri, Pandeeswar, Rana, Sharma and Sudeshna. All my friends elsewhere are also acknowledged with whom I share many great memories. Last but not the least, I would like to thank my family for their support and encouragement, without which I would not be who I am today.

Synopsis

The advent of nanomaterials has heralded a new phase in research and development of novel structures which have been shown to have the potential for a multitude of applications. Their immense advantage over conventional flat films in various properties such as mobility, emission, endurance etc. have led to widespread applications in different fields. A host of nanostructures have been fabricated in this endeavor with nanowire based devices already in use. Another interesting morphology that has been reported for ZnO and GaN are nanowall structures which possess large surface area and have immense potential in sensing, photovoltaics and light emission, among other applications. Up till now, GaN based nanowall structures have only been fabricated using chemical means which suffers from high contamination and a lack of tunability. In this work, GaN nanowalls have been synthesized using plasma assisted molecular beam epitaxy by controlling the growth parameters. In a highly nitrogen rich environment with ultra high vacuum conditions, GaN nanowalls are fabricated on c-sapphire surfaces and characterized both *in-situ* as well as *ex-situ* by several complementary techniques. The nanowall structures formed using a physical method are cleaner and can be tuned more easily by changing the growth parameters. Several experiments are carried out in the course of this work, which have been divided into seven chapters:

Chapter I: This chapter introduces the reader to the field of solid state lighting and the advent of LEDs as the future illumination sources. Group III-N materials are at the forefront of LED technology and the advancements made in the III-N LED field are described briefly. The material properties of GaN are described with a focus on the lack of homoepitaxial substrates and the issue of resulting dislocations. The most commonly used growth techniques are discussed with the advantages and disadvantages of each being summarized.

Chapter II: The second chapter discusses the advancements made in the growth of GaN in a literature review. All the work carried out over the years by different groups on the improvement of GaN films using various growth methods are presented chronologically. From 1993, when the first GaN based LED was demonstrated, an intense amount of work has been done to improve both the internal and external quantum efficiency of LED structures. For internal quantum efficiency (IQE), the thrust areas have been to better the quality of GaN layers which suffers from a lack of suitable substrates. In this regard, techniques such as nitridation, buffer layers, ELOG etc. have been introduced which has steadily increased IQE values over the years. Similarly, EQE has been improved using surface plasmons, roughening, patterning among many other methods. Currently, nanostructures have been shown to improve both IQE as well as EQE since the commonly observed threading dislocations are filtered by them which improves crystal quality while higher surface area improves light extraction efficiency.

Chapter III: Here, we describe the experimental details of the work carried out in the thesis. The growth and characterization techniques used are elaborated and the working principle behind each is stated. Since the films were probed using three different kinds of characterizations, the chapter also splits the techniques based on their utility. Hence, the first section describes all the structural characterization techniques followed by optical and electrical. Some of the methods also contain specific signatures for GaN, such as Raman effect. A diagrammatic representation of the selection rules is shown for better understanding in this case.

Chapter IV: The first results chapter presents the details of the time dependent growth of GaN nanowall network films which were grown in nitrogen rich conditions using plasma assisted molecular beam epitaxy. The structural and optical quality of the films at low coverages ($<$ 100 nm) was poor, but improved significantly with growth time. The properties of a nanowall structure of thickness $\approx$ 600 nm were compared with other nanostructures and flat epilayer and it was observed that the photoluminescence of the band edge emission in nanowall structure was three orders of magnitude larger than flat epilayer with no defect related emission. Further, the structure showed very low stress levels, although interestingly there was a combination of biaxial and hydrostatic stress in the film, which is unusual for a wurtzite GaN film grown on c-sapphire since

such growth usually shows only biaxial stress. XPS studies carried out on two different nanowall morphologies also showed that nanowalls in general have a higher degree of charge transfer from Ga 4s to N 2p levels which stabilized the structure to a greater extent.

Chapter V: In the second results related chapter, we have explored two interesting properties of the GaN nanowall structure, electron transport and photoluminescence enhancement. Results of the electron transport measurements are discussed first followed by the PL enhancement efforts. A few initial studies on the electron transport in the GaN nanowalls indicated a higher mobility of electrons which was speculated to be confined in the apex regions of the nanowall since that is free of dislocations. In this regard, a few experiments were performed to probe these observations further. Magnetoresistance is directly proportional to mobility, and the mean free path of the electron can also be deduced from the data. It was observed that nanowall structures showed negative magnetoresistance which is related to disorder in the structure. Resistivity and photoconductivity measurements were also performed which also showed a high conductance and presence of trap states. Etching the film was carried out to ascertain the possible differences of the film properties at the apex and near the interface. It was observed that resistance and density of trap states increased with etching time, indicating that the film formed near the interface is more defective and the defects reduce higher up the walls. To enhance the band edge photoluminescence, two different methods were employed. The first was to nitride the substrate which improves the crystal quality and can potentially reduce the non radiative scattering centers in the film. The second method was to coat the film with metal nanoparticles to take advantage of surface plasmon coupling with the GaN excitons. Nitridation was carried out by exposing the clean c-sapphire surface to nitrogen plasma and the confirmation was gathered from RHEED pattern. A comparison between GaN grown on bare and nitrided c-sapphire surfaces showed that photoluminescence of GaN grown on nitrided c-sapphire was four times more than the GaN film grown on bare c-sapphire. Improvement of crystal quality and a lower strain was also deduced from HRXRD results. In the second experiment, Ag nanoparticles were coated on GaN films using electron beam evaporation and annealed in inert nitrogen atmosphere. Since metal nanoparticles can also scatter the excitonic

emission, getting the perfect configuration is needed to obtain enhancement. It was seen that after annealing the Ag-GaN structure to one particular temperature, the band edge emission increased by more than five times. There were no stabilizing agents used to cover the Ag nanoparticles and hence this structure is even better than what has been reported in literature.

Chapter VI: The Ag-GaN hybrid structure also holds promise as a SERS substrate. Different biomolecules and proteins were adsorbed to probe the SERS activity of the template and the results are presented in this chapter. Metal nanoparticles are commonly used to enhance the Raman signals from biomolecules since they can scatter the signals more effectively. This helps in detecting ultralow concentrations of analyte which has led to even single molecule detection. Nanostructured surfaces provide a very high surface area which can also improve the SERS activity of the template. In this experiment, as deposited configuration of Ag-GaN nanowall structure was first used to detect simple biomolecules such as thiophenol which gave encouraging results. SERS enhancement was much higher compared to a Ag-GaN epilayer surface and the signals were homogenously obtained at different spots on the surface. Further, the substrate could be reused which was another big advantage. FDTD simulations were also carried out and it was seen that GaN gives higher electromagnetic field intensity compared to Si and the nanowall configuration is better than flat layer in terms of the enhancement. The interparticle spacing between the Ag nanoparticles was 5 nm, which resulted in modest enhancement factors, but this large spacing was useful in detecting proteins. Two protein molecules with different pI levels were deposited independently on the Ag-GaN surface, and it was observed that in both the cases, SERS enhancement was observed. Since SERS templates are sensitive to the pI levels of the analyte, it was interesting to note that this template gave signals for proteins with widely different pI values. The second experiment was carried out using the templates from last chapter where the size and shape of Ag nanoparticles had been changed along with thickness of the GaN nanowalls. It was observed that thicker nanowalls gave a higher SERS intensity, but the thinner nanowalls were sensitive even after annealing to higher temperature. This was due to the way Ag deposited in both the cases, for thinner nanowalls most of the Ag nanoparticles adsorb on the sidewalls while on the thicker nanowalls Ag deposits only on the top surface. After

annealing to high temperatures, Ag on the top surface agglomerates and does not give any SERS signal, but Ag deposited on the sidewalls does not diffuse in the same way and hence still provides signal enhancements. Similar to the previous experiment, proteins were deposited on one of the samples which gave the highest SERS intensity and it was shown that the property of giving signals for varying pI levels held even in this case.

Chapter VII: The seventh and the last chapter summarizes the results drawn from each of the previous chapters. Important conclusions are drawn from each study that highlight some of the novel contributions of the thesis. Limitations of the experiments are also mentioned and some suggestions are given for future work in this direction.

Contents

List of Figures

List of Tables

Acronyms

BEE	Band Edge Emission
CVD	Chemical Vapor Deposition
EDS	Energy Dispersive X-ray Spectroscopy
EF	Enhancement Factor
FDTD	Finite Difference Time Domain
FESEM	Field Emission Scanning Electron Microscopy
FWHM	Full width at Half Maximum
HVPE	Hydride Vapor Phase Epitaxy
LED	Light Emitting Diode
LSPR	Localized Surface Plasmon Resonance
MBE	Molecular Beam Epitaxy
MOCVD	Metal Organic Chemical Vapor Deposition
PVD	Physical Vapor Deposition
QCTM	Quartz Crystal Thickness Monitor
RHEED	Reflection High Energy Electron Diffraction
SERS	Surface Enhanced Raman Spectroscopy
TDD	Threading Dislocation Density
UHV	Ultra High Vacuum
VLS	Vapor Liquid Solid
XPS	X-ray Photoelectron Spectroscopy
XRD	X-Ray Diffraction

Chapter 1

Introduction

1.1 Solid state lighting

The technological advancement to obtain high brightness sources is an ongoing and an important aspect of human development. From lighting the first fire millenia ago, mankind has been on a never ending quest to better technologies for brighter lighting sources. Since energy conservation is a big environmental concern, the world has most recently seen a gradual phasing out of the most popular incandescent light bulbs and the evolution of solid state lighting, a technology that utilizes the emission from semiconductor light emitting diodes (LEDs) to convert electricity to light in an efficient way. For comparison between various devices, lighting is typically quantified by its light output per unit energy put in. A typical measure of light output is *"lumen"*, defined as a unit of luminous flux equal to the light emitted in a unit solid angle by a uniform point source of one candela (cd) intensity. Candela is the base unit of luminous intensity in the international system of units (SI) that is equal to the luminous intensity in a given direction of a source which emits monochromatic radiation of frequency $540\text{x}10^{12}$ hertz and has a radiation intensity in that direction of $\frac{1}{683}$ watt per unit solid angle. Incandescent bulbs typically have an intensity of about 1200-1800 lumens while natural sunlight is about 1000-6000 lumens. In comparison to them, LEDs typically have an intensity of about 10-100 lumens which has confined their application in indication (e.g.

calculators, traffic lights) rather than illumination (e.g. reading lamp). Currently, for illumination purposes a bunch of LEDs are grouped together to achieve a reasonable intensity. The output depends on the current applied which in turn depends on the potential difference across the diode. Hence, the output is described in terms of radiant flux (R_f) and is expressed in milliwatts (mW) at a standard 20 mA current. In a solid state device, luminescence is achieved through excitation of electrons in a semiconductor using electricity whereas the more traditional incandescent bulbs use thermal radiation to generate light. This immediately shows a few advantages solid state devices have over the filament bulbs; the absence of a filament increases the lifespan of the device and a smaller mass provides higher resistance to shock and vibration. Some more advantages of solid state lighting are:

Long life - Compared to an incandescent bulb which provides about 1000 hours of life, an LED can provide more than 50,000 hours which reduces maintenance costs.

Energy savings - The best available white LEDs provide three times luminescence efficiency (lumens/watt) than incandescent sources. Colored LEDs eliminate the requirement of filters which provides further advantages in applications requiring colored lighting.

Quality - With minimum ultraviolet and infrared radiation, the quality of light is much better, and the colour is tunable.

Safety - LEDs operate at low voltages and are cool to touch, making their handling much safer, and applicability wider.

Smaller and flexible - Since LEDs have smaller sizes and can be fabricated in various structures, they are highly suited for lighting tight spaces and have unique applications.

There is already a widespread useage of LEDs in applications such as indicators, where brightness, visibility and long life are important. For instance, traffic lights and exit signs on major highways all over the world are gradually turning to LEDs improving the safety and convenience of drivers significantly. Other places where LEDs have found applications include lighting smaller areas such as decorations, displays, pathways, parking lots and even indoors. They have found widespread use for backlighting of televisions and cellular phones. As LEDs become more efficient, we would see them being applied in even more

places, possibly entire walls and ceilings being illuminated. There are three main ways by which solid state lighting is achieved; apart from the aforementioned semiconductor LEDs, organic (OLED) and polymer (PLED) being the other two methods. Currently, most commercial LEDs use inorganic semiconductors as their sources for illumination. The seminal advances in the field of semiconductor electroluminescence were:

1. Demonstration of red LED emission by N. Holonyak in 1962

2. Demonstration of blue LED by S. Nakamura in 1993 along with I. Akasaki and H. Amano

Initial commercial introduction of LED lamps took place in 1968: indicator lamps by Monsanto and electronic displays by Hewlett-Packard. Due to the availability of only red LEDs, the initial performance of these products was quite poor at just 1 millilumen (mlm) at 20 mA since the human eye is relatively insensitive in the red region.
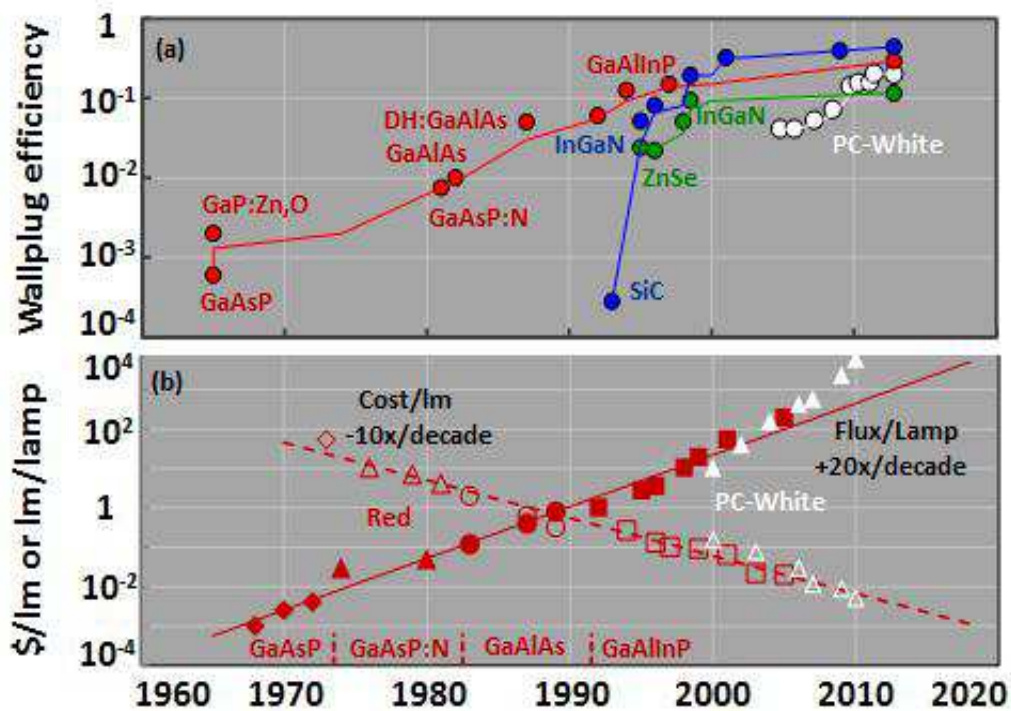
Figure 1.1: Progress in luminescence efficiency over the years in red LEDs with blue LEDs joining post 1993

The top panel infographic in Figure 1.1 shows a steady and encouraging performance improvement of red LEDs in terms of luminescence efficiency and cost per lumen. The wall plug efficiency, also known as radiant efficiency is defined as the energy conversion

efficiency with which the system converts electrical power into optical power. It is measured as the ratio between the radiant flux (total output power) and the input electrical power. The efficiency improved as a result of development of newer materials such as GaP and GaAsP, followed by AlGaAs leading to AlInGaP. This improved the efficiencies by more than two orders of magnitude, jumping from about 1/50 lm/W in the 1970s in GaP and GaAsP based LEDs to 10 lm/W in 1990 from AlGaAs based LEDs, when it started replacing the red-filtered incandescent bulbs in terms of luminescence. The current state-of-the-art LEDs employ AlGaInP emitting at more than 150 lm/W. By 1985, they were viewable in ambient light, but were still limited to small indicator and display applications which required nor more than 100 mlm per indicator function or display pixel. It was around this time that red LEDs finally ventured beyond the small signal applications and found a place initially in the centre high mount stop light (CHML) in automobiles which was the medium flux power signaling market with flux requirements between 1-100 lm. The material properties overtook the applications soon and red LEDs were regularly fabricated with flux of > 100 lm. Evolution of technology drove the quest for researching higher efficiency devices and attainment of higher efficiencies further propelled the market. Large number of small signal LEDs became too expensive and the demand for high-emission, high-power LEDs rose as a result. The bottom panel of Figure 1.1shows a Haitz's law graph which indicates that the progress in efficiency had a tremendous impact on the cost per package and cost per lumen. Flux per lamp has increased 30 times every decade, and the cost per lumen (price charged by LED suppliers to original equipment manufacturers or OEMs) has been decreasing 10 times per decade.

The breakthrough in blue LEDs was initialized in 1969 with the first hydride vapor phase epitaxy (HVPE) growth of GaN by Maruska and Tietjen[1]. Early 1970s saw a lot of undoped, Mg- and other impurity doped GaN films being grown[2–6]. The first electroluminescence from GaN was demonstrated by Pankove *et al.* in 1971[2], and although the structure was a metal-insulator-semiconductor (MIS) diode and not a conventional p-n junction it was still commercialized by Toyoda Gosei Co. Ltd. in Japan in 1993 where the output power was of the order of 1-5 μW. However, poor crystal quality led to the residual carrier concentration being at 10^{19} cm^{-2} which resulted in devices with low outputs. It was Yoshida *et al.*[7] who used molecular beam epitaxy in 1983 to employ

an AlN buffer layer to improve film quality; a concept later used by Amano *et al.*[8] to achieve an electron concentration of 10^{17} cm^{-2} using a metal organic chemical vapour deposition (MOCVD) system in 1986. Amano *et al.* were also the first group to employ a low energy electron beam irradiation (LEEBI) technique to achieve the first p-type Mg-doped GaN in 1989[9] with a hole concentration of 10^{16} cm^{-2} and mobility of 8 cm^2/V.s at room temperature using a low temperature GaN buffer layer. This was also the first instance of a p-n junction LED being fabricated using GaN where they demonstrated the I-V curve and the electroluminescence but did not record the output power or the efficiency of the LEDs. In 1991, Nakamura *et al.* used the LEEBI treatment to achieve p-n junction GaN LED employing a low temperature GaN buffer layer[10] though it was not commercialized. The next section discusses the advent of III-nitrides in the field of LEDs up till now.

1.2 III-nitrides

After the discovery of GaN, it was straightforward thereon to alloy it with In and Al to obtain varying band gaps to span the whole solar spectrum. A schematic is shown in Figure 1.2 describing the band gaps of III-V materials and some other semiconductor materials in use today such as Si and Ge. It is apparent that in order to span the maximum range of energies, alloying within III-N materials is the only option. Other semiconducting materials such as GaAs and CdTe have very low band gaps and even after alloying it is not possible to span much more than the solar spectrum. More importantly, since green, blue and ultraviolet photons represent frequencies in visible and beyond the visible spectrum, they can only be produced using materials with a band gap of at least 2.2 eV. The available materials in this range include diamond (5.47 eV), silicon carbide (2.99 eV) and the group III nitrides such as GaN (3.4 eV). The achievement of blue LED by incorporation of indium[11] opened the door for white light emission and various other applications such as cell phones, computers, TVs etc. However, since these LEDs have a structure that requires the deposition of InGaN layers over a GaN layer, there is a deterioration in quality for higher In compositions because of lattice mismatch between InGaN and GaN. Further, because of the efficiency drop, obtaining emission in green wavelength range is difficult for commercial applications, an issue which is popular by

the name of "*green gap*". Although this problem is currently overcome by coating a high efficiency blue LED with phosphor to obtain green emission, further research is underway to obtain high brightness green LEDs. As of 2013, Osram has managed to obtain an intensity of 108 lm/W which can be raised to 135 lm/W for a larger chip with a lower power density. Other companies are trying their own methods to overcome this issue which is a major roadblock for obtaining high intensity green LEDs and consequently white light.
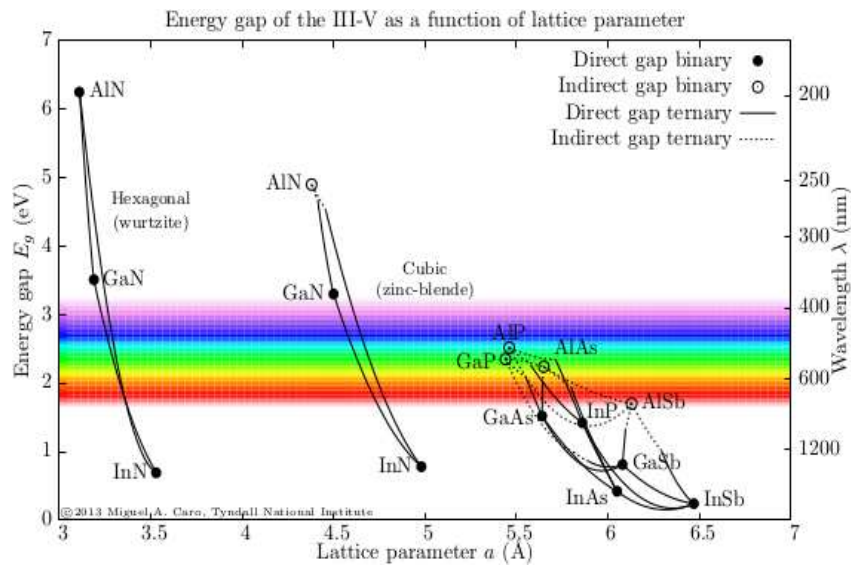
Figure 1.2: Schematic showing the III-nitride materials in terms of band gap compared to other semiconductors*

Since the III-nitride materials can be tuned to obtain devices operating in ultraviolet region also, it is possible to obtain high efficiency devices using these compounds. However, as explained in the next section, the growth of high quality GaN films is challenging and involves several issues which have prevented the incorporation of GaN-based materials in the various applications wherein they are expected to excel.

†

1.3   GaN: material properties

GaN is a wide, direct band gap semiconductor with a band gap of 3.4 eV[12] which can help devices operate in the ultraviolet region of the spectrum. It can be alloyed

---

†*image from mcaroba.dyndns.org, thesis of Miguel Caro, University College Cork

with In and Al to obtain band gaps that span the whole solar spectrum, and enable applications such as LEDs and solar cells. Further, it is chemically stable even at elevated temperatures (up to about 1173 K) which makes it suitable for caustic environments albeit offering technological challenges in device fabrication. It has three allotropes: wurtzite, zinc blende and rock salt. Nitrides are usually observed as having wurtzite structure, but they can also crystallize in the zinc blende polytype which is a metastable state primarily achieved with non equilibrium growth conditions. Figure 1.3 shows the arrangement of atoms in the wurtzite structure of GaN which comprises of two interpenetrating hexagonal close packed (HCP) sub-lattices of Ga and N with an offset of $\frac{5}{8}$ along the vertical direction of the unit cell. A single unit cell is shown in Figure 1.4 which contains 4 atoms (space group P6$_3$mc) and has a shape of vertically oriented prism. The base is defined by the primitive lattice vectors, $\overrightarrow{a}$ and $\overrightarrow{b}$, which have equal lengths and are separated by an angle of 60°. Both $\overrightarrow{a}$ and $\overrightarrow{b}$ lie in the xy plane and the height of the cell is defined by the vector $\overrightarrow{c}$ which is at an angle of 90° to both $\overrightarrow{a}$ and $\overrightarrow{b}$. In the ideal wurtzite structure, the lengths of the vector $\overrightarrow{c}$ is related to $\overrightarrow{a}$ or $\overrightarrow{b}$ by the relation $\overrightarrow{c} = 2\sqrt{\frac{2}{3}}a$. Since this structure lacks an inversion point, group III nitrides which crystallize in wurtzite exhibit effects like piezoelectricity and pyroelectricity among other properties, such as band folding which are interesting. The typically performed epitaxial growth is in the (0001) direction which leads to the piezoelectric polarization field along the growth direction. In the strained material, it influences carrier concentrations, electric fields etc. which have significant effects on the resulting electronic and optical properties of the overgrown film. Therefore, due to the wurtzite structure induced polarization and the polar nature of the substrate, the resultant carrier concentration is enormous when both the factors are combined. In the bulk material usually it is assumed that rearrangement of surface charges would nullify spatially uniform the electric fields, but it is not the case in heterostructures where the quantum confined Stark effect (QCSE) is known to reduce the internal quantum efficiencies of LEDs fabricated on such surfaces. Hence, although the piezoelectricity is detrimental for LED fabrication, it is still being studied for its other uses, one such being surface acoustic wave (SAW) filters.
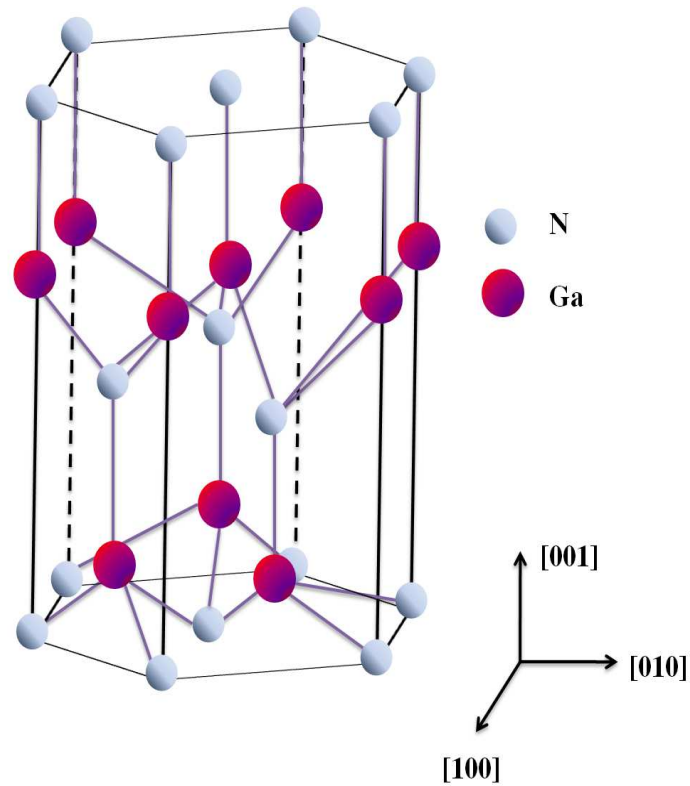
Figure 1.3: Wurtzite structure showing arrangement of atoms

1.4   Substrates

One of the most basic issues with growing gallium nitride is the unavailability of
a suitable substrate upon which a defect free film can be grown. Since nitrogen is
insoluble in gallium at equilibrium, it is very difficult and expensive to obtain crystals of
GaN that can be employed as substrates for homoepitaxial growth. Efforts were made
between 1930-1960 to obtain single crystals of GaN but success was obtained only with
the experiments of Zetterstrom[13] and Karpinski[14] who showed that a nitrogen pressure
of 16 kbar at 1773 K was the best condition for obtaining relatively large size crystals
of GaN. Although later experiments by Porowski[15] resulted in growing GaN below its
melting point, most groups pursued the heteroepitaxial thin film approach. However, for
heteroepitaxial growth, the most popular choice of substrate is sapphire, which also has
a wurtzite structure, is transparent, stable at room temperature and has good optical
quality. However, sapphire has a 16 % lattice mismatch with GaN which introduces
defects such as threading dislocations in the overgrown film. This reduces device quality
by forming scattering centers that decrease the mobility of electrons. Other options that
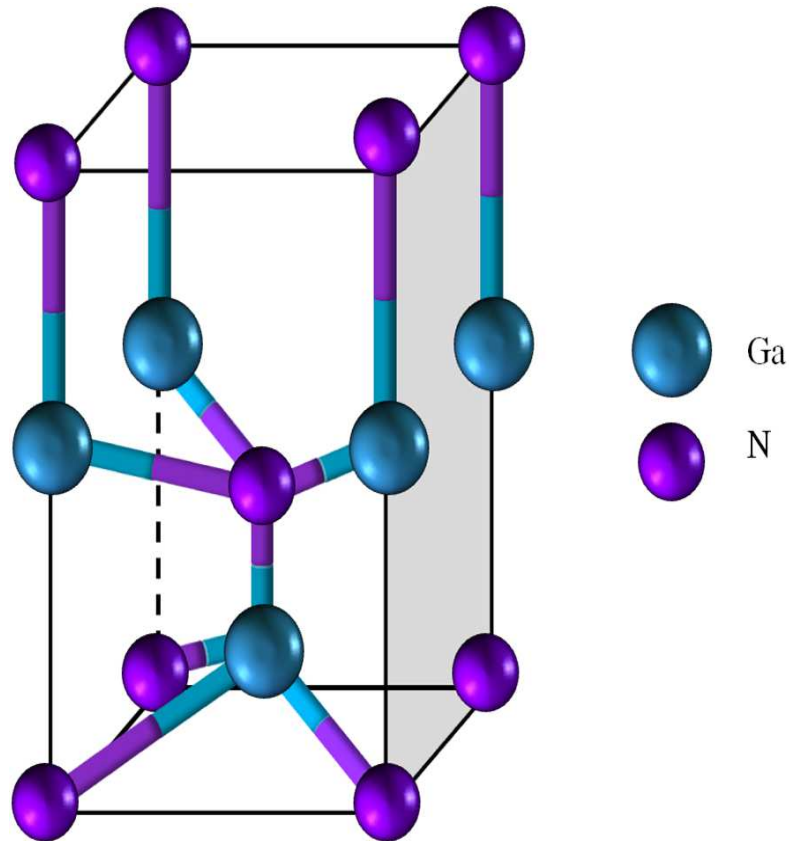
Figure 1.4: Unit cell of a wurtzite structure

have been tried include 6H-SiC, which despite having only a 3% lattice mismatch and a higher thermal and electrical conductivity than sapphire is substantially more expensive confining its use for research purposes only. ZnO has a wurtzite structure with ≈ 2.2 % lattice mismatch and offers an alternate substrate for growing equilibrium wurtzite GaN. 3C-SiC and MgO are both cubic zinc-blende structures which have a better structural and thermal match with nitrides compared to sapphire. Hence, they are the most popular choice for growth of cubic phase of GaN which is also being explored for its potential applications apart from the wurtzite phase.

Material	Epitaxial relationship	Lattice parameter (Å, 300K)	Lattice mismatch (%)
GaN (wurtzite)	-	a = 3.189 c = 5.178	-
AlN (wurtzite)	$(0001)\parallel(0001)$ $(11\bar{2}0)\parallel(0001)(11\bar{2}0)$	a = 3.111 c = 4.979	2.4 4.1
α-sapphire(wurtzite)	(0001)——(0001) (c-sapphire)	a = 4.759 c = 12.991	13.8 13.8
	$(1\bar{1}30)\parallel(0001)(1\bar{1}30)$(m-sapphire)		0.4 -1.9
	$(0001)\parallel(0001)(2\bar{1}\bar{1}0)$(a-sapphire)		2.6 -1.9
	$(2\bar{1}\bar{1}0)\parallel(0001)(01\bar{1}2)$(r-sapphire)		13.8 1.1
6H-SiC	$(0001)\parallel(0001)(0001)$	a = 3.086 c = 15.117	3.5 3.5
Si (diamond)	$(0001)\parallel(0001)(0001)$	5.431	17
ZnO (rock salt)	$(0001)\parallel(0001)(111)$	4.580	-1.9

Table 1.1: Comparison of different substrates for GaN heteroepitaxy

1.5   Dislocations

The most important issue with heteroepitaxial growth is the incorporation of dislocations in the overgrown film due to lattice mismatch with the non-native substrate. The movement of atoms of the overgrown film to attain their lattice parameter results in imperfection in the crystal lattice. There are mainly two types of dislocations, edge and screw. Edge dislocations are formed when an extra half-plane of atoms is present in the lattice which distorts the nearby planes due to disproportionate forces acting upon them.

As shown in Figure 1.5 above, the Burgers vector (denoted as $\vec{b}$) describes the magnitude and the direction of propagation of the lattice distortion. For an edge dislocation it is simpler to visualize the dislocation as just missing of a few atoms which runs all along the lattice, but for a screw dislocation the picture is slightly more complex. Consider there being a slip plane in the crystal; for a screw dislocation, a shear stress on this plane would cause atomic planes above to slightly shift towards one side and the planes below to shift the same amount towards the opposite side, like a ripple. As the screw dislocation propagates, the atomic planes contort and resemble a screw with their displaced positions.
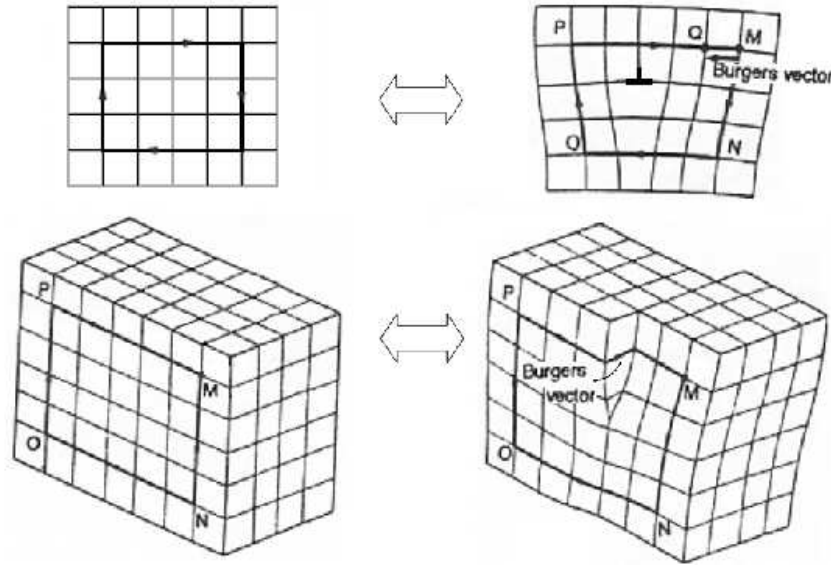
Figure 1.5: Schematic showing edge and screw dislocations as visualized in a lattice

Growing wurtzite GaN on (0001) surfaces can lead to defects propagating in the $< 0001 >$ direction which are termed as "*threadingdislocations*" or along the (0001) direction which are the "*basaldislocations*". The threading dislocations can be of screw, edge or mixed types. The directions and magnitudes of the Burgers vectors related to the three types are listed in the table below:

Type	Burgers vector	Magnitude	Energy
Edge	$\frac{1}{3} < 11\overline{2}0 >$	0.319 nm	a^2
Screw	$< 0001 >$	0.518 nm	c^2
Mixed	$\frac{1}{3} < 11\overline{2}3 >$	0.608 nm	$a^2 + c^2$

Table 1.2: Types of dislocations found in the w-GaN crystal. The Burgers vector and its magnitude are also mentioned along with individual energies

The screw and edge type dislocations are interchangeable under the application of stress. On a typical GaN on c-sapphire growth, the average threading dislocation density (TDD) is quite high ($\sim 10^{12}$cm^{-2}), with edge being the dominant type. The TDD drops rapidly with thickness of the film through mutual recombination which can be seen in HVPE grown films. The nomenclature of dislocations in GaN is defined on the direction of propagation; the threading screw dislocations along $< 0001 >$ direction are called c-type dislocations while the threading edge dislocations along $\frac{1}{3} < 11\overline{2}0 >$ are called a-type dislocations. The one with burgers vector b $= \frac{1}{3} < 11\overline{2}3 >$ that are either in the prismatic (any plane parallel to c-plane) or glide plane are called mixed or (a+c) type dislocations. Typical burgers vector with their representative glide planes are shown in

Figure 1.6; each one refers to a specific kind of dislocation.
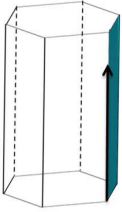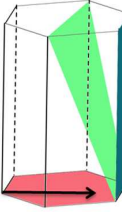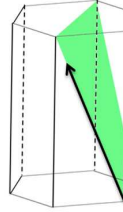
Burgers vector	b = <0001> (c-direction)	b = 1/3<11$\bar{2}$0> (a-direction)	b = 1/3<11$\bar{2}$3> (r-direction)
Visualization			
Glide plane	{1$\bar{1}$00}	{0001}, {1$\bar{1}$00}, {1$\bar{1}$0n}	{1$\bar{1}$00}, {1$\bar{1}$0n}
Nomenclature	c-type dislocations	a-type dislocations	a+c type dislocations

Figure 1.6: Schematic showing various glide planes of GaN on which dislocations are present for growth along (0001) direction

1.6 Thin film growth methods

There are many methods which have been employed to perform thin-film growth, with each technique having its own advantages and disadvantages. A few of the techniques have been summarized below:

1.6.1 Molecular Beam Epitaxy (MBE)

One of the most popular methods to produce single crystals, MBE was invented in late 1960s in Bell laboratories. The term MBE itself is used to infer to the process of epitaxial growth of compound semiconductor films using the reaction between one or more thermal molecular beams on a crystalline surface under ultra high vacuum (UHV) conditions ($< 10^{-10}$ Torr). Due to UHV conditions, the procedure offers excellent control on the growth of the films at an atomic level such that difference between sticking coefficients of different elements may be taken into account. Further, the technique provides a slow growth rate ($\approx 3~\mu$m/h) which lets the films grow epitaxially and allows extremely acute control over the thickness of the films down to a single atomic layer. For improved layer uniformity, the sample holder is designed for continual azimuthal rotation of the sample, commonly known as the CAR assembly. Due to the high vacuum levels in the chamber, the contamination is reduced and to date the highest purity in films is achieved using MBE. The MBE growth process cannot be described by a thermodynamic representation, as the different parts involved in the process, such as sources, substrate and walls are at different temperatures. Therefore, in a nonequilibrium growth environment, a kinetic model best describes MBE growth. Compared to other methods which utilize chemical reactions such as MOCVD, MBE growth of GaN takes place at temperatures in the range of 500-800 °C. Although the Ga-N bond strength is strong and is estimated as being around 4.2 eV, GaN decomposes above 800 °C in atmospheric pressure and at lower temperatures in vacuum. At high temperatures the decomposition rate surpasses the deposition rate, which limits the growth temperatures which can be employed for film formation. Low temperatures reduce surface adatom mobility which leads to defects in the film, which is usually avoided by introducing a surfactant impurity which increases mobility of surface atoms. However, it is still the best technique for maintaining precise

control of interface and thickness of layers; although due to its expensive cost and maintenance it is primarily used for optimizing of structures. Currently, MBE is used to grow complex structures which are processed to produce a wide range of electronic and optoelectronic devices such as high electron mobility transistors (HEMTs), high efficiency solar cells and solid state lasers.

1.6.2   Metal Organic Chemical Vapour Deposition (MOCVD)

In MOCVD, the deposition takes place using chemical sources in contrast to physical sources used in MBE. The MOCVD reactor is maintained at pressures of 10-760 Torr and ultrapure gases are introduced into the chamber which are then pyrolized at high temperatures onto a substrate providing a control of a few nm thickness of the layers. Though the control is lesser than MBE, the high throughput and cheaper cost makes MOCVD a popular choice to manufacture devices on a larger scale. As the process involves heated gas flow and chemical reactions occurring on the surface, the typical substrate temperature is in the 500-1500 °C range. To ensure uniformity the sample can be rotated at speeds of 1500 rpm. The major disadvantage of MOCVD has been the usage of large quantities of toxic gases such as AsH_3 and PH_3, though recent development of less hazardous precursors has overcome this issue. Also, parasitic reactions such as the solid adduct formation between TMAl and NH_3 in case of AlN growth reduces growth rate, but still the growth rates are high ($\approx$ few μm/h) and can be used. A limitation in MOCVD growth is the lack of *in-situ* monitoring during growth, which is possible in MBE due to the large source-to-sample distance and high vacuum. However, the MOCVD growth is thermodynamically favorable in contrast to MBE growth which is kinetically controlled. MOCVD yields multi-wafer films that are used to form structures that display effects such as the two-dimensional electron gas (2DEG). two-dimensional hole gas (2DHG), various transport properties and quantum size effects (QSE) in heterostructures and multilayers.

1.6.3   Hydride Vapor Phase Epitaxy (HVPE)

HVPE is a low cost method used to grow thick films at rates in excess of 100 μm/h. It lacks the control and heterojunction layer growth required to obtain device quality structure and is mainly used to obtain large crystals of GaN. It is one of the earliest

methods used to obtain GaN crystals and dates back to 1960's. Pure metal is heated to obtain metal atoms which are then reacted with HCl at 800-900 °C forming a volatile gaseous metal chloride which then reacts with NH_3 to give GaN crystals. In this method, HCl and H_2 are present in the reactor which can etch the GaN film resulting in a rough surface morphology of the film. The purity of materials used in HVPE growth is higher than MOCVD, which makes it a good choice to produce thicker and free-standing layers. In terms of fabricating ternary alloys, HVPE is not a suitable technique since high growth rates do not allow for rapid compositional changes required during growth. Also, since the flow of HCl cannot be abruptly terminated, forming sharp interfaces is not as simple as the other techniques discussed earlier. The presence of HCl also puts a constraint on the substrates used for film growth. Silicon is readily attacked by HCl forming silicon chloride which may get incorporated in the film. The other by-products are liquid gallium from the reaction of silicon with GaCl which disrupts the crystallinity of the epitaxial growth. Hence, films grown on silicon tend to be heavily doped with silicon and have poor morphology. Passivation of the surface with a low temperature AlN or GaN film grown by CVD techniques are used to overcome this problem but silicon carbide and sapphire are better substrate candidates due to their inertness towards HVPE reactor environment. The most important advantage of HVPE is that crack free, low dislocation density ($\approx 10^7$ cm^{-2}) thick films ($\approx 10~\mu$m) can be produced in relatively quick time which are useful for optoelectronic and RF electronic devices. The "$carbon - free$" environment also ensures lower contamination levels than MOCVD and the presence of HCl provides an impurity "$self - cleaning$" effect improving the doping levels of the epitaxial films.

1.7 Efforts to improve film quality

The most significant progress to achieve better quality films in the past decades has been the application of low temperature nucleation layers. Since the best bet remains to get defect free GaN in order to perform homoepitaxy, research has moved on to produce bulk crystals; although thick and free standing GaN and AlN films are still desirable for III-nitride based epitaxial growth. For c-sapphire, deposition of AlN or GaN layers at low temperatures of 500-750 °C showed a remarkable improvement in

	MBE	MOCVD	Plasma-assisted MOCVD	HVPE
Source	Metal, gas	MO, NH$_3$, carrier gases	N$_2$, MO	Metal, NH$_3$
Source safety	Safe	Higher risk	Safer than MOCVD	Safe
Deposition temperature (GaN)	≈ 600-900°C	≈ 950-1200°C	<700°C	<1150°C
Pressure	UHV: < 10^{-11} Torr	15-750 Torr	NA	760 Torr
Speed	≈ 1 µm/h	1-10 µm/h	<0.5 µm/h	50-200 µm/h
Interface control	Very good: atomic layers	Good: difficult to get layers thinner than 3-4 nm	Poor	Poor
Parasitic Reactions	None	High	High	High
Uptime (cleaning)	6-12 months	6-10 days	NA	Heavy maintenance

Figure 1.7: Comparison between most popular growth techniques highlighting advantages (green), disadvantages (red) and comparable properties (orange)

quality for films grown above 1000 °C[16]. However, since the theoretically predicted dislocation density (also called as threading dislocation density or TDD) of 10^7 cm^{-2} was not achieved, filtering dislocations in GaN films has remained a research topic. Further approaches in this area include pre-nitridation[17–19] of substrate, epitaxial layer overgrowth (ELOG)[20–22] and *pendeo*-epitaxy[23]. These approaches have now enabled reduction of the dislocation densities to 10^7 cm^{-2}, but the demand of producing more sophisticated devices operating at extreme conditions of temperature, voltages and current densities have pushed towards the search of better substrates. Recent efforts have moved towards producing nanostructures which are known to be dislocation free[24–26] and the possibility of using them as substrates to perform homoepitaxy. In this regard, the most obvious choice of researchers was to produce nanowires[27–30] which have proven to be extremely advantageous and brought about applications ranging from field emission transistors[31–33] and lasers[34–37]to solar cells[38,39]. The TDD in nanowires is virtually negligible since their footprint on the substrate is extremely small and they also have high surface area on the sidewalls, which leads the dislocations to terminate on the wall in order to reduce their line energy. Apart from nanowires, another interesting

nanostructure which has been previously studied in systems such as carbon[40–42] and ZnO[43–45]is the nanowall. There have been attempts to obtain porous structures of GaN by etching epilayers in order to alleviate strain[46,47] but the advent of nanowalls has opened up a separate field in itself. Owing to its large surface area, it has prospective applications in solar cells[48] and sensors[49]. Further, since it is also known to eliminate threading dislocations by the same mechanism as nanowires, it is interesting to probe whether it can be used as a prospective substrate for homoepitaxial growth of GaN. In this regard, this thesis presents a comprehensive understanding of GaN nanowalls fabricated using plasma-assisted molecular beam epitaxy on c-sapphire substrate and its properties. The work explores ways of tuning the structure by controlling the growth parameters and the effect of different nanowall dimensions on their properties. Optical and transport properties have been studied in detail and an attempt has been made to correlate the separate nanowall morphologies with the results obtained.

Chapter 2

Literature Overview of the growth of GaN and its nanostructures

2.1 Introduction:

The research topic explored in this thesis is the formation of a novel nanostructure of GaN; termed as a nanowall network, its properties and potential uses in various applications. Currently, a wide variety of work is being persued, which involves the growth of GaN using MBE, formation of several nanostructures and their applications in a plethora of fields including light emission. It is pertinent to gather as much information about this background in order to understand the scope of this thesis and to make an informed judgment about this work. As mentioned in the introduction chapter, from its brief history to the evolution of GaN based technology, a lot of effort has already been made to make GaN in different forms including alloying, nanostructuring and making heterostructures to get high performance devices. For structural and light emission properties, the most commonly used experimental probes are SEM, TEM, XPS, Raman spectroscopy, XRD and PL with many other variations employed by different groups.

Since this thesis attempts to explore the applicability of a novel nanostructure of GaN and its prospective applications as a light enhancer and biosensor, this chapter intends to review relevant literature that explains the status of the field which helps us understand and define the nature of the experiments to be performed and their interpretation.

2.1.1   Growth of GaN to improve light emission

By 1993, working LEDs based on GaN were demonstrated but were not commercialized due to their limited luminescence capabilities. This section aims to summarize the improvements made over the years to increase light emission from GaN-based devices using various techniques. Since the devices are majorly fabricated using thin film deposition, it is pertinent to obtain a suitable substrate upon which the growth can take place. In case of GaN, substrates sharing the same lattice parameter, such as GaN itself, are not only very expensive to use, but large sized crystals are yet to be grown. Therefore, majority of the research takes place using substrates which have different lattice parameters. Performing heteroepitaxial growth on lattice mismatched substrates leads to inherent stresses at the interface, which are relieved via the formation of dislocations. These dislocations are detrimental to device performances since they introduce scattering centers in the film which act as non-radiative defects and inhibit electron transport. A lot of effort has been made with regard to circumventing this problem so as to improve device quality. One of the earliest methods already mentioned before is the application of low temperature buffer layers of either AlN or GaN itself. It was assumed that lowering threading dislocation density (TDD) is required to improve light emission from GaN layers, since it was proved that a low TDD is required to improve electronic properties. However, it was noted to much surprise by researchers that GaN based LEDs were able to provide sufficient brightness even with dislocation densities to the tune of 10^{10} cm^{-2}[50]. Other III-V material systems would not show any emission under such large defect densities. A hypothesis by Chichibu *et al.*[51] suggested that minority carriers injected into InGaN layer are trapped in the localized states caused by fluctuations in In compositions before being dissipated by the nonradiative recombination centers. However, a theoretical study carried out by Karpov *et al.* pointed out that a dislocation density of at most 10^7 cm^{-2} is needed to achieve an internal quantum efficiency of unity[52]. This led researchers to explore a wide array of growth methods including epitaxial lateral overgrowth (ELOG)[20,53], *pendeo*-epitaxy[23,54] and nanostructuring[55,56]. Among these, nanostructuring showed a lot of promise since nanowires show termination of threading dislocation because of the presence of sidewalls and a large surface area[26] and therefore are potentially dislocation-free. Further, since their footprint on the substrate

is small the lattice mismatch based defects are minimal. With so many advantages, the research community was drawn into the exploration of nanostructure-based devices which has seen a lot of progress over the years. Using MOCVD, GaN nanowires have been grown and fabricated into devices which have shown superior optical quality[57]. Another major issue is to improve the light extraction efficiency from the surface since without it, only a small fraction of light ($\frac{1}{4n^2}$ per surface) is emitted due to total internal reflection, where n is the refractive index of the material. Different methods such as surface roughening[58,59] and geometrical modification[60,61] have been employed previously, but they depend on random light redirection. Photonic crystals (PhCs) were then employed[62–64] which were able to controllably extract light and reduce lossy reflections. Currently, PhC GaN LEDs give a light extraction ability of an average of 3.5 times[62] which has reasonable agreement with theoretical predictions[65].

2.1.2 Experimental techniques used to grow GaN nanowires

Since GaN nanowires were the most popular choice of nanostructures to improve LED efficiency, it is pertinent to follow the progress of the nanowire growth and application research over the past decade or so. This section discusses the various growth techniques and their properties used to grow GaN nanowires.

Chemical Vapour Deposition

Chemical vapor deposition (CVD) is a process in which a solid material is deposited from a vapor by a chemical reaction occurring on or in the vicinity of a heated substrate. The solid material can be in the form of a layer, powder, or single crystal. Upon changing the experimental parameters such as substrate material or temperature, composition of the reaction gas mixture, total pressure of the gas being flowed, etc., materials with different properties can be grown. A characteristic feature of the CVD technique is its excellent "*throwing power*" which enables the production of coatings possessing uniform thickness and properties with low porosity even on substrates of irregular shapes. Another characteristic feature is localized, or selective deposition, on patterned substrates. CVD is employed in many thin film applications, for instance, in the microelectronics industry to make films of dielectrics, conductors, passivation layers, oxidation barriers, and epitaxial

layers. Optical fibers, as well as wear-, corrosion-, and heat-resistant coatings are commonly made with this technique. Other applications are in the preparation of high temperature materials (tungsten, ceramics, etc.) and the production of solar cells, high temperature fiber composites, and size-specific particles. Even high-T_c superconductors have been recently fabricated by this technique. The first GaN nanowire growth using CVD was reported by Han *et al.*[66] which was also the first report of producing GaN nanowires. Carbon nanotubes (CNTs) were used in their method to confine the reaction within the tubes leading to a nanowire morphology. The reaction in the GaN nanowire growth process was carried out at high temperature in a conventional furnace with a horizontal tube:

$$2Ga_2O_{(g)} + C(NTs) + 4NH_3 \rightarrow 4GaN(NWs) + H_2O + CO + 5H_2 \qquad (2.1)$$
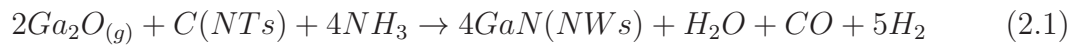
The precursor for Ga_2O_3 used in the reaction consisted of a 4:1 molar mixture of Ga-Ga_2O_3 powders. From HREM images it was confirmed that the GaN nanowire so produced had a diameter similar to the carbon nanotubes.

Following this, more attempts were made using CVD to improve the quality of GaN nanowires, including those by Chen *et al.* who used a NiO catalyzed technique[67] to obtain smooth and straight GaN nanowires deposited on LaAlO$_3$ substrates at 920-940 °C in a flow of NH$_3$. Prior to the deposition, the substrates were dipped into a $Ni(NO_3)_2$ ethanol solution and then heated at 900 °C in a long quartz tube with a continuous flow of Ar for 2 hours in order to decompose $Ni(NO_3)_2$ into NiO nanoparticles. These nanowires were 10-40 nm in diameter and grew to a maximum length of 500 μm. Johnson and coworkers[34] then used sapphire as a substrate to deposit GaN nanowires using a Ni catalyst in a CVD system using metallic gallium and ammonia as sources of Ga and N respectively. The deposition was carried out at 900 °C which formed nanowires with lengths extending to several hundreds of microns and diameters between 30 and 150 nm. The mechanism underlying this method is called the vapour-liquid-solid (VLS) mechanism, which is currently the most widely used due to its simplicity and versatility with respect to application in semiconductor systems. It is a 1D crystal growth mechanism which is assisted by a metal catalyst and results in the creation of

rods, wires, whiskers etc. Growth of 1D growth was introduced in the Si industry 50 years ago and its mechanism was suggested for wider use by Wagner in 1964[68]. The mechanism starts with the metal catalyst forming liquid alloy droplets at elevated temperatures upon absorption of vapour components. The alloy then gets supersaturated with temperature or pressure fluctuations, leading to concentrations of components within the alloy being higher than the equilibrium concentration. This situation drives the precipitation of the component at the liquid-solid interface to achieve minimum free energy of the alloy system. Consequently, 1D crystal growth commences and proceeds as long as vapour components are provided. The VLS term itself is coined since the system involves vapour (carrying solid components), liquid (metal catalyst alloyed) and solid (1D crystals precipitated) phases in the mechanism.

The methods described above to obtain GaN nanowires using template based CVD or depositing on expensive single crystal substrates gave very low yields. Chen and Yeh[69] demonstrated a method for large scale production of GaN nanowires on silicon wafers by reacting gallium and ammonia using polycrystalline indium as a catalyst. Molten gallium and powdered indium in toluene were placed on the substrates initially, followed by the evaporation of toluene. The substrate was then transferred onto a quartz tube and kept in a furnace with the temperature set at 910 °C for 12h under a constant flow of ammonia. This reaction resulted in large quantities of GaN nanowires being formed with diameters ranging from 20 to 50 nm and lengths extending upto several microns.

To fabricate devices based on nanowires, it is important to obtain low defect density and long nanowires. Although the nanowires may be produced ideally; the processing, dispersion and patterning techniques such as ultrasonication and lithography can introduce unwanted defects. To alleviate this issue, Li and coworkers demonstrated a method of nanowire growth which was suitable for *in-situ* fabrication of nanoelectronic devices[70]. Using a "dip-pen" nanolithographic (DPN) technique, a contact-mode AFM tip was dip-coated with $Ni(NO_3)_2$ solution and was used to coat a very small amount of it onto a substrate. The position of the catalyst was controlled using a piezoelectric scanner and the GaN nanowires were synthesized in a horizontal tube using elemental gallium and ammonia precursors.

Metal Organic Chemical Vapour Deposition

Metal Organic Chemical Vapour Deposition (MOCVD) is a chemical deposition method of epitaxial growth of films from surface reaction of organic compounds or metal organics and hydrides containing the desired elements. More specifically, vapours of metalorganic compounds are transported in a carrier gas and are decomposed at or near a substrate which is maintained at high temperatures. MOCVD is also known by alternate names such as metal organic vapour phase epitaxy (MOVPE), organometallic vapour phase epitaxy (OMVPE), and organometallic chemical vapour deposition (OMCVD). Currently, MOCVD is the most successful and widely used method to grow nitride films, since it is scalable to produce high volumes of excellent quality multilayer heterostructures with high growth rates. There still remain a lot of issues with the technique since the high temperatures required for efficient decomposition of the precursors influence the quality of the grown films since differences in thermal diffusion induces additional dislocations.

The MOCVD technique was used to grow GaN nanowires for the first time at the University of California, Berkeley by the Yang group in 2003[57], using Trimethylgallium (TMG) and Ammonia as sources of Ga and N, respectively. The substrates used by them were Si, a-sapphire and c-sapphire on which thin films of Ni, Fe or Au were pre-deposited using thermal evaporation. At a substrate temperature of 800-1100 °C, the nanowire growth commenced via the VLS mechanism. In an oxygen-free environment, nitrogen was flown as a carrier gas at atmospheric pressure which percolated with the TMG precursor and joined a second nitrogen line. The resulting nanowire dimensions on a Au-coated c-sapphire substrate were 15-100 nm diameter and 1-5 μm length. It was also observed that the growth was epitaxial in nature since there were preferred orientations of the nanowires on the sapphire substrate.

This report was followed by Su *et al.* who also used a catalyst-assisted VLS mechanism growth in an MOCVD reactor[71]. Sapphire, alumina and SiO_2 were the substrates of choice which were dipped in a 0.01 M $Ni(NO_3)_2$ aqueous solution and dried on filter paper before loading in the MOCVD chamber. The GaN nanowires obtained at an intermediate ammonia flow had diameters of 100 nm and lengths upto 5 μm. They also observed that the liquid mediated, anisotropic 1D growth depends sensitively on

the growth stoichiometry or the V/III ratio. The nanowire growth was made scalable with the efforts of Stephen M. Hersee *et al.*[28] who were able to demonstrate growth of precisely controlled nanowire positions and dimensions which were grown in an MOCVD reactor without the presence of any external metal catalyst. They deposited a 30 nm silicon nitride growth mask layer by low pressure chemical vapour deposition onto 600 nm thick GaN films previously grown using MOCVD on silicon carbide, sapphire and Si (111) substrates. The growth was carried out at 1050 °C at a pressure of 100 Torr with a mixture of hydrogen and nitrogen gases used as a carrier in a MOCVD reactor. GaN nanowires were obtained in arrays from the growth mask and the diameter of each nanowire remained constant during the growth process.

Laser Ablation

Another technique used to obtain GaN nanowires is laser ablation, where pulsed laser is used to vaporize a solid target and a catalyst at high temperature. The key feature of this method is that the catalyst used to define the nanowire growth can be selected from a phase diagram or through a knowledge of chemical reactivity[27]. After the vaporization of the target, the resulting liquid nanoclusters define the properties of the nanowires via a vapour-liquid-solid (VLS) growth mechanism[27,72–74]. The Lieber group at Harvard is attributed to making important contributions to the development of the laser ablation method to synthesize single-crystalline compound semiconductors[27,72,73]. The laser ablation process described by Duan and Lieber[27] to obtain single crystalline GaN nanowires consists of a GaN/Fe (GaN:Fe = 0.95:0.05) composite target placed along with a quartz tube at the center of a furnace. A pulsed Nd:YAG laser (1064 nm, 8 ns pulse width, 10 Hz repetition, 2.5 W average power) was used to ablate the composite and the Fe clusters direct the growth as well as define the diameter of GaN nanowires which get deposited on the inner wall of the quartz tube. The dimensions of the nanowires obtained in this experiment were about 10 nm diameter and length exceeding 10 μm. Ng *et al.* used laser ablation to obtain nanowires of lengths of 300-500 nm and diameters of 50 nm[75]. They ablated a GaN target using a KrF excimer laser (248 nm, 23 ns) operating at a fluency of 2.2 J/cm² and the plasma plume was directly deposited onto a sapphire substrate coated with 10 nm of Au. The as-grown nanowires had a eutectic Au-GaN tip

demonstrating the VLS mechanism of growth.

Molecular Beam Epitaxy

Molecular Beam Epitaxy (MBE) was developed in late 1960s by J. R. Arthur and A.Y. Cho working at Bell Telephone Laboratories. It works in ultra high vacuum conditions (P $= 10^{-11}$ Torr) and is used to make compound semiconductor with atomic level precision and extremely high purity. In order to fabricate high quality semiconductor devices, it is required that the layers be deposited at rates between 0.001 and 2 monolayer/second which can only be currently achieved with MBE. In an MBE system, each element is delivered separately via molecular beams and the atoms or molecules in gaseous form travel to the substrate where they react to form the desired compound. Since the elemental sources are in separate cells, the choice of the elements and their relative concentrations can be adjusted for any layer, which precisely defines the composition of that layer and by extension, its electical and optical characteristics. This is the most important aspect of MBE wherein there is an extremely high control over layer thickness, composition and purity due to the low growth rate and thus layers of only a few atoms thick can be produced reliably. The Asaro-Tiller-Grinfeld (ATG) instability is an elastic instability commonly encountered during MBE growth. In case of a lattice mismatch between the growing film and the substrate, elastic energy is accumulated in the growing film. At a critical height, the free energy of the film can be lowered if the film breaks into isolated islands, where the tension can be relaxed laterally. This critical height depends on Young's moduli, mismatch size, and surface tension. This instability has been researched to get some applications, such as assembling quantum dots and is also known as Stranski-Krastanow growth mode.

GaN nanowires have been synthesized with excellent quality using MBE on various substrates. Calarco and coworkers[76] were the first to demonstrate the growth of GaN nanowires on a Si(111) substrate. They studied the evolution of nanowire growth with time under a set of growth conditions and observed that the wire density increased rapidly with time and then saturated. Bertness *et al.*[77] also studied the growth of GaN nanowires grown under various different set of parameters such as variation in nitrogen to gallium flux, thickness of AlN buffer layer and substrate orientation. They were able

to establish that the growth mechanism included the formation of nanocolumns in the AlN layer, and the propagation of GaN nanowires was driven by the differences in growth rates among various crystallographic planes under nitrogen rich conditions. Due to the immense amount of reports on catalyst mediated growth mechanism, early work in the field of MBE growth of GaN nanowires followed the same hypothesis wherein it was speculated that the growth proceeded through the formation of nanoscale Ga droplets acting as self catalysis particles[78,79]. However, since these so-called droplets were never observed on the nanowire tips, the explanations for the growth of nanowires became varied. A lot of factors inherent to MBE growth, such as high growth temperature, desorbtion of Ga adatoms, slow growth rates, high sensitivity to surfactants and consistent crystallography indicated that the growth was promoted through surface diffusion and variation in sticking coefficients of adatoms[80], which led to the development of differential sticking coefficient model[77,81,82]. Theoretical estimations of surface energies and diffusion constants provided more support to the model[83] combined with testing in conditions not commonly employed, such as rapid cooling during the progression of growth[81] and intentional formation of Ga droplets[84]. Growth rates cannot be quantitatively predicted with this model and the fact that needs to be incorporated is that the three dimensional geometry would alter the growth rate by itself because of the difference in average flux at the top and sides of the walls, as the top receives five or six times more adatoms compared to sidewalls[85]. For nanowire growth, the evidence in the reports of Calarco[76,86] suggest a significant contribution of Ga adatoms in the nanowire growth which either deposit on the top of the wires or arrive at the sidewalls and diffuse to the top. This predicts thin and long nanowires being grown, which has seen variation in the experimental findings . Tchernycheva *et al.* were also able to grow free standing GaN nanowires on Si (111) substrates under catalyst free mode using plasma enhanced molecular beam epitaxy[87]. They obtained cylindrical nanowires with a hexagonal cross section defined by $[10\bar{1}0]$ planes and diameters down to 20 nm. Changing the III/V flux ratio also tuned the lateral/axial growth rate ratio from ≈ 1 % to ≈ 10 %. Rafael Mata and coworkers used plasma assisted molecular beam epitaxy to grow GaN nanowires on Si(111) as a function of temperature and it was found that the density, diameter and length of the nanowires depended strongly on the growth temperature[88].

The application of GaN in UV/blue emitters and high temperature/power electronic devices is well known. Due to its low electron affinity, high carrier mobility and physical/chemical stability it is also useful as a field emitter. The nanowires, due to their cylindrical geometry and strong two dimensional confinement of sub atomic particles, are attractive candidates to fabricate nanoscale electronic and optoelectronic devices[34]. Their potential has already been demonstrated in fields such as photovoltaics, light emitting devices (LEDs), field effect transistors (FETs), lasers, photocatalysts and nanogenerators.

2.1.3   Application of nanowalls to improve light emission

Nanowalls are two dimensional nanostructures which hold promise in fields requiring large surface areas, such as sensors[89] and solar cells[90]. They have been fabricated using a wide variety of materials over the past decade[41,91–98] and their applications ranging from proof-of-concept gas sensors[99–101], nanogenerators[102] and photoconductors[103] have been shown. Among the many materials used for this structure, ZnO is the primary semiconductor of choice due to its fast electron transport[101,104] and hence has been extensively grown and studied[44,48,105–114]. GaN is being considered due to its ability to alloy with other group-III materials to get a tunable band gap. There have been relatively fewer reports of growth of GaN nanowalls[115–120] and hence it is interesting to study GaN nanowalls in greater detail to probe its potential for various applications. Some interesting properties of GaN nanowall network structures, such as in-plane electrical conductivity are predicted to be useful to fabricate electrical devices. Recent focus has, however, been to devise sensors due to its high surface to volume ratio.

Nanowalls can be grown using techniques similar to those used for growing 1D nanowires through spontaneous self assembly. The earliest known report of fabricating GaN nanowalls is by Gautam *et al.*[95] who initially obtained GaS and GaSe nanowalls by thermal treatment of the respective powders. GaN nanowalls were then formed by reacting the GaS and GaSe nanowall samples with NH_3. There have been instances where both nanowire and nanowall growth has been achieved in a single film[91,102]. It has been observed that the nanowalls form a network among the nanowires and grow taller near the nanowires, which suggests a sharing of precursors between the two nanostructures[107]. Kumar *et al.*[102] have observed the growth of nanowires after

a nanowall growth has occurred. The nanowires grow at the junction of the nanowalls which has led to the hypothesis that the precursor adatoms could be clustering at these points acting as nucleation points for nanowire growth. Evolution of nanowires into nanowalls[108] has further reinforced the belief that there are regimes of preferred growth of these one and two dimensional nanostructures. In this area, the exact nature of the competition between the growth modes of the two nanostructures is poorly understood, and a comprehensive understanding of the nanostructure growth mechanisms and the option to choose between the two modes is needed in order to allow a rational synthesis of pre conceived nanostructures. Brewster *et al.*[121] have performed the growth of ZnO nanowalls in a horizontal tube furnace by changing the source flux. The growth evolved from nanowires which formed at shorter growth times on the ZnO film to nanowalls. The nanowires incorporated into the film to form nanowall structure at 20 minutes and at 40 minutes there were only nanowalls remaining. Since both the nanowires and nanowalls grew from the film surface, they shared the same mechanism of growth which consisted of a combination of catalyst assisted and non assisted method. After the formation of nanowires, the nanowalls grow due to geometric situations as follows: the sidewalls of nanowires are no longer the preferential sites for adatom incorporation, the film height increases to an extent that the precursor collection area of the film is in competition with the nanowires for further growth. Adatoms also diffuse between nanowire sidewalls and the nanowall growth edge which is shown to be a preferential diffusion process as the areas of concave structures are favoured over convex structures. Shi *et al.*[107] in their experiments with ZnO nanostructures observe a cluster drifting effect and propose a mechanism for the growth of the nanostructures. Since they followed a vapour deposition process, controlling the concentration of the reactant vapor allows rapid surface nucleation to a point where a three dimensional nanowall morphology is obtained but not upto the mark where two dimensional epitaxial layers get deposited. It is very apparent from their results that the formation of such a structure is independent of the susbtrate or any nanowires forming elsewhere. The general mechanism according to them stems from the drifting of the Zn clusters which get deposited on the substrate due to heterogenous nucleation carried out at high temperatures. This drifting leaves a trace which favors further deposition through a vapor-solid process. For the formation of a nanowall network, the authors hypothesize that the highly dense clusters collide among each other leading

to nucleation with a network shaped trace. These clusters would also initiate a nanowire growth due to favorable thermodynamic conditions. The space between the nanowires would be filled with ZnO crystals resulting in a nanowall structure. As the motion of the Zn clusters is Brownian which ultimately leads to the formation of nanowalls, there is no relation between the structure and the substrate lattice, although the film as a whole demonstrates epitaxy.

Kesaria *et al.*[119] intentionally grew GaN nanowall network structures for the first time. They were able to form epitaxial nanowalls by plasma assisted molecular beam epitaxy on c-sapphire substrate. It was interesting to note that these structures formed purely through kinetic control of the reacting species and no catalyst or pre-treatment of the substrate was needed. Although nanowalls of GaN have been formed earlier by photoelectrochemical etching[120] and other chemical etching methods[122], structures grown using MBE show better optical qualities and are much more stable. Formation of a crystalline nanostructure follows the crystal growth theory[123,124], which comprises of three basic mechanisms; spiral growth at screw dislocations (BCF theory)[125,126], layer by layer (LBL)[126,127] growth and dendritic growth. The most favoured mechanism is the one that is governed by supersaturation, defined as $\sigma = ln(\frac{c}{c_o})$, where c and c_o are the precursor and equilibrium concentrations, respectively. Screw dislocations play a pivotal role at low supersaturations as the self-perpetuating step provided by screw dislocation growth spirals allows crystal growth at saturations lower than what is required for 2 dimensional (LBL) growth. It has been shown that screw dislocations can indeed drive the growth of 1 dimensional structures such as nanowires[124,128–132], nanotubes[130] and even two dimensional structures like nanoplates[133]. Indeed, Kesaria *et al.*[119] invoke the same BCF theory to explain the formation of nanowalls in their case. However, since the growth takes place on low index c-sapphire surface in high supersaturation conditions, there is a higher probability of two dimensional nucleation as defined in the crystal growth theory. Therefore, it is imperative that the mechanism of the self assembled nanowalls be further probed and many experiments are remaining to be done. Zhong *et al.*[115,116] have explored the growth of GaN nanowall network structures using MBE on Si (111) surfaces and have been able to tune the porosity of the film by changing the Ga:N ratio. They were able to conclude that the network structure is under low

stress and possesses good optical quality. The GaN nanowall is a novel structure and is shown to grow on various substrates, but the exact mechanism of its evolution is still to be explained. It is important to understand how the structure forms, as this structure would be useful in fields where a large surface to volume ratio is needed, such as gas sensors and photovoltaics. In comparison to separated nanostructures such as quantum dots and nanowires, an interconnected morphology is also promising when it comes to fabricating a device structure.

Chapter 3

Experimental Details

3.1 Introduction

This chapter deals with the various experimental tools employed for the work reported in this thesis. It is organized in the following order: first, the thin film growth methods used to grow GaN and Ag, namely the plasma-assisted molecular beam epitaxy (PA-MBE) and the physical vapour deposition (PVD), respectively will be discussed. Next, the characterization methods used throughout the thesis would be elaborated, under the headings: structural, optical and electrical, explained in that order. For structural characterization, the techniques used and described in this section are field emission scanning electron microscopy (FESEM) and high resolution X-ray diffraction (HRXRD); and for electronic structure and composition, X-ray photoelectron spectroscopy (XPS) is used. For optical characterization, Raman spectroscopy as well as the phenomenon of surface enhanced raman scattering (SERS) was used along with photoluminescence (PL), which was measured both by a xenon lamp source as well as a He-Cd laser at room temperature and low (liq. N_2) temperatures. The transport properties were determined by four probe method, magnetoresistance (MR) and photoconductivity (PC).

3.1.1   Thin film growth

The PA-MBE system is the primary film growth technique used in this work and will be discussed first followed by the electron beam evaporation method in the PVD system which was used to deposit Ag on the GaN films.

Molecular Beam Epitaxy

The GaN films were grown on c-sapphire substrates using PA-MBE (SVT, USA) at growth temperatures ranging from 580 °C to 780 °C. The base pressure of the system is maintained at 1.0×10^{-11} Torr. A schematic of the system, is shown in Figure 3.1.
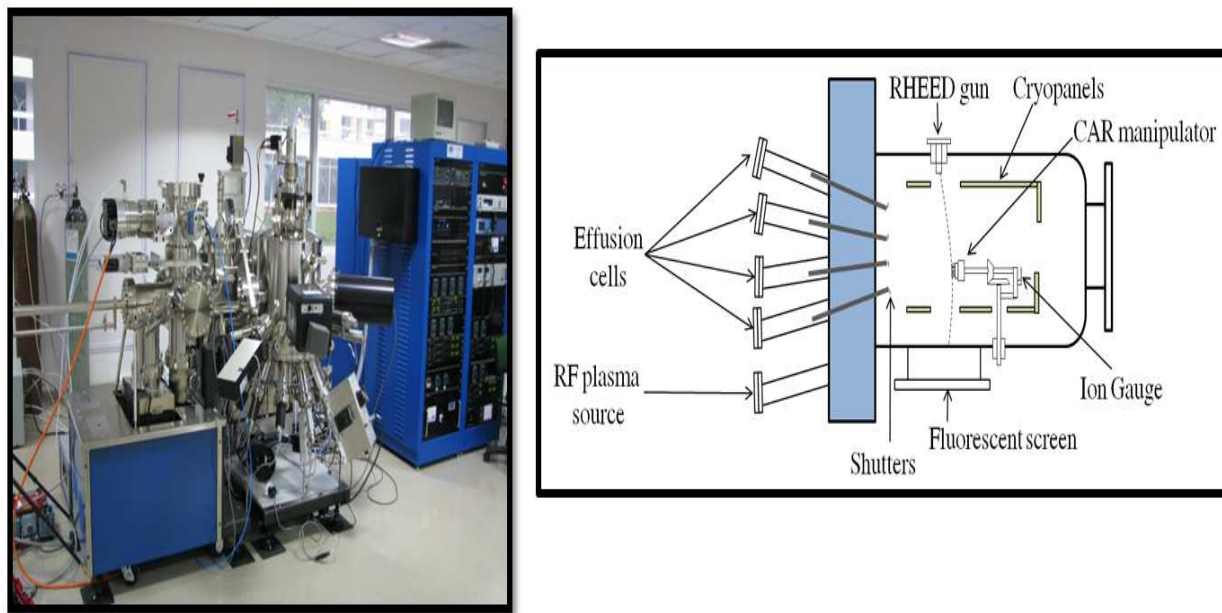
Figure 3.1: Schematic of the MBE system

Elemental gallium and gaseous nitrogen were used as sources. The gaseous nitrogen was flown at rates between 2 and 6 sccm for various samples and at forward plasma powers ranging between 200 and 400 W. All the substrates were chemically pre-cleaned using isopropyl alcohol (IPA), ethanol and acetone in that order before being introduced in the load lock chamber. Thermal cleaning was carried out in the preparation chamber at 600 °C for one hour at a ramp-up rate of 5 °C per minute. The preparation chamber is pumped using a turbo molecular pump (TMP) backed by a diaphragm pump as well as an ion pump to maintain the pressure. After outgassing in the preparation chamber, the

substrates are transferred to the growth chamber where they are placed on the continual azimuthal rotation (CAR) manipulator. The samples are then annealed in ultra high vacuum (UHV) conditions of 5×10^{-10} Torr at 800 °C for half an hour. An ion gauge located on the back of the CAR is used to measure the growth chamber pressure when pointed away from the source and the beam equivalent pressure (BEP) when facing the sources. The surface cleanliness is confirmed by reflection high energy electron diffraction (RHEED) studies which show characteristic streaks which are the Kikuchi pattern for a clean, uncontaminated, single crystalline surface. The growth chamber is pumped by a TMP-diaphragm pump system and an ion pump and also consists of a cryo-panel cooled by liquid nitrogen to ensure minimal degassing even at higher growth temperatures. Elemental gallium is obtained by evaporating metallic gallium which is kept in cylindrical cells made of ceramic attached to the growth chamber via metal containers. These cells are known as Knudsen cells (or K-cells) and are typically kept at ≈ 100 °C to avoid any contamination. The flux of gallium being introduced into the growth chamber is controlled by the temperature of the K-cell which also determines the growth rate along with the forward plasma power and the temperature at which the growth stage is maintained, which is measured using a thermocouple located on the CAR heater. Typical values of the Ga K-cell used in this study ranged from 1000 °C to 1100 °C which gave a growth rate of ≈ 0.3 μm/h. A chiller kept at a temperature of 16 °C is used to flow water around the K-cells to keep them cool during growth. The molecular beam condition that the mean free path λ should be greater than the geometric size of the chamber is easily fulfilled if the pressure does not increase beyond 10^{-5} Torr. Due to the UHV conditions employed, λ is of the order of kilometers which also ensures uniformity of the film as shown in Figure 3.2. Though the MBE grown films provide excellent control over layer composition and thickness, the deposition rate is very low.

There are various *in-situ* characterization techniques used in an MBE system. In this study, flux rate of each species was monitored using an atomic absorption spectrometer (IS4K, SVT) and the surface was probed using reflection high energy electron diffraction (RHEED). The RHEED pattern and oscillations are indicative of the growth mode and the smoothness of the surface. Further, a computer controlled shutter employed at the mouth of each K-cell can open and close at high accuracy which allows the composition
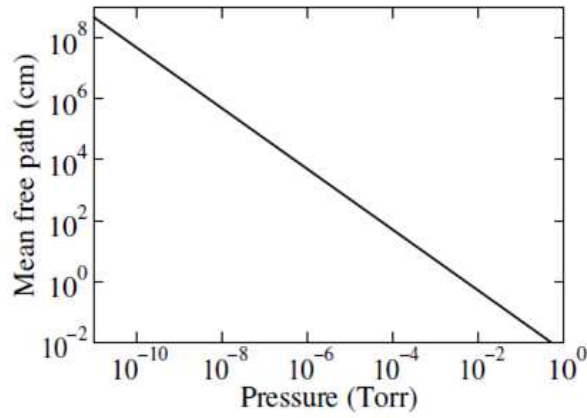
Figure 3.2: Mean free path of nitrogen molecules at 300K

and thickness of each layer to be controlled with high precision making the growth of superstructures quite easy. The mass evaporation rate per unit area of a source surface is given by the Langmuire-Knudsen relation[134]:

$$\Gamma_e = N_A \alpha_e \frac{P^* - P}{\sqrt{2\pi MRT}} \tag{3.1}$$

where N_A is the Avogadro's number, R is the gas constant, α_e is the sticking coefficient $(0 \leq \alpha \leq 1)$ and M and P^* are the molecular mass and vapour pressure of the evaporant, respectively. The maximum evaporation rate is obtained in vacuum where P = 0 and α_e = 1. An expression for the maximum value of Γ_e is given by:

$$\Gamma_e = 5.834 \times 10^{-2} \sqrt{\frac{M}{T}} P^* \tag{3.2}$$

At pressures of 10^{-2} Torr, Γ_e is of the order of $10^{-4} gcm^{-2}s^{-1}$. The film deposition rate also depends on the distance between the source and the substrate and on the emission angle. For a K-cell, where the aperture is very small (area of A_e) through which the evaporated atoms diffuse; and the aperture size is small compared to the source to substrate distance, the source can be approximated to be point-like and the mass deposition rate per unit area of the substrate R (g $cm^{-1}s^{-1}$) is given by:

$$R = \frac{\Gamma_e A_e}{\pi r^2} \cos\theta \cos\phi = 1.856 \times 10^{-2} A_e \sqrt{\frac{M}{T}} P^* \frac{\cos\theta \cos\phi}{r^2} \tag{3.3}$$
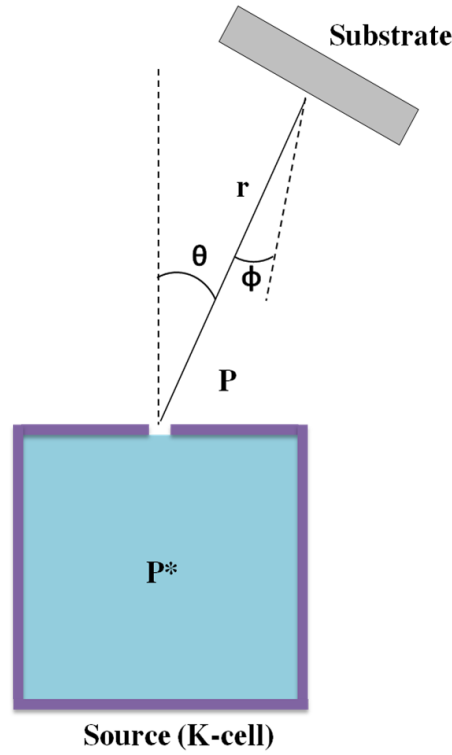
Figure 3.3: Angle dependence of deposition for a K-cell

Figure 3.3 reveals that the deposition rate varies across the substrate. For a substrate of diameter D placed exactly above the source, the mass deposition rate on the center of the substrate R_1 and on the edge R_2 are proportional to:

$$R_1 \alpha \frac{1}{r_1^2} \tag{3.4}$$

$$R_2 \alpha \frac{1}{r_2^2} \cos^2 \theta = \frac{r_1^2}{r_2^4} \tag{3.5}$$

Defining the uniformity as

$$\sigma(\%) = \frac{R_1 - R_2}{R_1}(\%) \tag{3.6}$$

we get

$$\sigma(\%) = 1 - [1 + (\frac{D}{2r_1})^2] \approx \frac{D^2}{2r_1^2} \tag{3.7}$$

For comparison, thickness uniformity of 1 % on a 10 cm diameter surface requires r_1 of at least 70 cm; though this distance would be doubled for practical reasons. Such large r values needed for thickness uniformity of the deposited film require large chambers and pumps with high pumping speeds which consequently make deposition rates low and wastage of large amount of evaporant materials, and thus is collimated by using a tubular K-cell.

Physical Vapour Deposition

The PVD system consists of both a thermal evaporation as well as an electron beam evaporation method to sublimate a solid target in order to coat a film on the substrate of choice. In this work, electron beam (or e$^-$ beam) evaporation method has been used to evaporate Ag which was in the form of a wire (Alpha Aeser, 99.9999% pure) onto the GaN films. A schematic of the system is shown in Figure 3.4.
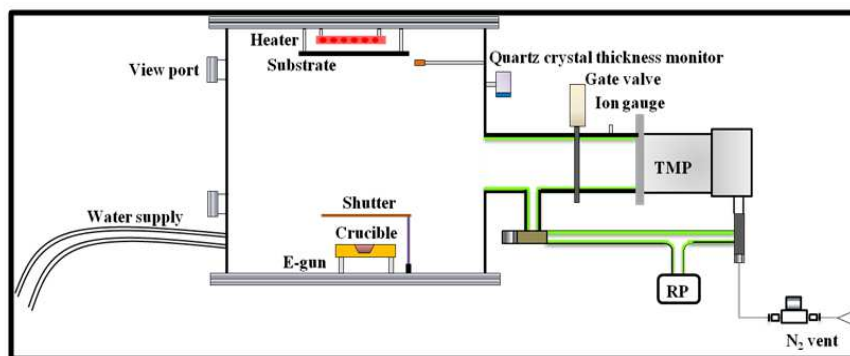
Figure 3.4: Schematic of the PVD system

Electron beam evaporation is essentially a PVD technique in which an electron beam of high intensity is generated from a filament and controlled using electric and magnetic field to divert its path so as to strike a target (Ag in this case) which vaporizes it within a vacuum environment. Upon sublimation, the source atoms would traverse the vacuum

chamber in a plume which at low thermal energies (less than 1 eV) and coat a substrate placed directly above the target. Average working distances are between 300 cm to 1 meter based on the mean free path which depends on the vacuum conditions. In our case, the chamber has a base pressure of 1.0×10^{-8} Torr, pumped by a TMP backed by a rotary pump as well as an ion pump. This allows convenient working distances of $\approx$ 300 cm in the chamber. A water cooled copper block is typically used to hold the target material in a crevice which is bored out of it in the shape of an inverted and truncated cone. A magnetic assembly consisting of a permanent magnet and two pole extensions are placed close to the block in such a way that their field lines run parallel to one side of the block. Below these field lines, there is a filament which produces electrons via thermionic emission which is collated into a beam. This electron beam is focused and steered using the field lines, typically in a 270 ° arc to impinge on the center of the crevice. The energy of the electron beam is also controlled so as to make it fall directly at the center of the crucible. The voltage applied to produce the electron beam is 5.45 kV in the present experiment and the Ag is deposited at an emission current of 5 mA. The main advantage of using electron beam evaporation over thermal is that the higher energy transferred to the target allows a denser plume to form which yields a denser film with an increased adhesion to the substrate. Also, since the electron beam only heats the target and not the crucible, there is a significantly lower degree of contamination from the crucible. It is also possible to heat multiple crucibles in order to deposit multiple materials without breaking the vacuum. The electron beam also leaves behind a small part of the target in the crucible which typically covers the crucible and is termed as a 'skin' which prevents the crucible from deteriorating and hence the same crucible can be used for multiple depositions of the same material with even lesser chance of contamination. Since the electron beam generates a lot of heat, it is imperative to cool the system before initiating the deposition. For this reason, water lines are connected to the electron gun and water is flown using the same chiller as mentioned above before starting the deposition. The thickness of the deposited film is measured using a quartz crystal thickness monitor (QCTM).

3.1.2   Structural characterization

This section discusses in detail the experimental tools and methods used in the structural characterization of the GaN films such as FESEM, HRXRD, XPS, Raman and SERS.

FESEM

The imaging of the samples was carried out using an FESEM system (Quanta line, FEI, Netherlands) operating at an accelerating voltage of 20 kV. The system can accommodate upto seven samples on a rotating stage and operates under high vacuum conditions. The working distance (distance between the electron gun and the sample) in this work was kept at 15 mm, which allowed for a maximum sample tilt of 45 ° from the normal. In addition, the system also encompasses an electron dispersive x-ray analysis (EDS) and cathodoluminescence (CL) as additional characterization tools.

Working principle

The FESEM operates under high vacuum conditions (P $\leq 10^{-7}$ Torr) which helps the electron beam collimate along the column while also preventing discharges inside the gun zone. The source used for the generation of electrons is an electron gun typically employing a filament made of LaB_6 fashioned into an extremely small tip radius ($\approx$ 100nm). The major difference between a conventional SEM and an FESEM is the way the electrons are generated from the filament. In the SEM, the filament is heated and electrons are released by the process of thermionic emission; the filament in FESEM is placed in an extremely high electrical potential gradient. Since the filament tip radius is very small, a very high electric field is concentrated which magnifies the field to such an extent that the work function of the material itself is lowered enough so that the electrons can leave the filament. As there is no heating involved in the electron emission, FESEM is also known as a cold cathode emitter. The images produced by an FESEM are cleaner, have less electrostatic distortions and spatial resolution (< 2nm) which is 5 or 6 times better than an SEM. Two anodes are used for focusing in the FESEM. A voltage of $\approx$ 0-5 kV between the field emission tip and the first anode, called the extraction voltage,

controls the current emission (1-20 mA). Another voltage (1-30 kV) applied between the second anode and the cathode, called the accelerating voltage, increases the beam energy and determines the velocity at which electrons move in the column. This voltage along with the beam diameter determines the resolution (capacity to resolve two closely spaced points as two separate entities). With higher accelerating voltages, better resolution can be achieved. The resolution of the FESEM used is $\approx$ 5 nm.

1. Field emitter
2. Anode
3. Multi-hole aperture
4. Gun/aperture alignment system
5. Condenser lens
6. Stigmator
7. Linear tube
8. In-lens detector
9. Objective lens
10. Scan coils and stigmator
11. Objective cap
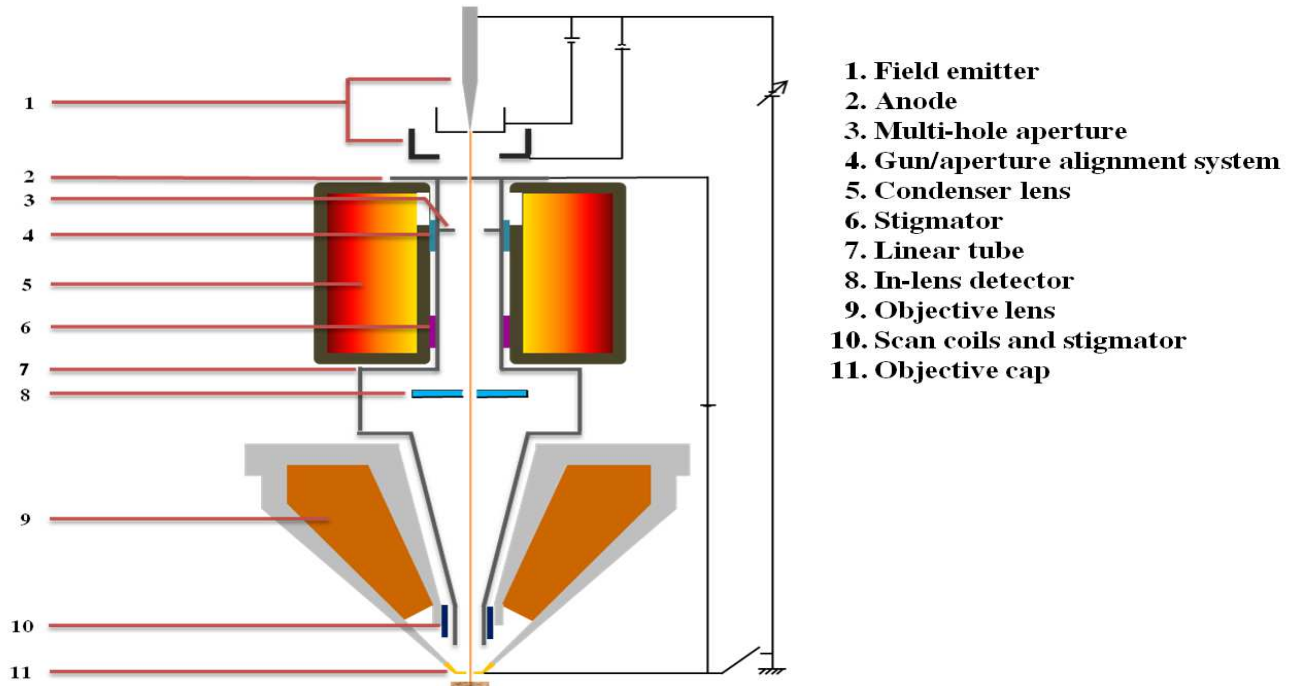
Figure 3.5: Electron optics described in a schematic

Figure 3.5 shows a schematic of the electron optics in an FESEM assembly. Field emitter (1) emits the electrons which pass through the anode (2) aperture. The electron beam then passes through a multi-hole aperture (3) which is typically 30 μm in diameter. If needed, other aperture sizes can be selected by using the gun/aperture alignment system (4). The condenser lens (5) controls the amount of demagnification of the electron beam. The current in the condenser lens determines the diameter of the beam. A small current produces a narrow beam which provides better resolution, but the signal to noise ratio is also worse. The stigmator (6) ensures that the beam is rotationally symmetrical by correcting irregularities in the x and y directions. A circular beam is important as elliptically shaped beam produces blurry and stretched images. Anode and linear tube (7) are connected to form the beam booster which provides better protection against stray fields. Objective lens, consisting of electromagnetic (8) and electrostatic (9) lenses, is the

lowest lens in the column and it focuses the electron beam onto the specimen. At short working distances, the objective lens has to apply a higher force to deflect the electron beam which produces the smallest beam diameter. Although this gives better resolution, the depth of field (range in vertical direction in the object where it can still be viewed clearly) is poorer. The deflection system consists of a set of scan coils (10) which are used to raster the beam across the sample surface. Image appearance occurs in sync with this movement of the beam. The velocity with which the beam moves determines the refreshing rate of the image on the computer screen and the noise in the image (rapid scan leads to low signal and higher noise). Magnification also increases if the scanned region is smaller keeping the window size constant. Scan coils are typically composed of upper and lower coils which prevent the formation of a circular shadow at low magnification.

HRXRD

HRXRD of the samples was performed on a Discover D8 system (Bruker) in both the $\theta - 2\theta$ as well as the Rocking curve modes. X-rays were produced by a Cu K$_\alpha$ source and a 4-bounce Ge (220) monochromator was used to get high resolutions.

Working principle

X-ray diffraction works on the principle of Bragg's law which states that for X-rays falling on a set of equidistant parallel planes hkl separated by an interplanar distance of d_{hkl}, constructive interference will be observed for those x-rays reflected from the lattice planes by a specular angle that have a path length difference between them as an integral multiple of the wavelength:

$$n\lambda = 2d\sin\theta \tag{3.8}$$

The interplanar spacing is related to the lattice parameters for a hexagonal lattice by the following relation:

$$\frac{1}{d_{hkl}^2} = \frac{4}{3a^2}[h^2 + k^2 + hk + l^2(\frac{a}{c})^2] \tag{3.9}$$
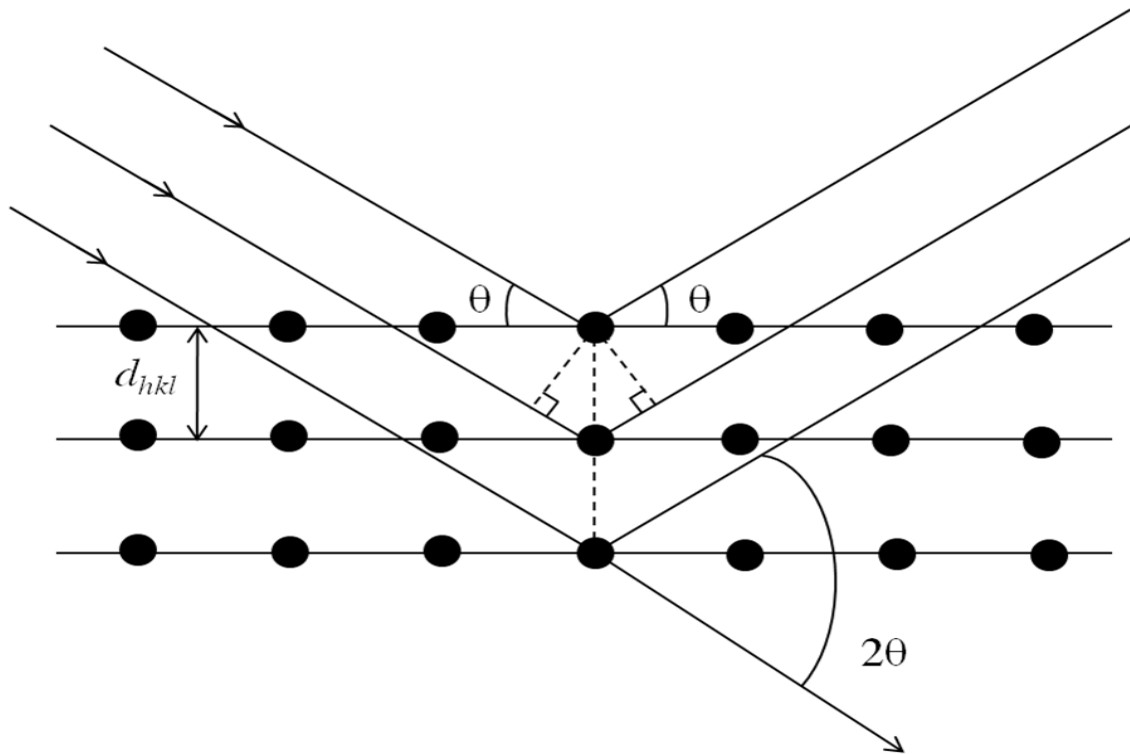
Figure 3.6: Bragg's law represented diagramatically; diffraction occurs only if the incident ray undergoes specular reflection from a given set of parallel planes

In crystalline samples, diffraction peaks can give important information about the lattice planes, strain, texture etc of the material. Some of the information obtained using XRD for this work will be discussed later in this section. There are different measurements in an XRD instrument based on this principle. The most common one is a $\theta - 2\theta$ measurement wherein the interplanar spacing d can be measured.

A symmetric $\theta - 2\theta$ scan is performed in order to measure the interplanar distance of the planes parallel to the sample surface. Here, the angle θ of the incoming beam with respect to the sample surface is modified while simultaneously keeping the detector at an angle of 2θ with respect to the incoming beam. The angle θ at which a diffraction peak is observed, can then be used to give the interplanar distance according to the above equation. For determining the interplanar distance of a set of planes tilted by an angle with respect to the sample surface, an asymmetric $\theta - 2\theta$ scan is performed. Similar to the case of a symmetric scan, the detector is placed at an angle of 2θ with respect to the incoming beam. The incoming beam in this case makes an angle of ψ with respect to the sample surface. It should be noted that $\theta - \psi$ is a fixed offset while scanning through θ values.
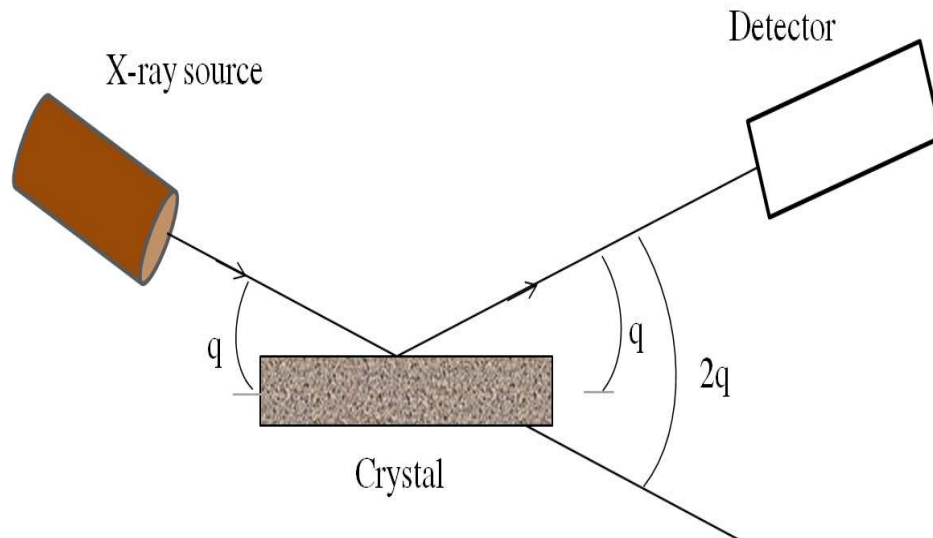
Figure 3.7: symmetric scan geometry in an XRD setup

An alternative to the asymmetric scan method is the skew-symmetric measuring geometry. As in the case of the symmetric scan, the incoming beam forms an angle ψ with respect to the sample surface, while the detector is kept at 2θ. Here, the deviation is that the sample is tilted over a fixed angle of $\chi = \psi$ around the axis parallel to the sample surface and the plane of the incoming and outgoing beams.

The determination of the interplanar distance with a $\theta - 2\theta$ measurement does not only allow to identify the phases present in the specimen, but also to determine the epitaxial stress and strain. Stress and/or strain result in the deviation of the interplaner distances within a crystal from a relaxed thin film. The full width at half maximum of the diffraction peak is inversely proportional to the thickness of the crystalline layer. The full width at half maximum (FWHM) of the peak is given by the Scherrer formula:

$$\text{FWHM} = 0.9 \ \lambda/t \cos(\theta B)$$

where the FWHM is expressed in radians, λ is the wavelength of the X-rays, t is the thickness of the layer and θB the Bragg angle of the reflection. A non-perfect crystal can be divided into different crystalline domains (crystallites) that have a different orientations. This occurs if long ranging stacking faults and other extended defects are present in the sample. The thickness t in the Scherrer formula will, in that case, be related to the crystallite particle size. Another kind of scan commonly carried out while performing HRXRD on crystalline thin films is the Rocking Curve (RC). This scan allows
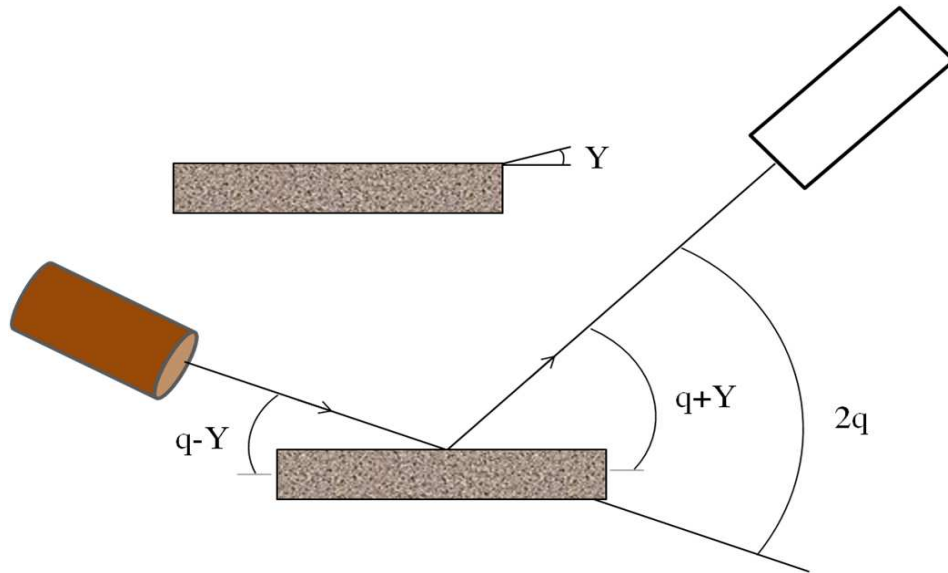
Figure 3.8: Asymmetric scan alignment in XRD

one to determine the mean spread in orientation of the different crystalline domains of a nonperfect crystal. It is also possible to determine the size of a crystal if it is very small. In order to perform a RC scan, it is mandatory to first carry out a $\theta - 2\theta$ scan in any geometry. Next, the incident angle θ and the detector position 2θ, is fixed at the Bragg angle of the corresponding reflection plane. The RC measurement is then taken by varying the orientation of the angle around its position by an angle $\Delta\omega$ while keeping the detector position fixed. The width of the rocking curve peak has several determining factors. The major contribution comes from the spread in crystalline orientation between various domains. The width of the peak is usually expressed in terms of Full Width at Half Maximum (FWHM) W, and W_{tt} is the mean spread in orientation for the given set of planes belonging to the chosen Bragg reflection. Another factor contributing to the peak width is the lateral size of the domains. This broadening is defined as:

$$W_{inc} = \frac{\lambda}{2b\sin(\theta_b)} \tag{3.10}$$

where b is the mean width of a particle. The last contribution comes from the detector resolution W_d. The present D8 Discover system has a resolution of $< 0.005°$ when the monochromator is mounted. This factor is usually neglected as the other two factors are much larger in comparison. The total FWHM is then calculated as a combination of these three factors:
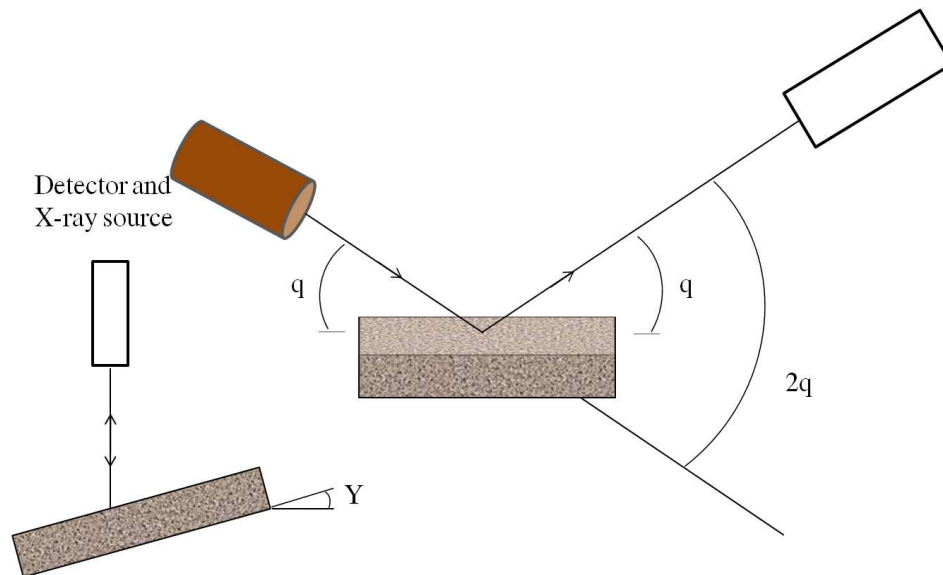
Figure 3.9: Skew-symmetric scan configuration for XRD

$$W^2 = W_{tt}^2 + W_{inc}^2 + W_d^2 \qquad (3.11)$$

XPS

X-ray Photoelectron Spectroscopy (XPS), also known as Electron Spectroscopy for Chemical Analysis (ESCA) is the most widely used surface analysis technique since it can be used to probe a broad range of materials and provides valuable quantitative and chemical state information from the surface of the material being studied. A system purchased from Omicron was used in the present study. The beam energy varied from 0.5 kV to 5 kV giving a maximum target current of 59.3 and 130.1 μA, respectively. Beam energy was 5 keV when the spot size was small while for the broad spot mode the best results were obtained at 1 keV. The average depth of analysis for an XPS measurement is approximately 5 nm. Spatial distribution information can be obtained by scanning the micro focused x-ray beam across the sample surface. It is also possible to obtain depth distribution information by combining XPS measurements with ion milling (sputtering) to characterize thin film structures. Surface information provided by XPS is important for many industrial and research applications where surface or thin film composition plays a critical role in performance including nanomaterials, photovoltaics, catalysis, corrosion, adhesion, electronic devices and packaging, magnetic media, display technology, surface

treatments, and thin film coatings used for numerous applications.

Working principle

Figure 3.10 provides a schematic of the XPS process, which works on the principle of photoelectric effect wherein the surface of a sample is bombarded with mono-energetic Al k_α x-rays causing photoelectrons to be emitted from the sample surface. An electron energy analyzer is used to measure the energy of the emitted photoelectrons. From the binding energy and intensity of a photoelectron peak, the elemental identity, chemical state, and quantity of a detected element can be determined.

The energy of the incident x-ray is given by the Einstein relation:

$$E = h\nu \tag{3.12}$$

where h = Planck's constant $(6.62 \times 10^{-34}$ J.s) ν = frequency of the radiation in Hertz

In order to escape the atom, an electron must overcome the binding energy of the shell it is in along with the work function of the material. The kinetic energy of an emitted photoelectron is then given as:

$$K.E. = h\nu - B.E. - \phi \tag{3.13}$$

For materials showing correlation between electrons, an additional term 'U'' is also included in the right hand side of the equation.

X-ray sources

An X-ray tube comprising of a hot filament kept at a high voltage, usually between 10-15 kV and a current of 10-15 mA emits the electrons. The electrons are accelerated towards a grounded potential anode which is water cooled to maximize the current. Since the anode material determines the wavelength of the X-rays produced, it is usually chosen in such a way that the photoemission peak from all the atomic levels of all the elements in the periodic table give a good intensity. A rule of thumb is that the incident energy should

be at least three times the binding energy of the electron in order to obtain a reasonable emission peak. Further considerations include that the anode's own photoemission peak should be as narrow as possible to obtain good resolution. The most popular elements that meet these requirements are aluminium and magnesium. Both the elements are usually combined in a twin-anode configuration in a single electron gun providing AlK_α or MgK_α photons of nearly same X-ray energies of 1486.6 and 1253.6 eV, respectively.
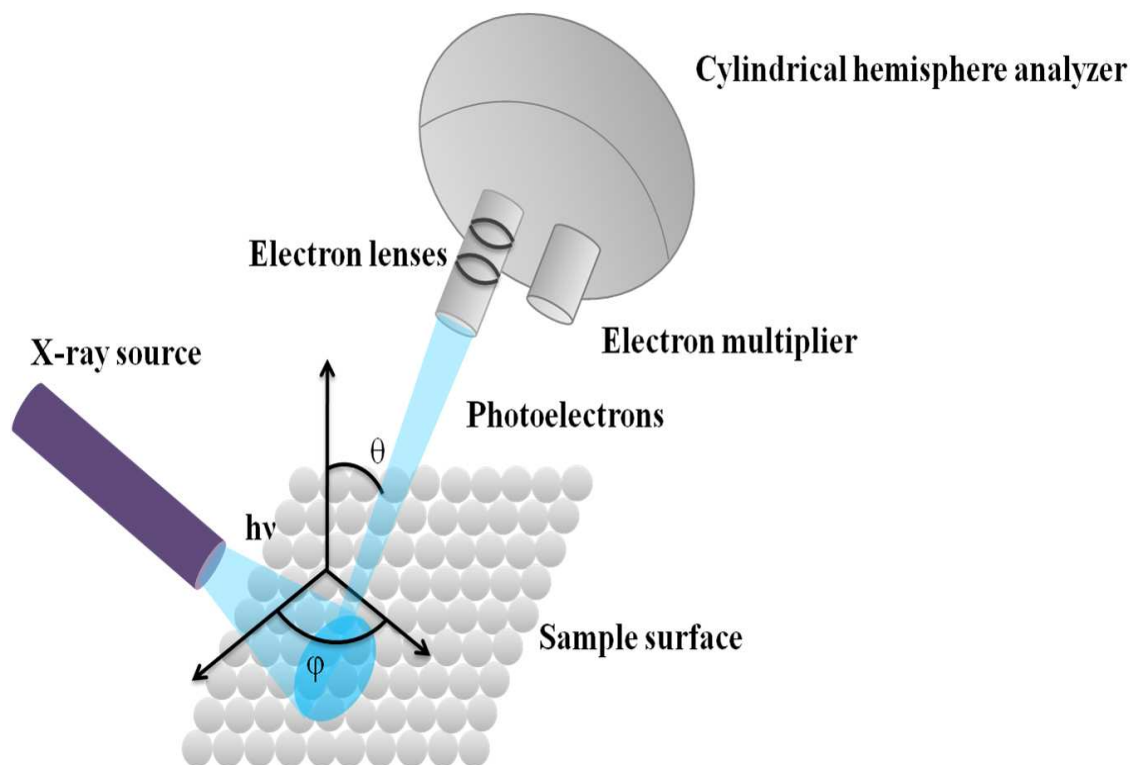
Figure 3.10: Schematic diagram of an XPS process

Energy analyzers

Analysis of an XPS spectrum is essentially dependent on identifying the photoeletron energies. This makes the electron energy analyzer the most important component in an XPS experiment. A single photoemission peak can consist of more than one component, which makes it mandatory to understand about the resolution of the peak. Energy resolution can be either absolute, defined as the aforementioned FWHM of that peak with an energy of ΔE, or relative, which is expressed as the ratio of ΔE to the KE of the peak position. The absolute resolution should be the same for all energies while performing an XPS measurement. There are two main types of energy analyzers used in XPS: cylindrical mirror analyzer (CMA) and the hemispherical sector analyzer (HSA),

which is also known as concentric hemispherical analyzer (CHA). The CMA is used when there is no need to achieve the highest possible resolution. The development of HSA came about with the need to get good spectral resolution which plays a key role in XPS analysis. Addition of a transfer lens and multichannel detecttion increases its sensitivity to the point where both high transmission and high resolution are obtained. There are two concentric cylinders in a CMA; the inner one is grounded while the outer one is at a negative potential. Many times an electron gun is coaxially mounted within the analyzer. The CHA uses an electric field between two hemispherical surfaces to disperse the electrons according to their kinetic energies. Concentric hemispheres with radii R_1 and R_2 are kept at negative potentials of -V_1 and -V_2 ($V_2 > V_1$). Electrons arriving at the analyzer entrance with an energy of E=eV_0 are focused at the exit only if the following condition is met:

$$V_0 = \frac{V_1 R_1 + V_2 R_2}{2R_0} \tag{3.14}$$

which determines the potential of mean free path analyzer through radius R_0 (equipotential surface between R_1 and R_2). Changing V_1 and V_2 allows scanning the electron kinetic energy following the mean free path through the hemispheres. The resolution is given by $R = \frac{\Delta E}{KE}$ which, being energy dependent, is non-uniform over the XP spectrum. Uniformity is achieved by retarding the electrons entering the analyzer to a fixed kinetic energy called the pass energy E_0 so that a fixed resolution is applied across the entire spectrum. This can further be tuned by decreasing E_0 or increasing R_0. There are two operating modes of a CHA: constant analyzer energy (CAE), also known as fixed analyzer transmission and constant retard ratio (CRR) also known as fixed retard ratio. In the CAE mode, electrons are accelerated or retarded based on a user defined pass energy. In CRR the electrons get retarded to a fraction of their original kinetic energy which is again specified by the user as they pass through the analyzer. This also makes it such that in the CRR mode the pass energy is proportional to the kinetic energy, and hence relative resolution is constant through the entire energy range. In the CAE mode it is the absolute resolution which remains constant all over the energy range which ensures accurate and reliable quantification of the XPS data while also accentuating the peaks

at the low kinetic energy end of the spectrum.

Detectors

After analyzing and transmitting the emitted photoelectrons, the detectors count the number of electrons to give the photoemission peak. Electron multipliers are used to increase the count and give a reasonably intense peak. Even though there are various types of multipliers, only two of them are commonly used: channel electron multipliers, also known as CEMs or channeltrons and channel plates. A CEM is an electron detector with an ability to multiply each electron by up to 108 times, providing a pulse output suitable for further amplification by normal electronic circuits. It is in the shape of a bent tube coated with a photoelectric material having a high secondary electron coefficient. The tube is usually kept at a potential of ≈ 2.5 kV. When an electron arrives at the mouth of the tube, secondaries are produced which are accelerated within the channeltron. One photon can produce a final output of 10 million electrons. The process of multiplication continues through the length of the CEM while creating even more secondaries along the way. This amplified cascade reaches the preamplifier where it is detected and the resultant pulse is finally registered by the acquisition software after being shaped into its final form. Similarly, pulses of electrons are produced in the channels of a microchannel plate. In combination with a position sensitive anode, it allows the detection of electrons with a resolution of upto tens of micrometers. Channel plates consist of discs which have arrays of small holes. Each hole behaves like a small channeltron. Since each channel has a smaller gain compared to a channeltron, it is common to use two plates in tandem. Such channel plates are used when data needs to be acquired in two dimensions; spectrometers have been designed using the channel plates to measure signals while performing parallel acquisition of photoelectron images, XPS line scans and parallelly acquiring angle resolved electrons.

Charge compensation

XPS is used to analyze samples with electrical properties varying from highly conducting to insulating such as wood or plastic. Insulating samples cause charging in the positive direction upon photoemission which causes a shift in the binding energy peak

in the higher energy direction consequently leading to ambiguity in peak assignment. If a non-monochromatic X-ray source is used for photoemission, there are a sufficient number of low energy electrons in the vicinity of the sample which can neutralize the sample surface. Monochromatic sources do not produce sufficient low energy electrons which can have the same effect which makes it difficult to analyze samples such as polymers, which are completely insulating. Flooding the sample surface with low energy electrons is the most common way to compensate surface charges. There is an additional gun called as a flood gun, which produces a uniform negative charge of known magnitude on the sample surface. This reduces the chance of non uniform or differential charging at the surface. Therefore, in order to have a good source of charge compensation, the electron gun must emit a beam of low energy to minimize any damage to the surface while also providing high flux to completely cover the whole surface. Presently, flood guns are available that can emit electrons of energies as low as 1 eV.

Chemical information from XPS

As mentioned earlier, another name for XPS is ESCA, since its major use is in the field of chemical analysis. First and foremost information obtained from characterizing the sample surface is the identification of the elements present. In order to get this data, it is usual to employ a scan over the whole energy region which can provide peaks for all the elements in the periodic table. This is called a survey or a wide scan and is the first scan taken in a typical XPS measurement. To assist with the identification of the peaks, a database is generally provided in the software or as a separate handbook. There are two kinds of peaks in an XPS scan: core level and Auger peaks. Auger peaks arise out of the Auger process: when an atom is probed by an external force, such as a photon or beam of electrons with sufficient energy to remove a tightly bound electron, an electron can be removed from the core shell. This emission leaves behind a hole in the core shell which is an unstable state. An outer shell electron can lose the energy equal to the difference between the binding energy of the displaced electron and its own binding energy to fill this gap. The transition energy can then be coupled to another outer shell electron which will be expelled from the atom if the energy provided to it is greater than its binding energy. In a spectrum, Auger peaks can be identified by changing the source energy and

finding the peak whose position does not change, since the binding energy of an Auger electron is independent of the source energy:

$$E_{kin} = E_{core} - E_b - E_c \tag{3.15}$$

where $E_{core}, E_b and E_c$ represent the binding energies of the core level, the first outer shell and the second outer shell. The Auger peaks are labeled according to the three levels taking part in the transition; the core level, the first and the second outer shell in that order. For example, O KLL peak denotes that the core level from which the initial electron is emitted upon being excited by the external source belongs to the K shell. The first L shows that the electron losing its energy to fill the hole created by the emission of the K shell electron belongs to the L orbital. The second L is for the secondary electron which gains energy equal to K-L and is emitted as an Auger electron. The two L may have different energies (as 2s and 2p) or the same, which are stronger and have more probability to occur than higher order transitions.

Elemental analysis in the XPS spectrum is carried out by identifying both the core level as well as the Auger peaks, which also gives information about the stoichiometry of the surface. Quantitative information can also be obtained by measuring the relative area under the photoelectron peaks. However, XPS spectra consist of significant background emission which must be substracted before any quantification. The background stems from the ability of X-rays to penetrate deeper into the sample, surpassing the surface layers. Electrons emitted at these levels may undergo inelastic collisions which alter the energy of electrons recorded by the detector. These energy loss processes result in a background of emission from energies separate from the characteristic photoelectric energy lines, while its shape is determined by the probability distribution for electrons with a given kinetic energy being modified from their original values. In case this probability distribution also exhibits a resonance type feature, convolution of a photoelectric peak consisting of this bias in the energy loss distribution can give rise to peak like structures which can be considered as part of the background. This means that while analyzing the XPS spectrum, there may be peaks which are extrinsic in nature rather than the intrinsic photoelectric mechanism. The background subtraction is carried

out commonly by three methods: linear, Shirley and Tougaard of which Shirley is the most commonly used technique. Next, quantification of the peak intensity is carried out using the peak areas. Factors affecting peak intensity can be described in the following equation:

$$I_{i,c} = f N_i \sigma_{i,c} \lambda \cos \alpha\, FTDA \tag{3.16}$$

where $I_{i,c}$ is the photoelectron intensity for core level c of element i, f is X-ray flux in photons per unit area per unit time, N_i is the number of atoms of element i per unit volume, $\sigma_{i,c}$ is the photoelectric cross section for core level c of the element i, λ is the inelastic mean free path (IMFP, defined as the distance travelled by an electron through a solid before losing energy) of the photoelectron in the sample, and α is the angle between the direction of the photoelectron and the sample normal. F is the solid angle of acceptance and T the transmission function of the analyzer. D is the efficiency of the detector and A is the area of the sample under observation. Since this equation is too complex for day to day analyses, empirical sensitivity factors (S) have been introduced whose values are specific for each element. Peak intensity is now defined in a much simpler equation, I = N × S, resulting in a semi-quantitative information in terms of relative atomic percentage:

$$Atomic\ \% = \frac{\frac{I_i}{S_i}}{\sigma \frac{I_j}{S_j}} \times 100\% \tag{3.17}$$

As the photoelectrons get attenuated by their passage through the sample, the information obtained comes primarily from the surface with a sampling depth of ≈ 7-10 nm. Consider photoelectrons being created at a depth z below the sample surface and being emitted in a straight line trajectory. Inelastic scattering leads to attenuation which is assumed to follow the Beer-Lambert law similar to light attenuation in an absorbing medium. Thus,

$$I_z = I_o \exp\left(-\frac{z}{\lambda \sin \theta}\right) \tag{3.18}$$

where I_z is the intensity of the photoelectrons from a depth z, I_o is from the electrons emitted from the surface and θ is the take-off angle to the surface ($\theta = 90 - \alpha$). λ is the IMFP of the electron with the escape depth being defined as $\lambda \sin \theta$.

Chemical shift and its significance

An important use of XPS in chemical analysis is to derive information about the oxidation state and thereby nature of bonding at the sample surface. The core level BE values deviate with bonding and environment producing what is called the chemical shift. In such cases, the binding energy is determined by taking into account the difference between the total energies of the initial state energy of the atom and the final state energy of the ion created due to photoemission. These changes can be calculated by quantum chemical methods and arise due to redistribution of electrons depending on the individual values of electronegativity for each atom involved in the process. However, the range of these shifts is only of the order of a few electron volts, which makes it critical to have good energy resolution and a narrow peak width in order to accurately estimate their value. In case of samples where the same atom may be in different chemical environments, such as polymers with carbon, the resulting C 1s peak will have various shifted peaks overlapping to produce a complex envelope. Extracting structural information from such a spectrum requires resolution of the component peaks and a knowledge of the inherent lineshapes. The approach to do this is the curve fitting technique which carries with itself its own mathematical formulation which will not be discussed here. Curve fitting is carried out after subtracting the background and a set of components is introduced within the envelope at appropriate BE positions in such a way that the envelope is completely covered. Usual peak fitting softwares calculate the sum of the components and compare with the experimental data, thereby obtaining a measure of how appropriate the fitting is by the least squares method. There are a lot of parameters which must be given as input, such as the peak lineshape and FWHM, its position and intensity. No unique solution can be provided to any fitting because of these limitations, and hence the only option is to perform such a fit which looks reasonable from a spectroscopic as well as a chemical point of view.

3.1.3   Optical characterization

This section describes the optical characterization methods used in this work. Raman and SERS measurements are carried out along with photoluminescence (PL) as optical probes. Raman studies have been performed using a 530 nm Nd:YAG laser while PL from the samples has been obtained both by a Xe lamp as well as a He:Cd laser emitting at a wavelength of 325 nm.

Raman spectroscopy

Raman spectroscopy is based on the inelastic scattering of monochromatic light which is usually from a laser source. Interaction of light with the sample and the consequent inelastic scattering changes the frequency of the light, which is called the Raman effect. The frequency or energy shift arises due to the interaction between incident electromagnetic waves and the vibrational energy levels in the atoms of the sample. Plotting the intensity of the scattered light versus frequency is what is called as a Raman spectrum of the sample. Generally, Raman spectra are plotted with respect to the laser frequency such that the Rayleigh band (elastically scattered light) lies at 0 cm^{-1}. Using this scale, the band positions lie at frequencies that correspond to the energy levels of different functional group vibrations. The Raman spectrum can then be interpreted in a similar way as the infrared absorption spectrum.

Theory of Raman effect

The Raman effect is based on the molecular deformations that take place when an electric field $\mathbf{E}$ is applied, where the molecular polarizability of the sample is α. A molecule will be Raman inactive, i.e. will have no peaks in the Raman spectra if there is no change in polarizability and $(\frac{d\alpha}{dq})_e \neq 0$ where q is the normal coordinate and e the equilibrium position. The prediction whether a particular molecular vibration is Raman active or not is determined by what are called the **selection rules**, the primary one of which has already been mentioned above. The incident laser beam can be considered as an oscillating electromagnetic wave with a vector $\mathbf{E}$ that induces an electric dipole $\mathbf{P} = \alpha\mathbf{E}$ when incident on the sample which deforms the molecules. Due to periodic

deformations, the molecules start vibrating with a frequency ν_m. The amplitude of this vibration is called a nuclear displacement. Another way to look at it is that the incident electromagnetic wave with frequency ν_0 excites and converts the molecules into oscillating dipoles. There are three different frequencies which can be emitted by these dipoles:

1. A molecule which does not have Raman active modes absorbs a photon with frequency ν_0 and is excited to a higher energy state. The molecule then loses the same amount of energy reverting back to its original state and emits light with the same frequency ν_0 as the excitation source. Such type of interaction is called **Rayleigh scattering**.

2. A Raman active molecule, when absorbing a photon with frequency ν_0 is initially in its basic vibrational state. A part of this incident frequency, ν_m is used to excite the Raman active mode and the resulting frequency of the scattered light is reduced to $\nu_0 - \nu_m$ which leads to a downward shift in the frequency of the peak in the Raman spectrum. Such kind of interaction is called a **Stokes shift**.

3. If the molecule is in an excited vibrational state when it absorbs a photon with frequency ν_0, it can release excessive energy in the form of a wave with frequency ν_m in order to return to its basic vibrational state. Then, the frequency of the Raman active mode peak in the spectrum shifts upward by $\nu_0 + \nu_m$. This Raman frequency is called **Anti Stokes shift**.

The origin of Stokes and Anti-Stokes shifts can be explained in terms of the types of oscillations involved. The polarisability (α) of the molecule is effected by the bond length, shorter bonds are harder to polarise. If the polarisability is changing then it will oscillate with the same frequency as the molecule is vibrating (ν_{vib}).

Polarisability of the molecule:

$$\alpha = \alpha_0 + \alpha_1 \sin(2\pi\nu_{vib}t) \tag{3.19}$$

The external oscillating electric field from the photon which has a frequency ν_p:

$$E = E_0 \sin(2\pi\nu_p t) \tag{3.20}$$

Therefore the induced dipole moment is:

$$p_{ind} = \alpha E = (\alpha_0 + \alpha_1 \sin(2\pi\nu_{vib}t)) \times E_0 \sin(2\pi\nu_p t) \tag{3.21}$$

since $\sin A \times \sin B = \frac{\cos(A-B) - \cos(A+B)}{2}$

the equation can be written as

$$p_{ind} = \alpha_0 E_0 \sin(2\pi\nu_p t) + \frac{\alpha_0 E_0}{2} \cos(2\pi(\nu_p - \nu_{vib})t) - \frac{\alpha_0 E_0}{2} \cos(2\pi(\nu_p + \nu_{vib})t) \tag{3.22}$$

This equation shows that photons may be scattered with a frequency ν_p (Rayleigh scattering), $\nu_p - \nu vib$ (Stokes scattering) and $\nu_p + \nu vib$ (Anti-Stokes scattering).

With complex molecules and interactions between neighbours additional parameters need to be considered and the symmetry of the molecules becomes an important incorporation. The derivation presented here is for single molecules in a gas. For crystalline materials such as GaN, the vibrations are quantified as phonons and the modes are determined by the crystal structure.

Raman scattering in GaN

Raman spectroscopy is a standard characterization technique used to study various properties of crystalline solids such as lattice parameter, stress, electronic and magnetic properties etc. It has many advantages compared to other spectroscopic techniques: it is non-destructive, requires no special sample preparation and is contactless so the sample is not physically modified in any way. Using a standard Raman microscope with a visible light laser as illumination source can give a lateral resolution of upto $\approx 1\mu$m or less depending on the spot size of the beam incident on the sample. In solids, Raman scattering occurs when the electronic polarizability is induced by excitations such

as phonons and plasmons. When Raman scattering occurs due to phonons, scattering efficiency is higher in covalent crystals compared to ionic crystals because the valence electrons are less localized and a larger fluctuation of the polarizability can be induced by lattice vibrations. This makes nitride semiconductors very suitable candidates for Raman scattering as the bonding in their case is a mixture of covalent and ionic. Also, they are quite robust and can withstand extreme conditions, hence laser irradiation does not harm the samples much.

Group III nitrides crystallize in either hexagonal (wurtzite, space group C_{6v}^4) or cubic (zinc blende, T_d^2) structure. In both the cases the Ga atom is tetrahedrally surrounded by four nitrogen atoms and the only difference is in the stacking sequence. While it is ABCABC.... for the cubic phase it is ABAB... for the hexagonal phase. The unit cell length of the cubic phase in (111) direction is given by the width of one bilayer while it is twice as much for the hexagonal phase in the (0001) direction. Since the crystal vibrations in solids are defined mainly by phonons, a dispersion relation is often defined for the phonons which is a plot of the angular frequency of the phonon ω as a function of its momentum k. The slope of this plot gives the group velocity of vibration of the atoms, which is also the speed of sound in the crystal. Since a crystals are periodic structures, the behavior of phonons within a crystal is only modeled within a single Brillouin zone. Each Brillouin zone represents one unit cell in reciprocal space. If the Brillouin zone contains more than one atom, then there are two different modes of phonons: acoustic and optical. The acoustic mode corresponds to sound waves traveling through the crystal, while the optical mode may interact either directly or indirectly with light. At the edge of a Brillouin zone, the group velocity of the phonon approaches zero, thus creating a standing wave.

Energies of the optical phonon modes in Γ are very similar in both the cubic as well as wurtzite phase. The first order Raman scattering is caused by phonons with wavevector $k \sim 0$ (Γ point) due to a momentum conservation rule in the light scattering process. At the Γ point, group theory predicts eight sets of phonon normal modes for the hexagonal structure, $2A_1 + 2E_1 + 2B_1 + 2E_2$. Of these, one A_1 and E_1 are acoustic while the rest are optical. For the wurtzite phase, the optical phonon modes are shown as a schematic in Figure 3.11.
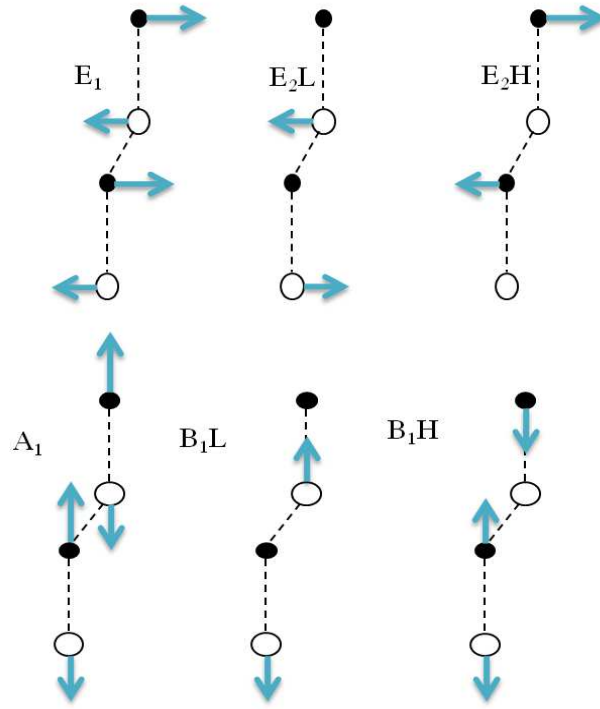
Figure 3.11: Optical phonon modes in a wurtzite structure.

The atomic displacement scheme of the optical modes is shown in Figure 3.11. A_1 and B_1 modes give atomic displacements along c-axis while E_1 and E_2 give them perpendicular to c-axis. The A_1 and E_1 modes are both Raman and IR active, while the two E_2 modes are only Raman active. Both the B_1 modes are neither Raman nor IR active and are known as silent modes[135]. The Raman scattering efficiency S with polarization detection is given by

$$S\alpha|e_L\mathbf{R}e_S|^2 \tag{3.23}$$

where e_L and e_S denote the polarization for the incident and scattered light, respectively, and $\mathbf{R}$ is the Raman tensor of the scattering process. For wurtzite structure, $\mathbf{R}$ has only diagonal non zero components for the A_1 phonon mode, only off-diagonal for the E_1 mode and both diagonal and off-diagonal for the E_2 mode[136]. This information is useful when the polarization directions are taken into account, for different configurations certain modes are visible. Table 1 gives the scattering geometries for observing the Raman active modes in the wurtzite structure.

Configuration	Mode
x $(y, y)\overline{x}$	$A_1(TO)$, E_2
x $(z, z)\overline{x}$	$A_1(TO)$
x $(z, y)\overline{x}$	$E_1(TO)$
x $(y, z)y$	$E_1(TO)$, $E_1(LO)$
x $(y, y)z$	E_2
z $(y, x)\overline{z}$	E_2
z $(y, y)\overline{z}$	$A_1(LO)$, E_2

Table 3.1: Raman configurations of allowed modes in wurtzite structure

The notation used to describe the configuration in Table 3.1 is conventional: the symbols outside the bracket show the direction of incident and scattered light from left to right, respectively. Inside the bracket, the polarization direction for both the light rays is given in the same sequence. For example, the $A_1(LO)$ phonon mode exhibits atomic displacement parallel to c-axis and propagates in the same direction. Considering z-direction to be the one along c-axis, the $A_1(LO)$ mode can be observed from the c-plane of a wurtzite structure in the $z(y,y)\overline{z}$ scattering configuration.

Raman studies are also an excellent way to probe stresses in the film. Wurtzite structures heteroepitaxially grown on hexagonal (0001) or cubic (111) surfaces will have uniform biaxial strain in the c-plane with strain tensor components $\varepsilon_{xy} = \varepsilon_{yz} = \varepsilon_{xz} = 0, \varepsilon_{xx} = \varepsilon_{yy} \neq 0, and \varepsilon_{zz} \neq 0$. This means that the layers are uniformly compressed or expanded in the c-plane, and in a reverse manner along the c-axis, maintaining the C_{6v} symmetry. The selection of phonon modes does not change in such a situation and only a frequency shift is observed, if any. Biaxial strain in the c-plane of wurtzite GaN is commonly probed by observing frequency shifts in the E_2 (high) or E_2H mode[137,138], as the frequency is sensitive to biaxial strain in the c-plane and this mode also gives the strongest signal in the spectrum which is quite convenient.

Surface Enhanced Raman spectroscopy

Surface Enhanced Raman spectroscopy (SERS) is a modification of the usual Raman spectroscopy in a way that the substrates used in such experiments allow electromagnetic field enhancement of the surface plasmons supported usually by metal nanoparticles. The enhancement of the field results in the increase in Raman signal obtained from the sample which allows detection of ultra-low concentration analytes. SERS has evolved to an extent

whereby single molecules are routinely observed due to the large enhancement[139].

The most important aspect of SERS is the enhancement of the Raman signal, and after much debate it is agreed that the dominant contributor to this is the electromagnetic enhancement mechanism. The basic concept behind it is an amplification of light by the excitation of localized surface plasmon resonances (LSPR). Maximum enhancement requires a concentration of light which occurs in gaps, crevices or sharp features of plasmonic materials which are the noble and coinage metals (gold, silver and copper) with nanoscale features. The SERS enhancement factor can theoretically go upto 10^{10}-10^{11}[140].

Another mechanism involved in signal enhancement is chemical enhancement which primarily involves charge transfer processes. The excitation wavelength is resonant with the metal-molecule charge transfer electronic states[141]. The total SERS enhancement factor is a combination of both the electromagnetic and the chemical mechanims. Resonance Raman effects also play a key role in SERS experiments as molecules with very large resonance Raman cross sections are used in SERS.

There are a few considerations to be taken into account when performing a SERS measurement in order to obtain maximum signal generation and enhancement. First is the choice of enhancing substrate, which range from nanorods to colloidal solutions and have tunable plasmon resonances along with a range of enhancement factors. Also, since the SERS enhancement dies off exponentially with distance (r^{-10} for a spherical surface[142]), maximum enhancement is found closest to the surface. The second parameter is the excitation source which should enable best possible excitation of the plasmon resonance. It is generally accepted that the enhancement would be maximum if the laser source has a frequency same as that of plasmon resonance for a substrate having a single peak in its LSPR spectrum. Although experimentally this has been found to lead to high values of enhancement factors, the maximum enhancement is actually found when the laser is blue shifted with respect to the plasmon frequency, ideally by half of the Raman vibrational frequency value[143]. This enhances both the excitation as well as the emission part of the Raman process, giving rise to highest Raman signals.

Detection of the SERS signal is identical to normal Raman experiments. A notch or

long-pass filter is used to absorb or reflect any Rayleigh scattering while simultaneously transmitting Raman signal. A spectrograph and detector are used to image Raman spectra across a wide spectral region.

Photoluminescence

Photoluminescence (PL) spectroscopy is a non destructive method to probe the electronic structure of materials. The basic principle of PL is the phenomenon of an electron absorbing a specific quantum of energy from an external light source (photons) to get excited to a higher energy level and then releasing the absorbed energy in the form of light to revert to its stable ground state. This light is detected and its energy recorded which then gives information about the electronic structure of the material.

There are two types of PL processes, fluorescence and phosphorescence. Consider a pair of electrons occupying the same ground state; both would have opposite spins in order to have lowest energy configuration and be in what is called the singlet spin state. Upon absorbing energy from an external source, one electron would move from its valence state to an excited state. If the spin of this electron is conserved, i.e. does not change, it is said to be in a singlet excited state. Emission of a photon to revert back to the singlet ground state, or between any two energy levels with spin conservation is called fluorescence. The probability of this phenomenon is very high and hence the average lifetime of an electron in the excited state is only $10^{-5} - 10^{-6}$s. Therefore, fluorescence also decays rapidly once the excitation source is removed. The three possible configurations are depicted in Figure 3.12.
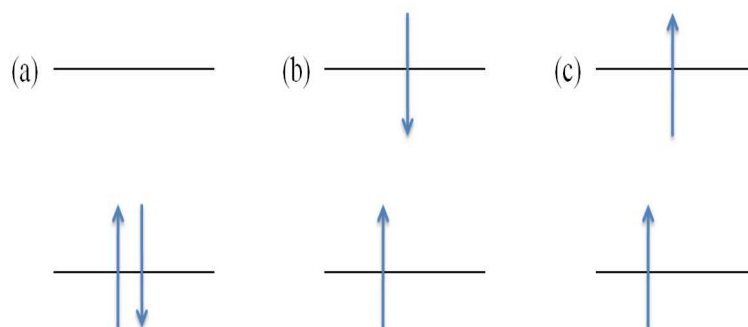
Figure 3.12: Spin configuration for a two electron system existing in (a) singlet ground state, (b) singlet excited state, and (c) triplet excited state

In case the excited electron changes its spin upon absorption of incident light and subsequent transfer to an elevated energy state, it is said to be in a triplet excited state and the spins of both the electrons are no longer paired. The emission that takes place when an electron in a triplet excited state goes back to its ground state, or between any two energy levels differing in electronic spins is called phosphorescence. As the average lifetime of phosphorescence ranges between $10^{-4} - 10^{4}$s, it can be observed for some time even after the removal of the excitation source.

Radiative transition

Although PL is observed only when the electron emits light while returning to the ground state, there are other pathways which can be taken. These competing processes are radiative transfer to another ion and nonradiative transfers such as multiphoton relaxation and cross-relaxation between different or similar ions. The external quantum efficiency of PL is defined as the number of photons emitted divided by the number of photons absorbed, and in majority of the cases can be expressed as the ratio between the measured lifetime to the radiative lifetime of a given level. The process of excitation starts with an electron absorbing the incident energy to elevate itself to a high vibrational level in the excited state. It then relaxes nonradiatively to the lowest vibrational level in the excited state by releasing excess energy to its surroundings. From the lowest energy level of the excited state, the electron then returns to its ground state by emitting a photon. This energy is what is expressed as the energy gap or the band gap in semiconductors and is the strongest emission in a lattice. Sometimes, when there are lattice impurities, defect bands may exist within this band gap which would lead to extra peaks being present in the spectrum.

Nonradiative transition

As mentioned earlier, the energy absorbed by the electron is sometimes released into the lattice and not as radiation during the relaxation process. Since these processes compete with radiation and consequently reduce the quantum efficiency of the material, it is imperative to suppress these phenomena. An example of such a process is the vibrational relaxation which occurs after the electron reaches the excited state and

occupies a high vibrational energy level. The relaxation takes place very quickly with the average lifetime of an electron being only 10^{-12}s. Another form of nonradiative transition is an internal conversion wherein an electron present in the lowest vibrational level of an excited state loses energy to descend into a higher vibrational level of a lower electronic energy state with the same spin. A combination of vibrational relaxation and internal conversion allows an electron to travel from an excited state to its ground state without the emission of a photon. A related form of such an occurrence is external conversion in which the excess energy is transferred to the solvent or another part of the sample's environment. The radiative and non radiative processes are schematically shown in Figure 3.13.
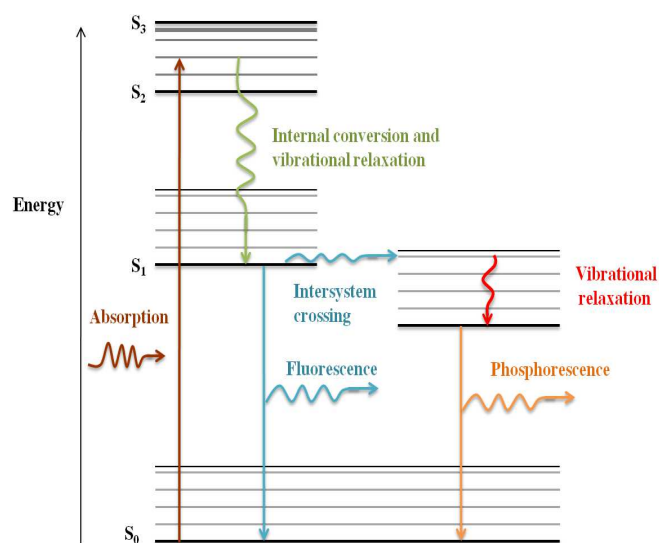
Figure 3.13: Energy level diagram of a molecule showing the pathways available for an electron for relaxation. Both radiative as well as nonradiative pathways are explained.

The last form of nonradiative transition is the intersystem crossing where an electron in the ground vibrational level of an excited electronic state switches to a high vibrational level of a ground electronic state with an opposite spin.

In semiconductors, the band gap can be either direct or indirect which leads to an interesting discussion on how the PL process differs in both the cases. The energy vs wavevector diagram for both systems is drawn in Figure 3.13 which shows how PL occurs in each case. Direct and indirect gap materials are distinguished by the relative positions of their conduction band minimum (CBM) and valence band maximum (VBM) in the Brillouin zone. For a direct gap material, both CBM and VBM are at the zone center

with k = 0. Indirect gap materials, on the other hand, have their CBM at some other point where k ≠ 0.

During the photon absorption and susbequent excitement of an electron to a higher energy state, both energy as well as momentum must be conserved. An incident light with energy $\hbar\omega > E_g$ would generate an electron hole pair and the electron (or hole) is excited to the conduction (or valence) band. For a direct gap material, the wavevector for both CBM as well as VBM possesses the same value, i.e. $\hbar\overrightarrow{k_i} = \hbar\overrightarrow{k_f}$, where $\overrightarrow{k_i}$ and $\overrightarrow{k_f}$ are the wavevectors of the initial and the final electronic state, respectively.
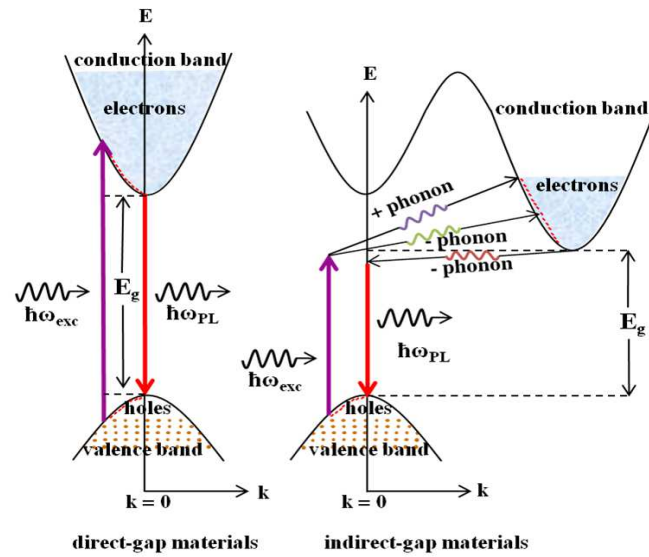
Figure 3.14: Schematic of band diagrams for a direct and an indirect band semiconductor. Photon absorption and emission processes are shown by vertical arrows on the E vs k diagrams. In indirect gap materials (right), CBM and VBM have separate k values. Therefore, in order to conserve momentum, photon absorption processes must involve either absorption (indicated by a "+" sign) or emission (indicated by a "−" sign) of a phonon.

This guarantees conservation of momentum for photon induced excitation of an electron since $\hbar\overrightarrow{k_i} + \hbar\overrightarrow{k_{phot.}} \approx \hbar\overrightarrow{k_i} = \hbar\overrightarrow{k_f}$ because $\overrightarrow{k_{phot.}}$, the wavevector of the absorbed photon $(2\frac{\pi}{\lambda} \sim 10^5 cm^{-1})$ is negligible compared to the electron wavevector which is of the size of the Brillouin zone $\frac{\pi}{a} \sim 10^8 cm^{-1}$, where a is the unit cell dimension having values of a few angstroms. This implies that during a photon absorption process in a direct band gap semiconductor, the electron wavevector does not change significantly.

An indirect gap material, on the other hand, has different wavevectors for CBM and VBM. Thus, to conserve momentum, the photon absorption process must be assisted by

either absorbing or emitting a phonon since the electron wavevector must change its value significantly to move from the valence band where its state is $(E_i, \overrightarrow{\mathbf{k}_i})$ to a state $(E_f, \overrightarrow{\mathbf{k}_f})$ in the conduction band. The absorption of a photon itself is not sufficient to provide this energy since $| \overrightarrow{\mathbf{k}_{phot.}} | << | \overrightarrow{\mathbf{k}_i} - \overrightarrow{\mathbf{k}_f} |$.

Since the PL efficiency is calculated as number of photon emitted compared to those absorbed, it can also be described in terms of competition between radiative and nonradiative recombinations. In an indirect gap material, the PL requires a change in both energy and momentum for the excited electron and hence requires both a photon as well as a phonon. This means that it is a second order process with a long radiative lifetime ($\sim 10^{-5} - 10^{-3}$s), and therefore the efficiency is relatively lower due to the competition with nonradiative recombination. In contrast, the emission of a PL photon does not require any phonon assistance for direct gap materials and hence has a much shorter lifetime ($\sim 10^{-9} - 10^{-8}$s) which makes it have a much higher PL efficiency compared to the indirect gap material.

3.1.4   Electrical Characterization

In this section, a short description of the methods employed to electrically characterize the samples would be provided. Four probe method, magnetoresistance and photoconductivity experiments were performed on various samples to determine the transport properties of the structure. A basic setup of the experiment and the principle would be explained in this section.

Four probe method

The four probe method is essentially a setup to measure the resistivity of a material by means of employing four equally spaced metal (usually tungsten) tips with same radii. Before describing the setup further, a brief introduction of the method of measuring resistance is required to understand the importance of this particular method.

Ohm's law

If physical conditions such as temperature and pressure are constant, then potential difference across the two ends of a conductor is proportional to the current flowing through the conductor:

$$V \; \alpha \; I$$

$$\text{or, } V = IR$$

The constant of proportionality R is called the resistance of the conductor.

Resistivity

At a constant temperature, the resistance R of a conductor is (i) proportional to its length, and (ii) inversely proportional to its area of cross section,

$$R \; \alpha \; \frac{L}{A}, or R = \rho \frac{L}{A} \qquad (3.24)$$

where ρ, the constant of proportionality, is the resistivity of the material.

Unit of resistance is Ohm (Ω) and unit of resistivity is Ohm.meter (Ω.m). Ohm's law can also be expressed in terms of current density

$$\overrightarrow{E} = \rho \overrightarrow{J} \tag{3.25}$$

where $\overrightarrow{J}$ is the current density and $\overrightarrow{E}$ is the electric field set up within the conductor due to the resistance offered.

The corresponding scalar equation $E = \rho J$ is valid if the conductor is homogenous and isotropic, meaning that the conductivity is uniform throughout the material and carries a uniform electric current (J) per unit of cross sectional area, through a uniform electric field E, in one dimension.

Two probe method

Consider a long, thin, wire-like geometry of a uniform cross section which has a constant current flowing through it. The resistivity ρ of this sample can be ascertained by measuring the voltage drop across the sample. In Figure 3.15, a battery E provides the current I flowing in the sample from point 1 to point 2. The potential difference between the two contacts at the ends of the sample is V (volt). If l is the length of the sample between the two probes and A the area of cross section, then the resistivity of the sample is given as

$$\rho = \frac{V}{I} \frac{A}{l} \tag{3.26}$$

This is the two-point probe method which was the initial setup to measure resistivity. However, this method has several drawbacks, such as

(i) Error incorporated through the contact resistance of the measuring leads.

(ii) The setup works only for a particular geometry and cannot be used for samples with random shapes.

(iii) Soldering the test leads can be difficult and will be another source of error.
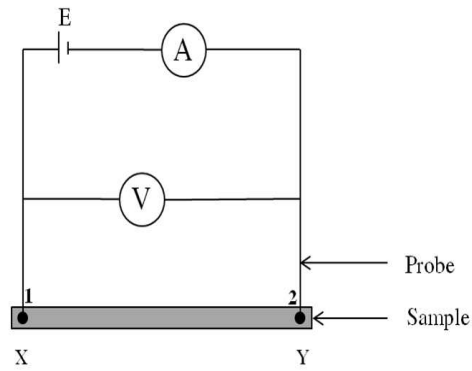
Figure 3.15: Schematic showing two probe method to determine resistance of a homogenous cylindrical sample

(iv) For semiconductors, heating of samples from soldering leads to injection of impurities in the material which affects the intrinsic electrical resistivity. Further, some metallic contacts form Schottky barriers on the semiconductor surfaces.

To overcome the first two issues, the four-point probe method was introduced. This method can be employed to calculate resistivity of materials with a wide variety of shapes, though with uniform cross sections. Soldering is replaced by pressure contacts to eliminate the last two drawbacks mentioned above.

Four probe method
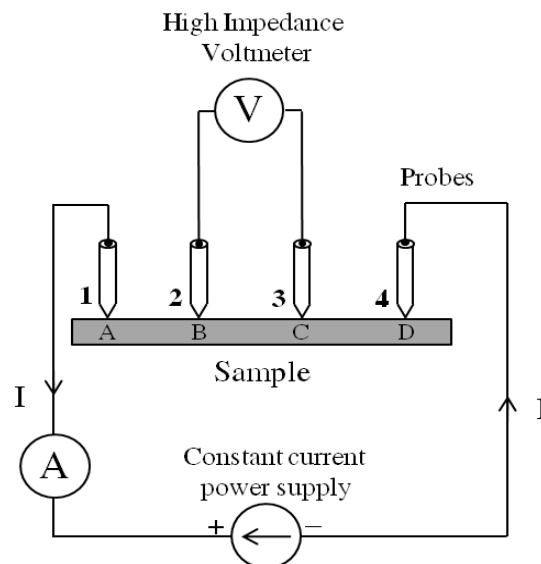
Figure 3.16: Schematic of four probe method to determine resistance of a homogenous cylindrical sample

In the four probe method shown in Figure 3.16, four equally spaced metal tips (usually

made of tungsten) with same cross sectional radii are placed on the sample. Each probe is supported by a spring on its end to minimize sample damage during the measurement. The four metal tips are a part of an automated stage that travels across the sample. A high impedance current source is used to supply current through the outer two probes and a voltmeter measures the voltage across the inner two probes to determine the resistivity.

The inner probes do not draw any current due to the high input impedance voltmeter in the circuit. This eliminates the unwanted voltage drop (equal to I$times$R) at points B and C caused by the contact resistance between probes. As these contact resistances are very sensitive to pressure and surface conditions such as oxidation, error in the two probe method (where a current is passed through the potential measuring contact) can be very large.

Magnetoresistance

As the name implies, magnetoresistance (MR) is the ability of a material to change its electrical resistance in response to an externally applied magnetic field. There are many phenomena which fall under the broad category of MR, some of which occur in bulk non magnetic metals and in semiconductors (e.g. giant magnetoresistance or GMR, Shubnikov de Haas oscillations etc.) or the more commonly occurring positive magnetoresistance in metals. The first such MR effect was observed by William Thomson (aka Lord Kelvin) in 1851, but he was not able to lower the resistance of materials by more than 5 %. Currently, many systems (e.g. semimetals, concentric ring EMR structures are known where magnetic field can change resistance by orders of magnitude.

MR occurs due to the difference in drift velocities of charge carriers. When the magnetic field is applied, the Hall voltage $V_H = E_y t = | \vec{v} \times \vec{H} |$ either compensates or cancels the Lorentz force for the carriers with the average velocity, $\vec{v}$. However, since all the charge carriers do not possess the same velocity, the ones moving at values less than $\vec{v}$ are over compensated and those higher than $\vec{v}$ are under compensated which results in trajectories that are not along the applied electric field ($\vec{E_x}$). The effective mean free path decreases as a consequence, increasing the resistance of the sample. As the applied magnetic field is increased, the trajectories of the charge carriers are more deviated which increases the MR behaviour.

The effects of the magnetic fields on the electronic properties of metals and semiconductors are oscillatory, and are often used to study the nature of electron transport in materials. The oscillation of magnetization of a crystal, commonly known as the de Haas-Van Alphen effect, are used to probe the Fermi surface of metals and semiconductors. Its analogue Shubnikov-de Haas effect describes the oscillations in longitudinal MR; it is observed in bulk materials and is typically much smaller.

Weak localization

The phenomenon of weak localization is observed in disordered systems and is essentially caused by the quantum interference of conduction electrons which manifests itself as a positive correction to the resistivity of the system. It is observed in one, two or three dimensions but from an experimental point of view the two dimensional case is most favoured. The correction to the resistance is of the order of 10^{-2} to 10^{-3} and can be measured within an error of 1%. MR is a powerful method to observe weak localization and to determine the lifetime of the electrons. Weak localization is particularly convenient to study in thin films as it corresponds to a time-of-flight (TOF) experiment with conduction electrons.

It is important to note that weak localization corresponds to an interference experiment involving conduction electrons which get scattered at impurities[144]. Applying magnetic fields influences this interference and introduces a time scale in the system.

At low temperatures, the conduction electrons possess two separate lifetimes, one elastic τ_0 and another inelastic τ_i. Here, τ_0 also represents the lifetime of the electron in an eigenstate of momentum while τ_i is the lifetime in an eigenstate of energy. At temperatures of 4K, τ_i can exceed τ_0 by several orders of magnitude which can enable the conduction electron in any state k to be scattered by impurities without losing its phase coherence. Since the impurities are described by a statistical distribution, the scattered wave in turn form chaotic patterns. Boltzmann theory neglects interference between the scattered partial waves and assumes that the momentum of the electrons disappears exponentially after a time τ_0. For free electrons this leads to the simple Drude formula for conductivity

$$\sigma = \frac{ne^2}{m}\tau_0 \tag{3.27}$$

Photoconductivity

Photoconductivity (PC) is a phenomenon wherein the electrical conductivity of a material increases upon absorbing electromagnetic radiation such as UV, IR or visible light, gamma radiation etc. It is frequently observed in small band gap semiconductors, where energy more than $\frac{E_g}{h}$ generates additional charge carriers. At high temperatures this effect is nullified to a large extent and only by illuminating using an intense beam of light PC may be observed.

Consider a thin slab of semiconductor illuminated by a beam of light propagating along the direction of its length (let it be in x-direction). The light with radiation intensity I (W/m^2) is shone at a position x from one end of the semiconductor. If α is the absorption coefficient per unit length, the power absorbed per unit length will be αI. The change in intensity with distance along the length of the sample is given by

$$\frac{dI}{dx} = -\alpha I \tag{3.28}$$

which can be solved as

$$I = I_0 \exp -\alpha x \tag{3.29}$$

Defining quantum efficiency η as the fraction of absorbed photons that produce excitons, i.e. electron-hole pairs, the number of such pairs produced per unit time is given by

$$\Delta n = \Delta p = \frac{\eta \alpha I}{h\nu} \tag{3.30}$$

Although constant illumination should, in principle, provide an increasing number of charge carriers which means that the current should increase linearly with time, it does

not occur as the excitons have a short and finite life time (10^{-7} *to* 10^{-2}s). This results in a recombination of the pairs ensuring that the number of excess charge carriers saturates instead of increasing indefinitely.

For an n-type semiconductor, if the lifetime of the minority charge carriers is τ_p, the rate of change of carrier concentration is given by

$$\frac{d}{dt}(\Delta p) = \frac{\eta \alpha I}{h\nu} - \frac{\Delta p}{\tau_p} \tag{3.31}$$

under steady state condition of $\frac{d\delta p}{dt} = 0$,

$$\delta p = \frac{\eta \alpha I_p \tau_p}{h\nu} = \Delta n \tag{3.32}$$

the excess hole density leads to an additional conductivity

$$\Delta \sigma = q\delta n \mu_e + q\Delta p \mu_h \tag{3.33}$$

Persistant Photoconductivity

The Persistant Photoconductivity (PPC) effect is a light-induced enhancement in conductivity that persists for a long period even after the removal of illumination source. The recombination of charge carriers, apart from preventing the PC to increase indefinitely, also acts as the main quenching mechanism. After the light is turned off, the recombination can be prevented by local potential barriers around the donor levels. This results in a persistent carrier concentration, which can be used to obtain PPC under an applied voltage bias.

PPC is often inherent to wurtzite GaN layers[145] and its origin has been attributed to an enormous number of factors ranging from bistable defects[145,146], deep level donors like AX[147] or DX[147,148], random potential fluctuations due to non stoichiometry and heterointerfaces[149,150] to unintentionally incorporated cubic phase crystallites in the hexagonal matrix[151]. In spite of various efforts in investigating optical metastability in GaN, the explanation of this phenomenon still carries contradictions. A possible correlation between PPC and yellow luminescence (YL) was also suggested[145,152,153] but there were reports which did not see any such correlation[149,150,154]. Recently, a study involving a comparison of PC and contact potential difference (CPD) data recorded in both steady state as well as transient mode has shown that localized defect states may be enabling charge hopping which causes a back transfer of conduction electrons to surface states after termination of illumination.

The PPC effect in conjunction with PC studies can elucidate the defect states in a material and has been so used to characterize many materials. Although considered detrimental to devices, it nevertheless provides an extremely useful tool to understand optical defect features in a system.

Chapter 4

Time dependent growth and properties of GaN nanowall network

4.1 Introduction:

In the past few years, there has been an increasing interest in porous GaN materials[122,155,156] which has also led to applications in sensing[157–159] and junction diodes[160]. It has also been realized that fabricating porous structures using a bottom up technique is much more cleaner, efficient and provides better kinetic control over feature sizes than conventional methods of etching which have been used until now to induce porosity. Initial studies by Kesaria *et al.* in the study of GaN nanostructures suggested that the diffusion of Ga adatoms over the substrate surface is hindered at steps of edge dislocations[118] which is an energetically favorable position for nucleation to take place. It was also theorized by them that lattice mismatch could be a factor in determining the morphology and open screw dislocations could be present at the void regions between the nanowalls. One of the major advantages of these nanostructures is their ability to effectively filter out interfacial dislocations due to the presence of free surfaces[26,161]. In contrast to flat epitaxial layers, nanostructures can be free from any residual strain, though completely stress-free structures have not yet been achieved[162,163]. Additionally, a high surface to volume ratio enables large exposure to external factors and leads to an improvement in luminescence characteristics[164]. Therefore, it is significant

to explore the strain state of the nanowalls in comparison to other nanostructures and flat films. Recently, X-ray Photoelectron Spectroscopy (XPS) has been extensively used to probe the stoichiometry and electronic structure of GaN thin films[165–167]. XPS is also being applied to study the impact of nanostructuring on the electronic structure and bonding[168–170]. Performing valence band XPS measurements on samples with different morphologies and electronic structure is essential to understand bonding manifestations in these low dimensional systems.

This chapter has been divided into three parts based on the experimental work carried out: the first set of experiments is designed to better understand the initial growth mechanism of GaN nanowalls which would eventually help in tailoring the porous GaN structures according to ones requirements by studying the time dependent growth of GaN films. The next experimental set involved the comparison of stress and strain states in the nanowall by comparing the structural and optical properties between nanowalls and other nanostructures grown by MBE. A commercially obtained flat GaN epilayer was used as a reference. In the third part of the study, XPS valence band studies of two nanowalls with differing morphologies was carried out and a comparison with a flat epilayer was made in order to study the effect of nanostructuring on the electronic structure and bonding configuration. The films were characterized using field emission scanning scanning electron microscope (FESEM), photoluminescence (PL), high resolution x-ray diffraction (HRXRD) and x-ray photoelectron spectroscopy (XPS).

4.2   Experimental Details:

The first set of experiments involved the time dependent growth carried out by growing four GaN nanowall network films for different time durations on bare c-sapphire substrates using a PA-MBE system for which the experimental details are as follows: the substrate and the Ga k-cell temperature in all the cases were kept at 640 °C and 1075 °C, respectively. The N_2 flow rate was 4.5 sccm to enable a nitrogen rich condition with III:V ratio of 1:100. The forward plasma power was maintained at 375 W with minimum reflected power yielding a growth rate of $\approx$ 300 nm/h. The four samples were grown for 20, 40, 60 and 80 minutes respectively. Hereby, the samples are referred to as S1 (20

min.), S2 (40 min.), S3 (60 min.) and S4 (80 min.).

The second set of experiments were performed for comparing the strain and luminescence properties of the nanowalls with other structures, the experimental details for which are: three GaN films were grown on bare c-sapphire at substrate temperatures of namely 630°C, 680°C and 730°C for 2 hours each.

To probe the electronic structure using XPS, two GaN films were used which were again grown on bare c-plane sapphire substrates at 630°C and 680°C for 2 hours each. A 2 μm thick MOCVD-grown commercial GaN epilayer grown on c-sapphire (TDI) was used as a reference sample. The pre-growth procedures in all experiments were followed as explained in the chapter with experimental details.

Films were characterized *in-situ* using RHEED with the energy of the electron beam being 8 kV. The morphology was determined *ex-situ* using FESEM (FEI, Netherlands). Optical properties of all the samples were examined by Photoluminescence (PL, Horiba Jobin Yvon) using a Xe lamp source which was made to emit at 325 nm using a filter. The crystalline properties were probed using an HRXRD instrument (Discover D8, Bruker) operating in a triple axis mode and using a four bounce Ge (220) monochromator, employing a Cu K$_\alpha$ source emitting at 1.5406 $\mathring{A}$. For absorption measurements, an LS 55 spectrometer (Horiba, Jobin Yvon) was used in the transmission mode configuration. XPS was also performed to look at the valence band by using AlK$_\alpha$ source. A commercial epilayer (TDI, USA) of 2μm GaN grown by HVPE was used in this study as a reference sample. CL spectra were obtained at room temperature using a beam acceleration voltage of 20 kV. XPS measurements of core as well as valence band level were performed using an instrument (Omicron, Germany) operating at a base pressure of 1x10$-$9 Torr.

4.3   Results:

The plan view FESEM images of the four samples (Figure 4.1) grown for time dependent growth studies show that the network structure progressively evolves from a rough surface as seen in S1 toward a typical nanowall surface morphology in S4. While S1 mainly displays a surface with mound-like structures, some of the mounds show branching. In the image corresponding to S2, it is observed that these branches start interconnecting
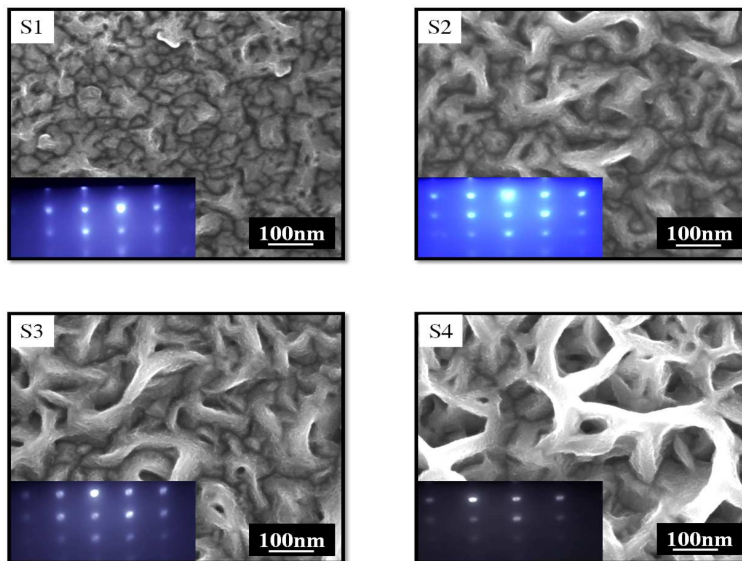
Figure 4.1: FESEM images showing the morphology of the four MBE grown samples S1-S4 with corresponding RHEED pattern as inset. All the films were deposited at 640°C

leading to a matrix of walls which forms the basis of a nanowall-network morphology. However, there is no preferential branching between certain grains unlike the case of Wu *et al.*[111]. Further, from S3 and S4 we can see that while some branches do not grow after initial joining, many continue to grow vertically leading to a wall-within-a-wall structure. Since the average Ga flux on the top surface is five or six times more than that on the side or bottom in case of three dimensional growth[171], it facilitates vertical extension of the walls and prevents coalescence. For GaN nanowires, tapering has been predicted to occur due to the flux difference, though experimental results vary[172]. We have observed tapering towards the apex of the nanowalls from the FESEM images which is quite prominent after longer growth durations (>2 hours). However, this may not result due to flux differences since then the tapering would be expected to take place much below the apex, but could be due to reduced energy of Ga adatoms adsorbing onto the sides. Insets of all the images show their respective RHEED pattern taken along $< 11\bar{2}0 >$. Typical spotty pattern characteristic of rough, three dimensional surfaces, is observed. For all the cases the c/a ratio calculated is ≈ 1.67 which confirms wurtzite structure.

Photoluminescence spectra for all the samples were obtained and are simultaneously plotted in Figure 4.2. Deconvolution of the spectra revealed that for S1 and S2, the band edge emission was very weak and was observed at 3.29 eV which is lower than the NBE value of bulk GaN of 3.4 eV. For both the samples, the spectrum was dominated by peaks
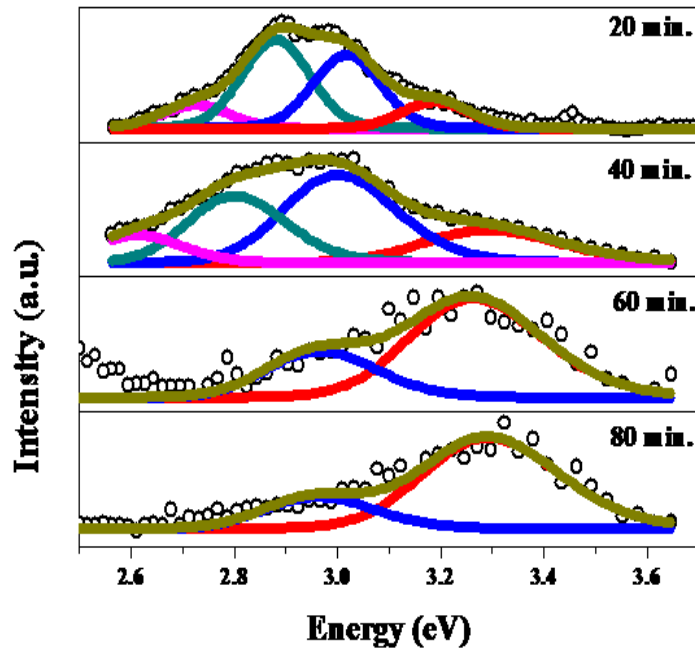
Figure 4.2: Photoluminescence spectra of the four samples plotted simultaneously. Gaussian peaks have been fitted in order to ascertain the accurate positions of the various peaks

at 3.01 and 2.79 eV in the case of S1; 2.99 and 2.80 eV in the case of S2. Peaks around 2.8 eV are generally observed in Mg-doped GaN[173], but there have been reports in case of unintentionally doped GaN films where such peaks have been observed and have been attributed to defects and large concentrations of impurities[174]. This is quite possible given the extremely low time of growth. S3 and S4 show spectra closer to a typical GaN film with a prominent band edge peak visible at 3.26 and 3.29 eV respectively. However, even in these cases, broad defect peaks at 2.96 eV can be observed which are not usually observed in such structures[175]. At very low coverages (thickness), the interfacial defects are in high density and show as low energy peaks in the range of 2.6 to 3.1 eV. However, as the nanowalls grow, the defect density reduces and only a prominent band edge peak at 3.4 eV is visible. At very low coverages (thickness), the interfacial defects are in high density and show as low energy peaks in the range of 2.6 to 3.1 eV. However, as the nanowalls grow, the defect density reduces and only a prominent band edge peak at 3.4 eV is visible. The PL results indicate that the nanowall structure is not completely formed and there still exist a lot of defects in the structure which result in extraneous

peaks in the spectra. Since the band edge emission is observed at ≈ 100 meV below the typical value of 3.4 eV for relaxed nanowalls grown on bare c-sapphire[118,175], the current structures are all strained.

(a)

(b)
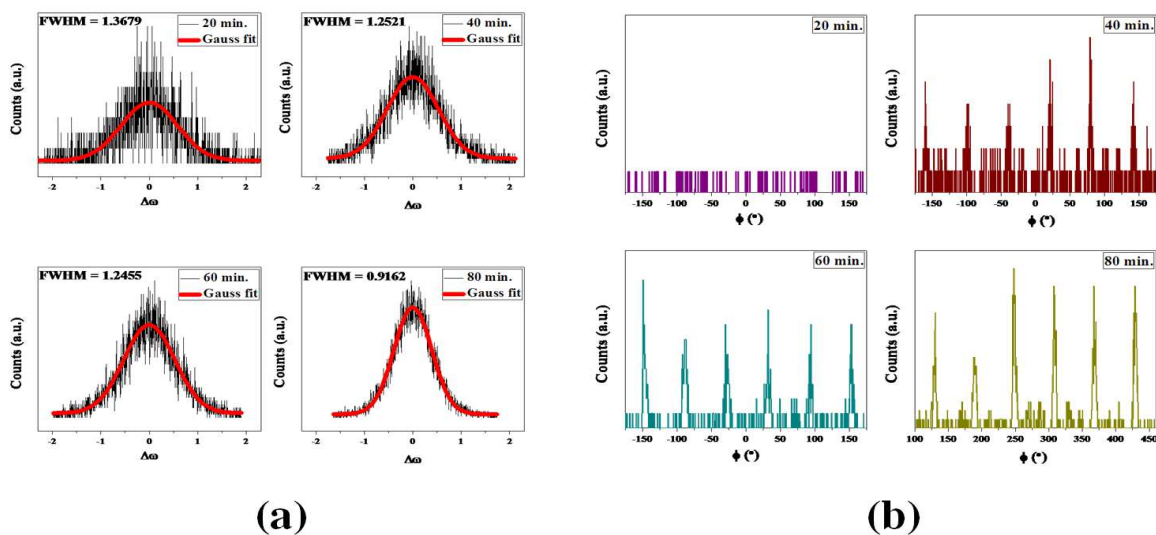
Figure 4.3: (a) (0002) XRC patterns of the four samples showing improved signal to noise ratio and a reduction in FWHM with growth time, (b) ϕ scans of all the four samples acquired along the asymmetric (114) plane

Crystalline quality of the structure can be relatively estimated using FWHM values of ω-scans, (abbreviated as X-ray Rocking Curves, XRCs). In Figure 4.3, (a) shows XRC patterns for the (0002) peak plotted for all the samples. The pattern was very noisy for S1 which has a very low coverage, but improved considerably for the other three samples. The FWHM values reduce from 1.37° for S1 to 1.25°, 1.24° and 0.93° for S2, S3 and S4, respectively, which are still much larger than the typical GaN/sapphire values of 0.08-0.14° [176,177]. The large FWHM values reflect large twist amounts in the mosaic model for highly defective films[178]. The epitaxial nature of the films was ascertained by performing the ϕ-scan for the asymmetrical (114) plane as shown in Figure 4.3 (b). Due to the extremely low coverage of the film and the asymmetry of the plane, the scattering amplitude of the diffracted wave was very low for S1, though the RHEED pattern confirms wurtzite phase of GaN. It was observed that the scan pattern improved considerably as the growth time was increased showing a typical six-peak pattern corresponding to the wurtzite symmetry in the films. The data of both ω and ϕ scans improved from S1 to S4, indicating that the nanowall growth progresses in a way that improves the crystal quality as well as promoting epitaxy.
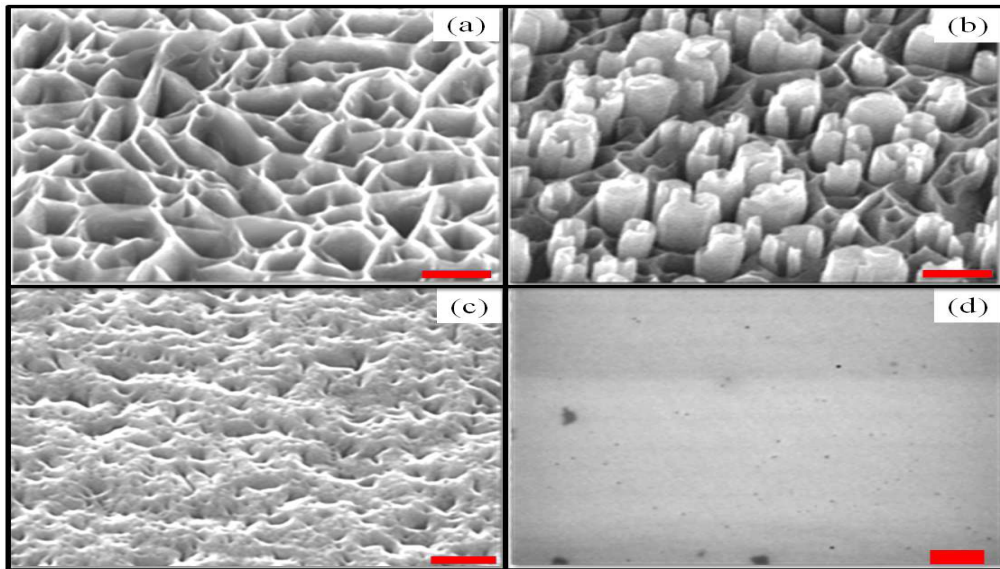
Figure 4.4: FESEM 45° tilted view images of GaN films grown on bare c-plane sapphire at (a) 630°C, (b) 680°C, (c) 730°C, and (d) is the plan view of commercially bought epilayer. The scale bars all pertain to 200 nm. The thickness of the films in all the cases was equivalent to a 600 nm flat film.

The three films grown for comparing stress and luminescence properties were first characterized using an FESEM to probe the surface morphology in all the cases. Images were taken at a tilt of 45° and the morphology of the three films grown at substrate temperatures of 630°C, 680°C and 730°C are shown in (a), (b) and (c) of Figure 4.4, respectively. The plan view of the GaN epilayer is also shown alongside in (d). The film grown at 630°C showed an interconnecting network of thin GaN nanowalls uniformly distributed all over the substrate. These wedge-shaped walls were observed to be broad at the bottom ($\approx$150 nm) and taper to about 5 nm at the apex (20 nm from the top). The cavities had dimensions ranging from 20 nm to 200 nm. In nitrogen rich conditions, the nitrogen molecules retard the diffusion of Ga adatoms, enabling their accumulation and supersaturation around the steps of the dislocations, where they are nitrided by the reactive nitrogen species from the plasma. The film grown at 680°C comprised of the network matrix, with c-oriented nanotubes growing within the cavities of the network. Kesaria *et al.* have previously shown[119] that at 680°C, the nanowalls stop growing after a certain growth duration and promote the growth of 1-D nanostructures by funneling Ga adatoms into the cavities, causing supersaturation and consequently nanorods protrude out of the network matrix. Formation of nanotubes arises from the large density of axial screw dislocations when the cost of creating a new inner surface is less than the strain

energy, rendering the dislocation core hollow[130]. Though the formation of a hollow core has been shown to alleviate the strain energy considerably, it is possible that some residual strain energy is still present. These nanotubes were observed to have dimensions varying from 50 nm to 250 nm, roughly the same variation as the size of the cavities, though most of the smaller cavities did not have nanotubes growing within them. The film grown at the higher temperature of 730°C provides higher diffusion of Ga adatoms and reduction in the sticking coefficients of N_2 molecules, and consequently a different morphology (c). The film formed is a lot flatter than the nanostructured films ((a) and (b)), and consists of a high density of pits formed from misfit induced threading dislocations. (d) shows a representative SEM micrograph of the commercially obtained GaN epilayer used in this study, showing a flat surface, for comparison.
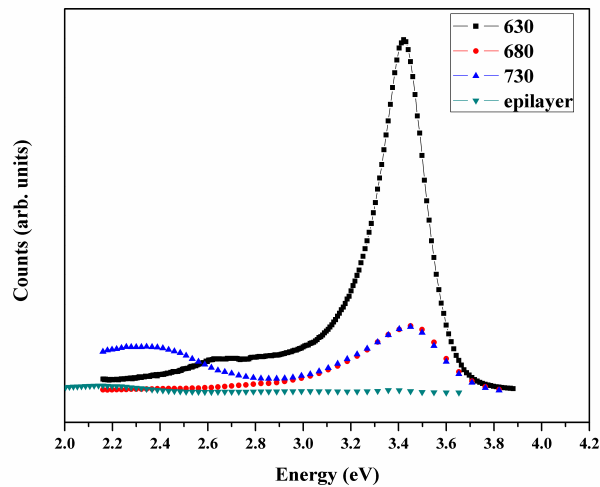
Figure 4.5: Room temperature PL spectra of the films grown at 630°C, 680°C and 730°C along with that of the epilayer.

The photoluminescence intensity of the four films has been compared by plotting the spectra of all the samples simultaneously in Figure 4.5. The film grown at 630°C had the highest intensity of the near band edge (NBE) peak which was observed at 3.42 eV, while the films grown at 680°C and 730°C had a NBE emission at 3.46 eV. Comparison of the area under the peak of all the films along with the epilayer showed an ratio of epilayer:730°C:680°C:630°C = 1:72:68:983. The photon emission was easily the largest in the nanowalls and more than ten times the other nanostructures. In flat thin films, there exists an evanescent wave which restricts the amount of light that can escape from

the surface of the film. Nanowalls reduce the total internal reflection and prevent light from being trapped within the walls which results in better light emission. The sample grown at 680°C also has nanowalls, but comprises of nanotubes as well growing inside the cavities created by the nanowall matrix. The reason for its the luminescence being significantly lower than that of pure nanowalls can be explained based on the fact that the formation of nanotubes takes place at the cost of walls which thus are truncated as compared to the film grown at 630°C. Further, the emission from the nanotubes formed by several axial dislocations is minimal, which renders a reduced emission efficiency of the system. Although no defect related peak in the 2.0-2.5 eV range was found, the luminescence intensity was very low. The sample grown at 730°C had a flat morphology and a high defect peak, but the band edge luminescence had a higher intensity than the defect peak, showing that the transitions from the defect states were less.
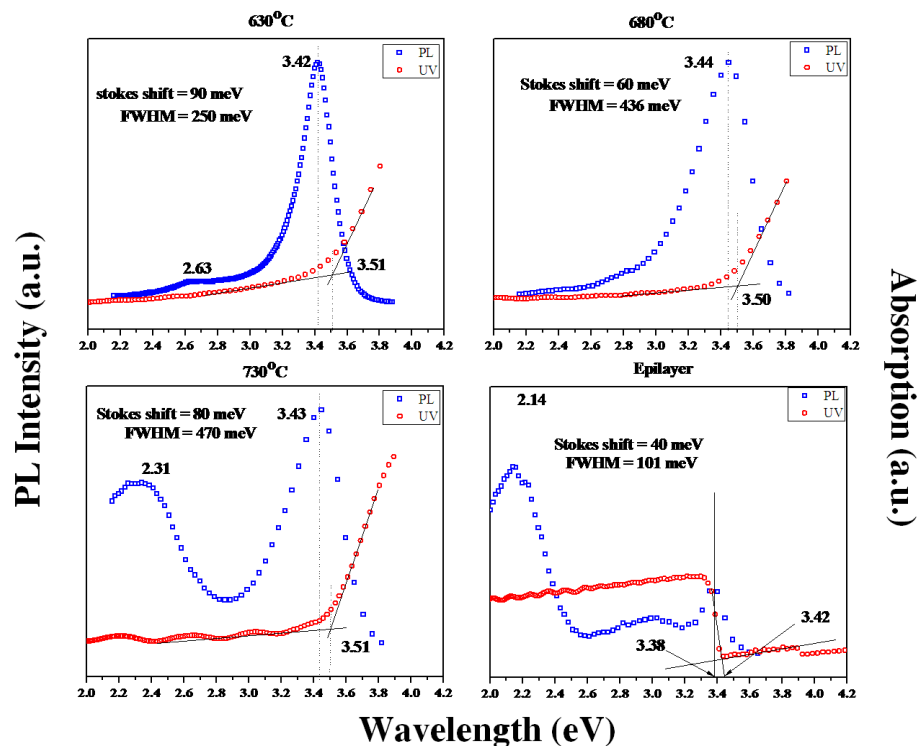
Figure 4.6: PL and absorption spectra of the GaN thin films grown at 630°C, 680°C and 730°C and that of the epilayer

To compare the two optical probes, the photoluminescence spectra and the absorption spectra for the four GaN films have been overlapped and presented in Figure 4.6. The spectra for the films grown at 630°C and 680°C showed the band edge emission at 3.42 and 3.45 eV, respectively. For the sample grown at 730°C, the spectrum had the band

edge emission at 3.44 eV and another peak at 2.31 eV which was attributed to the defect-related yellow luminescence peak. The epilayer showed a peak close to the band gap value at 3.38 eV; but there also was an intense deep-level defect-related peak at 2.14 eV. The value of the near band edge peak for bulk (unstressed) GaN film was taken to be 3.40 eV[179]. The blue shift in the three films was 40 meV, 70 meV and 60 meV in increasing order of growth temperature. Blue shifts of 30 meV are reported for GaN films grown on bare c-plane sapphire[138], and Rieger *et al.*[180] reported a strain related blue shift of 27±4 meV/GPa for GaN thin films grown on c-plane sapphire with a thin AlN intermediate layer. The blue shift is also known to be caused by a partial reduction of the piezoelectric field due to nanostructuring[181]. The FWHM of the PL linewidths were 250 meV for the nanowalls grown at 630°C, but increased to 436 meV for 680°C and 479 meV for the sample grown at 730°C, while that of the epilayer was 101 meV, suggesting the presence of band tail states below the conduction band[182]. The absorption profiles of the films were not sharp, indicating that the absorption took place over a range of energies available at the band tail states. The flat epilayer with minimal surface states, on the other hand showed a sharp absorption spike and a few oscillations (d), characteristic of a flat film. The sample grown at 630°C had the maximum Stokes shift of 90 meV while the samples grown at 730°C and 680°C showed Stokes shifts of 80 meV and 60 meV, respectively. The presence of blue shift of absorption edge with respect to PL band edge peak (at most ≈430 meV) can be attributed to the Moss-Burstein effect[183] in all the films, which have electron concentration $\sim 10^{20}$ cm^{-3}, as obtained by Hall measurements.

To understand any correlation between the differences in PL emission with the differences in nanostructures of the films, the atomic structure was probed by XRD. Bulk GaN powder was used to obtain the stress-free reference values of lattice parameters "*a*" and "*c*". The XRD pattern of the three MBE grown films along with the epilayer and the bulk powder, show the characteristic peaks of a wurtzite structure, as evidenced in Figure 4.7. Sharp, highly intense (0002) and (0004) peaks of GaN for all the films showed that all the films were highly crystalline and grew along the c-direction. For the three films grown at 630°C, 680°C and 730°C, the GaN (0002) peaks were observed at 2θ values of 34.51°, 34.47° and 34.50°, respectively. The epilayer had the corresponding peak at 34.22°, while for bulk GaN the peak was seen at 34.53°. A shift of the diffraction angle
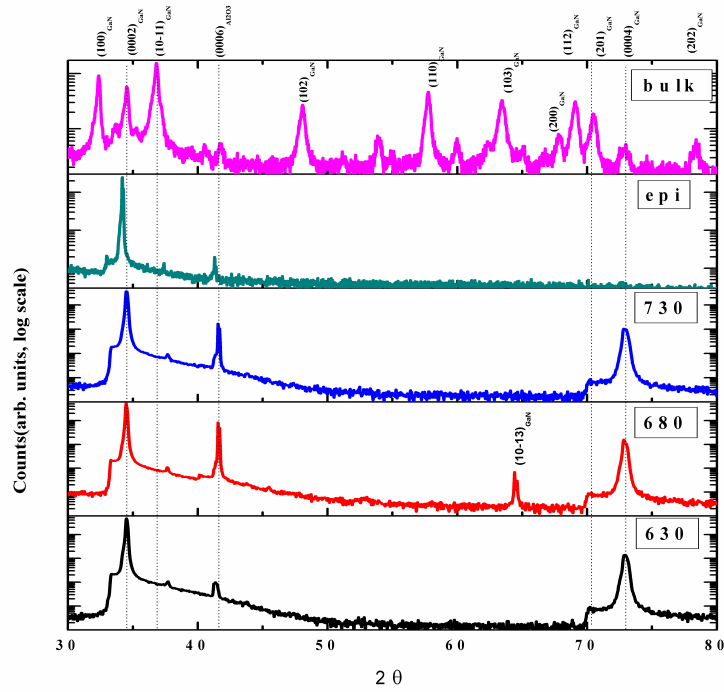
Figure 4.7: XRD patterns of the films grown at 630°C, 680°C and 730°C compared with bulk GaN powder

in XRD towards a smaller angle can be attributed to a tensile stress along that direction, causing an increase in the "c" lattice parameter. The off-axis peak of $(10\bar{1}1)$ observed in all the films, was used to calculate the "a" lattice parameter and it appeared at 37.71°, 37.65° and 37.67° for the samples grown at 630°C, 680°C and 730°C, respectively. The corresponding peak in the epilayer sample was at 37.40° and for the bulk GaN powder at 36.80°. Also, in the film grown at 680°C, we see an intense $(10\bar{1}3)$ peak, which may be due to the tilt of the nanotubes in that direction. Lattice parameters for the (0002) unit cell were calculated on the basis of angle shift ($\Delta 2\theta$) from the reference (bulk) value using Hookes law:

$$\sigma = \frac{[c - c_0]}{c_0} \frac{E}{\nu} \tag{4.1}$$

where c = lattice parameter of the film, c_0 = lattice parameter of bulk, E = bulk modulus (200GPa), and ν = Poisson ratio (0.38) . The strain values ϵ_{xx} (or ϵ_a) along x and ϵ_{zz} (or ϵ_c) along z axes are given by:

Table 4.1: Lattice parameters, stress and strain values calculated from XRD data for films grown at different temperatures

Growth temp.	Lattice parameter "a" ($\mathring{A}$)	Lattice parameter "c" ($\mathring{A}$)	Stress along c direction (GPa)	Strain along c direction	Strain along a direction	Calculated $\frac{C_{13}}{C_{33}}$	Valence band offsets (eV)
630°C	3.0960	5.1920	0.35	6.55×10^{-4}	-2.92×10^{-2}	0.011	1.82
680°C	3.1015	5.1992	1.07	2.04×10^{-3}	-2.74×10^{-2}	0.037	2.56
730°C	3.1013	5.1938	0.53	1.00×10^{-3}	-2.75×10^{-2}	0.018	2.16
Epilayer	3.1159	5.2345	4.65	8.85×10^{-3}	-2.29×10^{-2}	0.193	2.58
Bulk	3.1891	5.1886	-	-	-	-	

$$\epsilon_{xx} = \frac{a_f - a_b}{a_b}, \epsilon_{zz} = \frac{c_f - c_b}{c_b} \qquad (4.2)$$

where a_f and c_f = "a" and "c" lattice parameters of film, and a_b and c_b = "a" and "c" lattice parameters of bulk. The computed stress and strain values are tabulated along with the lattice parameters obtained from XRD in Table 4.1. It is also possible to calculate these values if the elastic constants of GaN are known accurately. In literature, these values are highly scattered as tabulated by Kisielowski *et al.*[138]. From the strain values obtained using lattice parameters, we have calculated the ratio $\frac{\epsilon_c}{\epsilon_a}$ which is related to the elastic constants by the equation $\frac{\epsilon_c}{\epsilon_a} = -2\frac{C_{13}}{C_{33}}$. The ratio $\frac{\epsilon_c}{\epsilon_a}$ was found to be 0.022, 0.074, 0.036 and 0.386, for the samples grown at 630°C, 680°C, 730°C and the epilayer, respectively. These values are in accordance with the ones calculated in ref.18 using lattice parameters, which reports a variation of $1.5 > \frac{\epsilon_c}{\epsilon_a} > -1.5$ for GaN films grown by various groups. The variation in the ratios of the known values of elastic moduli, though, has been calculated by them to be between $-0.27 > \frac{\epsilon_c}{\epsilon_a} > -1.18$, which explains the variation in our strain values calculated separately using lattice parameter and bulk modulus values. Further, the assumption that our films have dominant biaxial strain cannot be made, since that would lead to a $\frac{\epsilon_c}{\epsilon_a}$ ratio of -0.6 ± 0.2. According to the deductions made in ref.18 based on the strain ratios, we remark that a combination of biaxial stress in the basal plane ($\sigma_a = \sigma_b, \sigma_c = 0$) and partial hydrostatic pressure ($\sigma_a = \sigma_b = \sigma_c = \sigma_p$) is present in our films. The valence band offsets calculated by XPS valence band spectra are also included in the table for various films. Since all the films were n-type, the Fermi level was closer to the conduction band as expected.

Since the films are c-oriented, the z-axis is parallel to the growth direction. Calculations from the XRD peaks for all the samples showed a smaller "a" lattice parameter and a larger "c" lattice parameter in comparison to those obtained for the bulk powder GaN sample. This biaxial stress present in all the films arises due to residual as well as thermal stresses during growth processes[138]. In the GaN/Al_2O_3 system, due to the smaller thermal expansion coefficient of GaN with respect to that of sapphire, a biaxial compressive stress is generated in the xy plane, which can induce a tensile stress in the z-direction[162].

Though strains also manifest as shifts in the band gap, as mentioned previously, our results did not show any clear correlation between stress values and PL line shifts. This led us to believe that strains are not the only cause of the spectroscopic line shifts[138]. Since all the peaks were blue-shifted with respect to bulk value, we can infer that the compressive stress in the films was the dominant force. This observation is contrary to the report by Seo *et al.*[162] where they have observed a red shift in the PL peak positions, and attribute the broadness of the PL band to differently strained domains within the structure. Calleja *et al.*[79] attribute the wide spectral dispersion observed in GaN nanorods grown on Si(111) to interactions of the defects with local strain and/or electric fields at the column-substrate interface. Recently, Lee *et al.*[184] suggested that the broadness of the PL spectrum can be due to the inhomogeneity in the distribution of nonidentical nanorods. However, since our PL spectra of the nanostructures (630°C and 680°C) do not show significant defect related emission, the broadness of our PL spectra of nanostructures was attributed to non-radiative defects, originating at the interface during growth, resulting in a strained structure. The flattest of the films grown at 730°C had a high dislocation density which causes the high FWHM in the PL band edge peak.

The band structure of wurtzite GaN with C6v symmetry is presented and the shifts of various bands as deduced from the experimental results are shown for each sample in Figure 4.8. The E vs k band diagram of an unstrained film is shown alongside the three MBE grown films for comparison. Since all the films were compressively strained, the band shapes do not change, as the C_{6v} symmetry is maintained. The relative positions of the hole bands also do not change with respect to each other due to the wurtzite structure of the films, as already seen by XRD. The only difference in the valence band structures
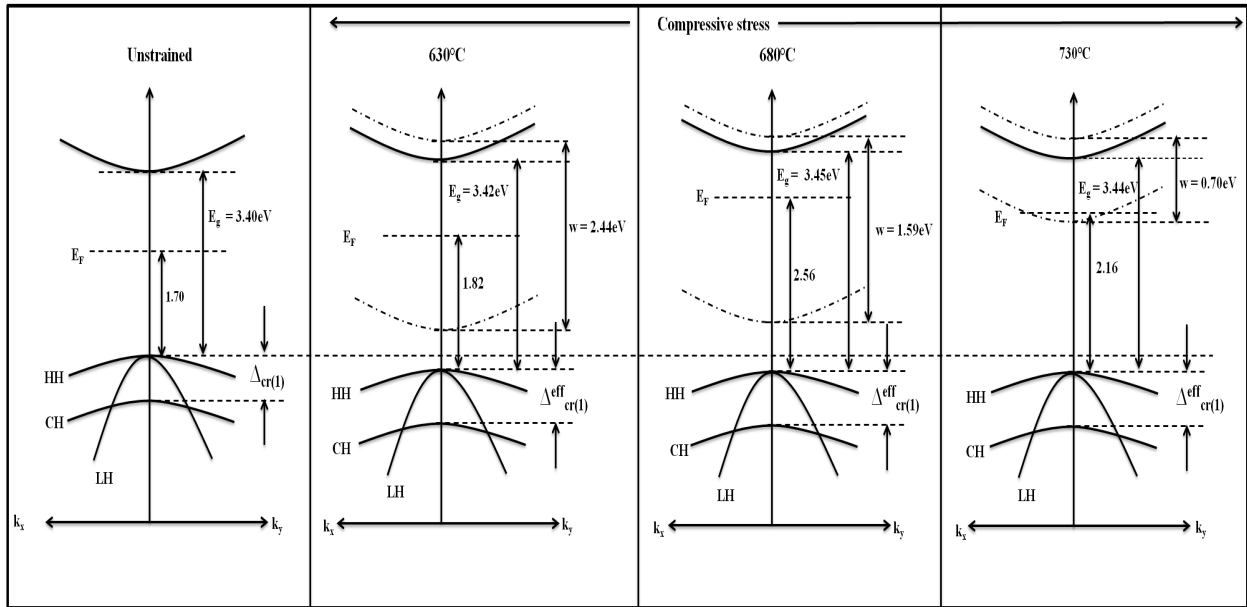
Figure 4.8: Band diagram of the three films grown at 630°C, 680°C and 730°C with respect to an unstrained GaN film.

are that there is a significant increase in the crystal-field splitting energy (Δ_{cr}) due to the compressive strain in the films, and there is a compressive-stress related slight downward movement of the hole bands (heavy hole (HH), light hole (LH) and crystal-field split-off (CH)). From the absorption spectra, the width of the conduction band was calculated to be 2.44 eV, 1.59 eV and 0.70 eV for the samples grown at 630°C, 680°C and 730°C, respectively. The decreasing width of the conduction band points to the fact that the available states for absorption decrease continuously with increase in growth temperature. Hence, in the nanowall network sample grown at 630°C, there is an abundance of empty states in the conduction band of energies as wide as 2.46 eV, reinforcing the thought that there is a huge density of band tail states in these structures. From the XPS valence band studies (not shown), the position of the valence band maximum (VBM) was calculated with respect to the Fermi level. The Fermi level was found to be situated at 1.85 eV above the VBM for the nanowalls (630°C), at 2.58 eV for the nanotubes (680°C) and at 2.15 eV for the flat film (730°C). Since all the films showed n-type conductivity in the Hall measurements, the XPS results further corroborate that fact. The band edge values calculated by photoluminescence measurements are also shown in the diagram, with all the MBE grown films showing values higher than an unstressed film.

For probing the electronic structure, two MBE grown films were compared with an
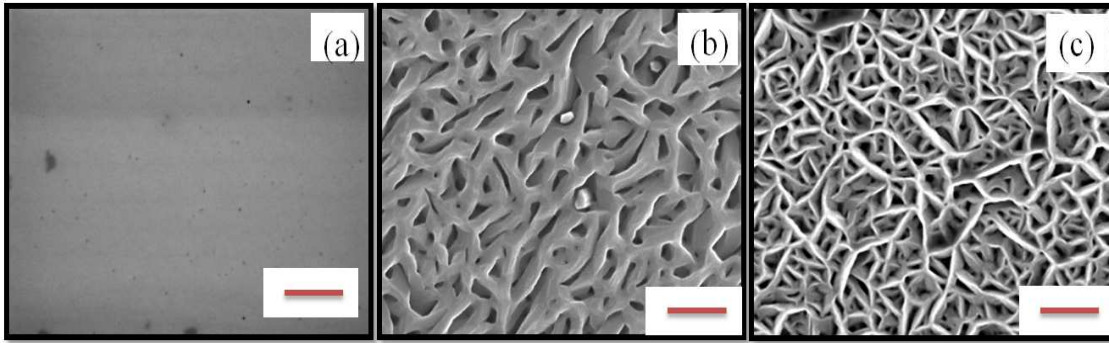
Figure 4.9: Plan view SEM images of all the three films are shown. (a) is the micrograph of the commercially available GaN epilayer, (b) is the flat-tipped GaN nanowall network sample grown by MBE at a substrate temperature of 680°C (sample 1) and (c)is the sharp-tipped network, grown at 630°C (sample 2). The scale bars all pertain to 300 nm.

epilayer. The plan view FESEM images of the three films studied, namely GaN epilayer and two GaN nanowall network samples with differing morphology is shown in Figure 4.9. The plan view images shown in Fig. 4.9 refer to only the top surface and a part of the uniformly covered GaN surface is shown in the micrographs. Cross section images of these films (not shown here) clearly show that the voids taper along the depth and become very small at the GaN/Al$_2$O$_3$ interface. The sample grown at 680°C (hereafter called as sample 1) has a flatter apex (tip) ($\approx$70 nm) compared to that grown at 630°C, which has a much sharper tip ($\approx$15 nm) (sample 2). Consequently, the surface coverage of sample 1 is much more ($\approx$45%) than sample 2 ($\approx$26%). Coverage in this case is the plan view ratio of area covered by walls, and tells about the porosity of different sample configurations. This is determined by Gwyddion, an image analysis software, with appropriate thresholding. The thickness of sample 1 is estimated to be 624$\pm$10 nm while that of sample 2 is 686$\pm$10 nm from cross sectional SEM images.

Cathodoluminescence spectra recorded at room temperature for all the samples in Figure 4.10 shows a clear near band edge (NBE) peak with no defect emissions. This is concomitant with such previous observations[118] in similar samples. The NBE emission from epilayer occurs at 3.39 eV and is weak. For sample 1, the band edge emission occurs at 3.40 eV, close to epilayer value. However, for sample 2, the NBE emission occurs at 3.43 eV, displaying a clear blue shift of $\approx$60 meV towards higher energy. The epilayer had the narrowest FWHM of 80 meV, while that of sample 2 is the broadest at 218 meV, and sample 1 gave an intermediate FWHM value of 130 meV. This observation
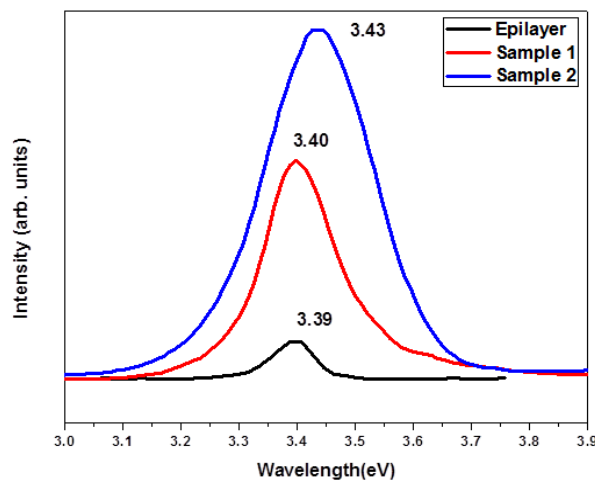
Figure 4.10: Cathodoluminescence (CL) spectra of all the three films plotted in the same graph with absolute intensities.

is in keeping with the photoluminescence studies made on similar films earlier, which showed that there is a high density of band tail states near the conduction band in the nanowall network morphology. The cathodoluminescence studies show similar results to the photoluminescence spectra observed earlier where the NBE emission from the nanowall structure is observed to be orders of magnitude higher than the epilayer. This is attributed to better light extraction efficiency from the nanowall surface that has low defect density, lower strain and a geometry that reduces total internal reflection

X-ray photoelectron spectroscopy (XPS) core level spectra for Ga 2p, Ga 3d and N1s, and the valence band spectra are acquired to observe any morphology dependent changes for different samples. Figure 4.11 shows the (carbon-corrected) Ga 3d and N 1s core level scans for all the films studied in the present case. Since the XPS studies are performed *ex-situ*, in order to observe any surface oxidation the Ga 3d peak of sample 2 is deconvoluted into Gaussian components corresponding to metallic Ga, GaN and Ga_2O_3 using appropriate FWHM values from literature[185] and is shown as an inset. From the area under the curves, it is clear that the major Ga 3d peak component is from GaN, and minor contributions are from the Ga-Ga or Ga-O bonds. So, we can attribute the observed valence band spectra to manifest the bonding between different atomic levels of Ga and N. All the Ga 3d peaks for the MBE-grown samples appear on the higher energy side as compared to the epilayer. The peak positions of Ga 3d semicore state are 19.6,
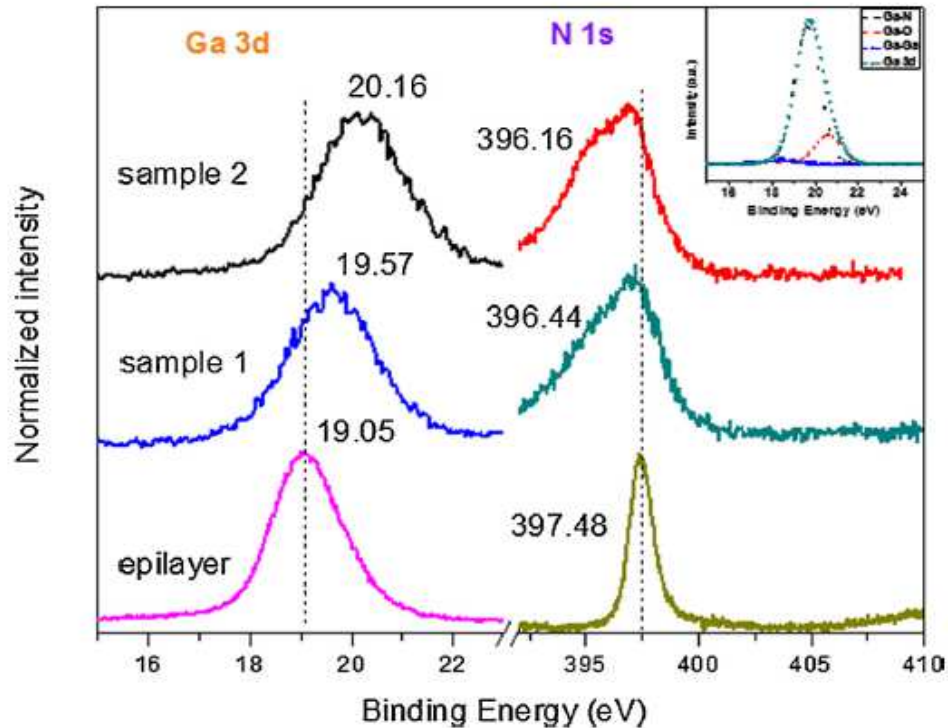
Figure 4.11: XPS core level Ga 3d and N 1s peaks plotted for all the samples, (Inset) Ga 3d core level peak for sample 2 deconvoluted into Ga Ga, Ga N and Ga O related components

19.5 and 20.2 eV for the epilayer, sample 1 and sample 2, respectively. These values are in agreement with previously reported values[186,187]. The epilayer has the least FWHM of 1.7 eV and the MBE grown samples also have comparable values of 1.8 eV and 1.7 eV for samples 1 and 2, respectively. The N 1s peak for the epilayer is observed at 397.5 eV, but for sample 1 and 2 these peaks have binding energy values of 396.4 and 396.2 eV, respectively. The FWHM of the N 1s peaks is calculated to be 1.2, 4.4 and 4.3 eV for the epilayer, sample 1 and sample 2, respectively. The width and a slight asymmetry observed for these peaks have previously been attributed to the presence of chemisorbed nitrogen on the surface along with the nitrogen species in GaN[188]. The Ga:N ratio is determined using Auger peaks and the value for the epilayer is taken as stoichiometric value of 1:1. It is seen that for the MBE grown nanowalls, the surface is richer in Ga, with sample 2 having a Ga:N atomic ratio of 1.6 while sample 1 had a ratio of 1.3. Though the films are grown in nitrogen rich conditions, it has been universally seen that they result in nitrogen vacancies (Ga-rich) surfaces[81]. Though the mechanism is not very clearly understood, the surface energies and low sticking coefficient of the side walls are speculated to create

nitrogen vacancies on the surface due to energy minimization. The gallium richness of the surface due to nitrogen vacancies is also reflected in the Hall measurements carried out on these samples (not shown) which gave a high sheet carrier concentration of $\sim10^{16}$ cm^{-2} and a conductivity of $\sim10^{2}\Omega^{-1}$cm^{-1}, indicating the high metallicity of the surface, while corresponding values for the GaN epilayer are $\sim10^{14}$cm^{-2} and $\sim2\mathrm{x}10^{1}\Omega^{-1}$cm^{-1}, respectively.
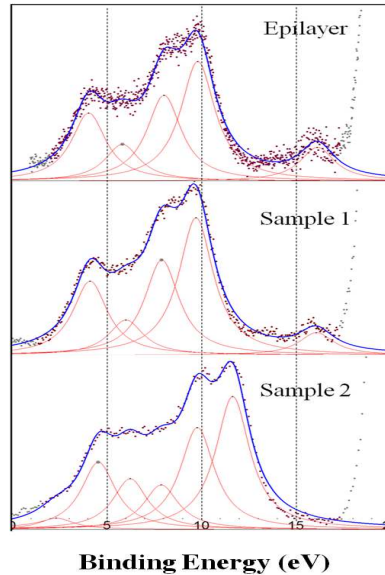
Figure 4.12: Valence band spectra plotted for all the samples. Peaks have been fitted to highlight the hybridized energy levels

The valence band spectra for all the three films shown in Figure 4.12, have been deconvoluted in order to explore the differences in energies of various hybridization levels of the three films, similar to studies done for other materials as reported by Bellardita *et al.* and Jiang *et al.*[189,190]. Figure 4.12 shows the three spectra comparing the fitted peaks according to their energies. For the epilayer and sample 1, the spectra is satisfactorily reproduced by five Gaussian peaks, but for sample 2 an additional peak is required. The peak positions for all the samples are tabulated in Table 4.2. Comparisons with theoretical calculations and experimental measurements previously reported[191] for GaN reveal interesting changes in the valence band for the three morphologies. For sample 2, a peak appears at 2.3 eV, which is close to the energy range of 1-2 eV below the Fermi level for the N 2p-Ga 4p hybridization as attributed in the above reference. However, this peak is absent in the spectra obtained for the epilayer as well as sample 1. A prominent peak appears at 4.0 eV for the epilayer and at 4.1 and 4.6 eV for sample 1 and sample 2,

respectively; and is attributed again to the hybridization between N 2p and Ga 4p levels. Although this peak lies outside the energy range mentioned earlier for this hybridization level, the theoretically obtained curve shows the presence of a non-zero density of states in this energy region[191] and hence such an attribution is reasonable. A small peak due to the hybridization between the N 2p-Ga 4s energy levels appears at 5.8 and 5.9 eV for the epilayer and sample 1 respectively. For sample 2, a similar feature around the same energy required two peaks at 6.2 and 7.9 eV for reasonable fitting. Since the band structure of GaN shows no energy state between 7 and 11 eV, the feature at 7.9 eV is a satellite. Another doublet observed further down the valence band at 7.9 and 9.8 eV for the epilayer appeared at 7.8 and 9.7 eV for sample 1, and at 9.8 and 11.6 eV for sample 2. This doublet appears in the forbidden region as mentioned earlier, and is attributed to the satellite feature caused by the charge transfer from Ga 4s to N 2p band, as previously observed by Magnuson *et al.* Relative shift between the all the hybridization peaks for sample 1 and 2 is explored by aligning the Ga 3d level (not shown) and it is confirmed that for sample 2, the peak at 6.2 eV shifts ≈0.3 eV lower than that for sample 1, while the satellite doublet observed between 9-11 eV shifts by ≈1.3 eV towards higher binding energy. The higher hybridization energy of this satellite for sample 2 indicates a greater degree of charge transfer, leading to stronger bonding strength. A lower energy of N 2p-Ga 4s hybridization feature does not affect the bonding strength as much, since it occurs very near to the top of valence band. In the region of -15 to -17 eV near the bottom of the valence band, a small peak corresponding to the hybridization between N 2s, N 2p and Ga 4s is detected for epilayer at 16.1 eV and at 15.9 eV for sample 1. No such peak is observed for sample 2, which is explained by the fact that this peak merges with the core level Ga 3d peak of sample 2 due to the same shift as mentioned earlier.

Table 4.2: Peak positions for the hybridized levels as observed from the valence band spectra for the MBE grown samples compared with the epilayer

	Epilayer	Sample 1	Sample 2	Hybridized Level
			2.32	N 2p-Ga 4p
Peak positions (eV)	4.02	4.10	4.55	N 2p-Ga 4s*
	5.79	5.99	6.23	N 2p-Ga 4s
			7.86	
	7.99	7.87	9.78	Satellite
	9.77	9.67	11.64	
	16.08	15.99		N 2p-N 2s-Ga 3d

With the epilayer values as reference, it is observed that for both the MBE grown samples the general binding energies for hybridized levels are higher, indicating a more relaxed structure. Further, for sample 2 an extra shift of ≈1.9 eV towards higher binding energy is observed for the hybridized level N 2p-Ga 4s. This shows that as the nanostructure evolves to a steeper wall, the electronic structure is further stabilized. Such an observation is in keeping with previously demonstrated results that the stress is relaxed in the nanostructured films and reduces as the structure evolves to a more open network[175].
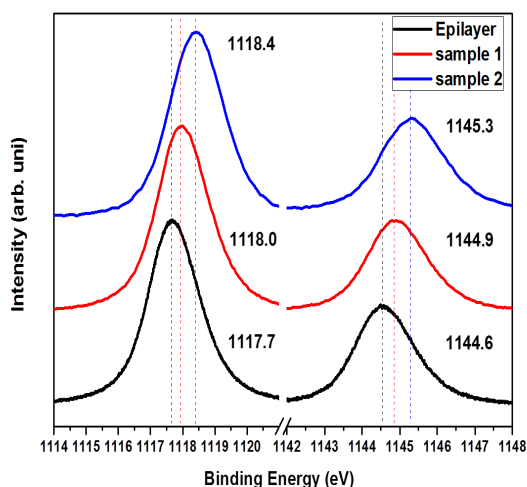
Figure 4.13: XPS core level Ga 2p doublet photoemission peak spectra of all the three samples

Ga 2p peaks are also compared for all the three samples to probe the branching ratio between the two components, as shown in Figure 4.13. The spin-split peaks of Ga 2p with theoretical values (pure Ga) at 1117 eV and 1144 eV correspond to $2p_{3/2}$ and $2p_{1/2}$ respectively. For our samples, the shift in the peaks is minimum in the epilayer and maximum in sample 2. Branching ratios (BR) are calculated using the formula $I(L_3)/[I(L_2)+I(L_3)]$ and compared with the literature values in order to estimate the degree of spin-orbit splitting in the nanowall network configuration. For our samples, the BR values are 1.831, 2.066 and 2.057 for the epilayer, sample 1 and sample 2 respectively. Since the statistical $p_{3/2}$: $p_{1/2}$ ratio is 2:1, the partial cross section is highest for sample 1 and therefore the initial-state effect is the maximum, showing that the *j=l+1/2* orbital is preferentially ionized[192]. However, since the values for sample 2 is also very close, we can

comment that the two nanostructure morphologies have a higher partial cross section than the epilayer. Earlier, several theories have been proposed for the reason behind the change in BR, with a general consensus that difference in the photoelectron wave functions (radial parts as well as phase shifts) of the two spin-orbit components are the major cause of such a change[193].
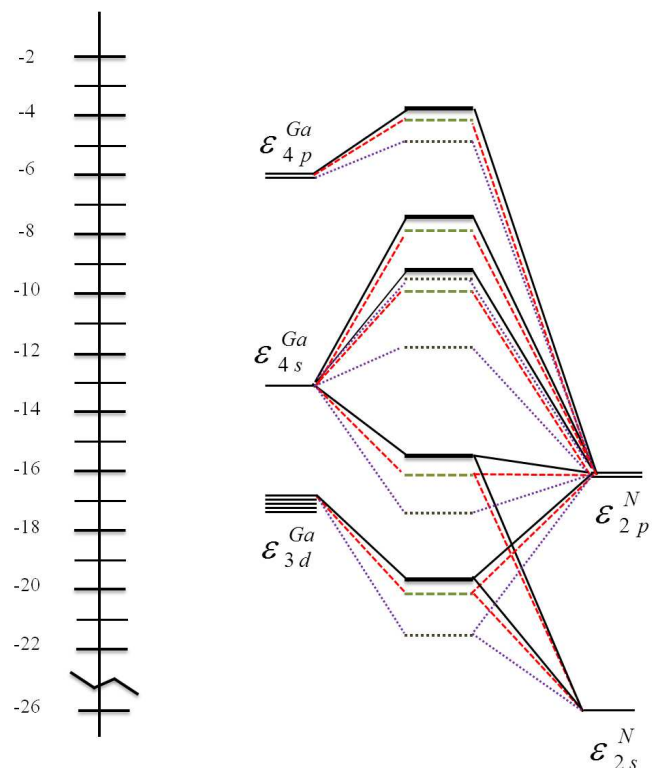
Figure 4.14: Schematic band diagram showing the bonding between atoms and the change in the positions of hybridized states compared to the epilayer sample 1(dashed lines) and (b) sample 2 (dotted lines).

A schematic band diagram for samples 1 and 2 comparing the separation in hybridized levels to those of the epilayer has been plotted in Figure 4.14, consolidating the results. Atomic energy levels are shown on either side of the hybridized levels in the center. The shifted hybridized levels are shown as broken lines below the solid black lines, which are the positions of the levels in case of epilayer. For all the hybridized levels, it is observed that in the case of sample 2, the separation is higher from epilayer compared to sample 1. The hybridized level corresponding to Ga 4s-N 2p is observed at an energy of 9.53 eV for sample 2, compared to 7.37 and 7.97 eV for the epilayer and sample 1, respectively. This clearly indicates a lowering in bonding energy implying a more stable structure, and hence we observe that thin nanowalls give a much more electronically stable structure compared to thick nanowalls or a flat epilayer.

4.4 Summary of Chapter 4:

To summarize this chapter, GaN nanowall network structures were epitaxially grown on bare c-Al$_2$O$_3$ substrates using PA-MBE. Time dependent growth showed that the films

followed a Volmer-Weber growth mode and some walls grew for a certain time and stopped while others grow further, giving rise to a wall-within-a-wall morphology. Enhanced luminescence was observed in the nanowall structure compared to other nanostructured films grown by PAMBE as well as a flat epilayer. Stress and strain values were lower than flat films and a band energy diagram was plotted which showed an interesting stress state in the nanowalls which differed from the conventionally expected biaxial strain state. A combination of biaxial strain and partial hydrostatic stress was speculated and the resultant strain shifted the hole bands to a lower energy level. A large density of band tail states was present in all the nanostructures and the nanowalls exhibited the largest of them. The electronic structure was further probed using XPS valence band spectra and it was seen that the charge transfer between Ga 4s and N 2p energy levels which was interpreted as the nanowalls having a more stable electronic structure.

Chapter 5

Transport properties and photoluminescence enhancement of GaN nanowall network

5.1 Introduction:

In the previous chapter, we observe quite a few interesting properties of GaN nanowalls. From the photoluminescence results described in the previous chapter, it is evident that the optical properties of nanowalls are clearly superior to other MBE grown nanostructures and flat epilayers. Two unique properties of the GaN nanowalls, namely dislocation filtering and their geometry, improve the optical properties. The reduced defects enhance recombination and the angles of the nanowalls reduce total internal reflection. Both these factors enhance light emission from this structure. There are a high density of band tail states which was apparent due to large Stokes shifts. Although the bond strengths were higher as seen in XPS, it is still interesting to probe other electronic properties such as mobility and conductivity to better understand the behaviour of electrons in the structure. Further, since the photoluminescence from the band edge is very intense, it is attractive in terms of applications in light emitting devices. For this purpose, it is also reasonable to make attempts to improve the emission even more to exploit the potential of the nanowall structure to the maximum. There are two

promising areas of GaN nanowall application which are going to be further investigated in this chapter, first the electron transport properties and then some attempts are made for photoluminescence enhancement.

5.1.1 Electron Transport:

Introduction:

Due to the low dimensional nature of the nanowalls, probing electron transport within them is of interest in terms of realizing nanoscale devices. Recently, it has been found that a network of GaN nanowalls show certain interesting structural, optical and transport properties[115,116,118,119,159,182,194]. Electron mobility (μ) in c-axis oriented wedge shaped GaN nanowall networks grown on c-sapphire substrates has been estimated to be several orders of magnitude larger[182] than GaN thin films[195]. In order to confirm this observation, more experiments need to be performed to independently obtain and then compare mobility values. The van der Pauw method needs a flat surface to accurately determine the resistivity. If the structure is porous, the contact between the probe and the surface is not 100% which gives rise to an error in measurement. Hence, in our case, the values of resistivities are not absolute, but are meant to be used as a comparison between similar samples Magnetoresistance (MR) is also an indicator of mobility in semiconductors with single carrier type since it is directly proportional to $(1 + (\mu B)^2)$ where μ is the semiconductor mobility. Hence, for a film with high mobility, the MR would be very high. Apart from the MR measurements, four probe measurements of the resistivity is also performed. Since the earlier reports[182] speculated the top part of the nanowalls to be more conducting, etching has been performed and resistance has been calculated at constant time intervals to study the change in the resistance with morphology. Photoconductivity measurements have also been performed and compared with photoluminescence graphs to analyze the presence of band tail states.

Experimental Details:

The transport properties were initially studied using four GaN nanowall network samples with differing morphologies which were grown on c-plane sapphire substrate using

PA-MBE. The N_2 flow rate (4.5 sccm) and duration of growth (2h) was kept constant for all the samples and the substrate temperature was varied. The four temperatures used in this study are 630 °C (sample A), 650 °C (sample B), 530 °C (sample C) and 780 °C (sample D). The order of temperatures is odd since the samples have been chosen in such a way that there is a continuous reduction of the dimension of the top of the walls. Line scans were performed on the SEM images to ascertain the tip widths of the nanowalls. The average electron concentration (n) was obtained by measuring the thermoelectric power at 300 K for these samples. Magneto transport measurements were carried out in a liquid He-cryostat equipped with a superconducting magnet in the temperature range of 1.8 K to 5 K. Magnetic field was varied between ±500 Oersted (Oe). Indium (In) contact pads, which result in good ohmic contacts, were fabricated on the sample surface. Four probe resistivity measurements were carried out in the Van-der-Pauw geometry to obtain the conductivity values. A nanowall sample grown at 640°C for 4h was used for chemical etching dependent transport property measurements, where 4M aqueous solution of KOH was used as the etchant.

Results:
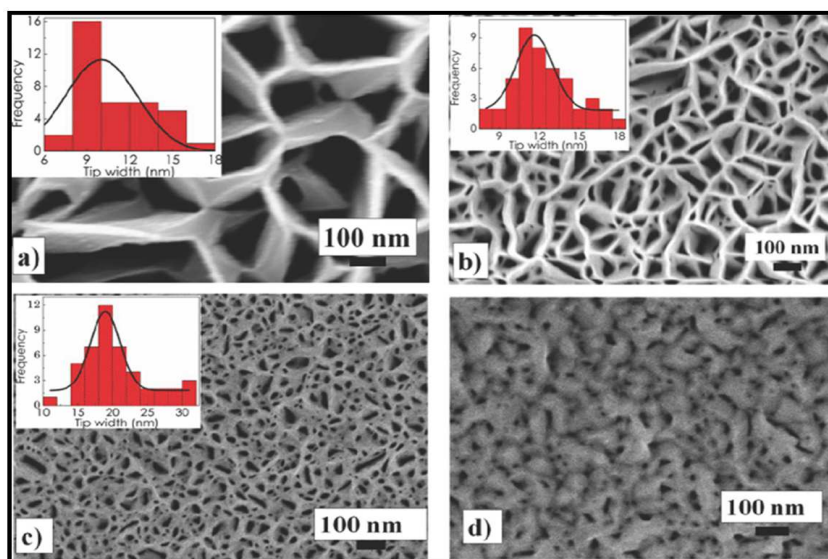
Figure 5.1: Top view SEM images for the samples A, B, C and D with histograms representing the distribution of the tip width of the walls as insets

The plan view SEM images for all the samples are shown in Figure 5.1. Nanowall structure can be seen to be present homogenously all over the substrate in all cases.

Sample D does not show the typical nanowall morphology and the surface consists of mound like structures which have voids within them. The nanowall tip width (t_{av}), plotted in the histograms in the insets of (a), (b) and (c), was obtained by analyzing line scan profiles on the SEM plan view images. The details are given in a previous publication of our group[182] Within the error incorporated in the SEM imaging, it can be seen that the tip width steadily increases from A to C. While the surface of sample A is only 40% covered, the coverage increases as 59, 72 and 80 % for B, C and D, respectively.
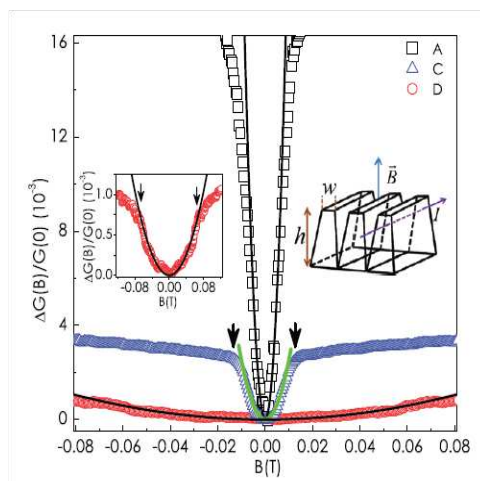
Figure 5.2: Relative change in conductance ΔG(B)/G(0) = (G(B)G(0))/G(0) measured at 2 K as a function of the magnetic field B for different samples. Left inset of the figure shows ΔG(B)/G(0) plot in close-up for samples D. Right inset schematically shows the direction of the external magnetic field B and current "I" with respect to the orientation of the walls. Solid lines in the figure represent the fitting of the data using the model discussed in the text.

The relative change in conductance ΔG(B)/G(0) = (G(B) G(0))/G(0) was measured at 2 K as a function of magnetic field B for different samples and is shown in Figure 5.2. Left inset of the figure shows ΔG(B)/G(0) plot in close-up for the samples D. In all samples, an increase of conductance with magnetic field (negative MR) is clearly visible at low fields. For highly doped semiconductors in weak magnetic fields, this effect is known to be caused due to weak localization (WL). WL is a result of constructive interference between two electron waves traversing the same path in opposite directions and leads to an additional contribution to resistance. The presence of a magnetic field in such a case gives a phase difference Φ/Phi_0, where Φ is the magnetic flux through the electron path and $\Phi_0 = \hbar/2e$ is the flux quantum. The magnetic flux so applied violates the interference conditions and the additional contribution from the WL decreases, leading to a negative

MR. The indication of weak localization further means that spin orbit coupling is weaker since in a system with strong spin orbit coupling, the spin of the carrier couples to its momentum. The spin rotates in opposite directions for two electron waves which leads to a destructive interference and a net lowering of resistivity. Comparing different samples, it was observed that for sample A, where the width of the nanowalls is the smallest at 10 nm, $\Delta G(B)/G(0)$ changed much faster than that of sample C and D, where $t_{av} \approx 20$ and 60 nm, respectively. Since $\Delta G(B)/G(0)$ increases more rapidly as the average wall width decreases, the WL effect is much stronger in the thinner nanowalls. This is intuitive, since in low dimensions it is easier to find a self crossing trajectory compared to bulk. Right inset of the figure schematically represents the direction of the external magnetic field B and current I with respect to the orientation of the walls.
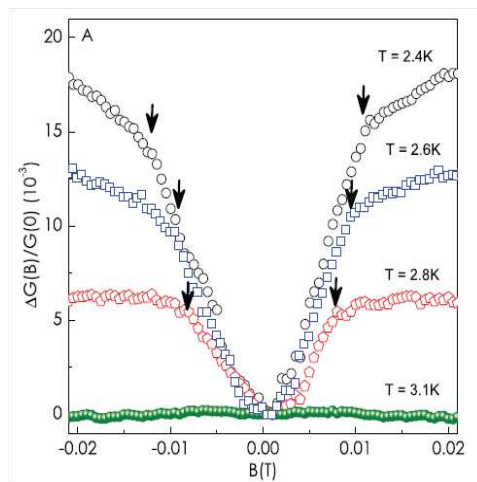
Figure 5.3: Compares the $\Delta G(B)/G(0)$ profiles for sample A recorded at different temperatures. It is noticeable that $\Delta G(B)/G(0)$ increases monotonically up to a magnetic field B_c (marked by arrows in the figure), beyond which the rate abruptly decreases.

Sample A showed the strongest signature of MR and in order to observe the temperature dependence of the same, $\Delta G(B)/G(0)$ profiles were recorded at different temperatures for sample A and are presented in Figure 5.3. As expected, $\Delta G(B_c)/G(0)$ decreases continuously with temperature as phonon effects cancel the electron scattering associated with WL. Above 3 K, the MR becomes so small that hardly any WL effect is seen. The direction of magnetic field with respect to the sample is also important as it has a direct impact on the motion of electrons which can give more information about the transport properties. In this experiment, magnetic field is applied perpendicular to the sample surface and is thus acting along their growth as schematically shown in the

inset of Figure 5.2. Beenakker and Houten have shown that for a thin layer, which is subjected to a magnetic field acting parallel to the layer plane, the quantum correction to the conductance as a function of the magnetic field can be expressed as[196]:

$$\Delta G^{wl}(B) = -N_{ch}\frac{e^2}{2\pi^2\hbar}ln[(\frac{\tau_e}{\tau_\phi} + \frac{\tau_e}{\tau_B})^{-1} + 1] \qquad (5.1)$$

where τ_e is the mean free time between two elastic collisions, τ_ϕ the phase coherence time and τ_B the magnetic field dependent phase coherence time. $\tau_B = C_1\hbar^2/w^3e^2B^2v_f$ in weak magnetic field regime $[l_m \gg \sqrt{wl_e}]$, where $C_1 = 16$ and 12.1 for diffused and specular surface scattering, respectively, v_f the fermi velocity, $l_e = \tau_e v_f$ the mean free path, $l_m = \sqrt{\hbar/eB}$ the magnetic length and w the thickness of the layer. The prefactor $N_{ch} = 1$ for a single film. However, in case of parallel network of walls, multiple parallel channels connecting the contact pads should be considered. N_{ch}, which should now be the effective number of parallel channels connecting the contact pads, can thus be larger than one. It should be noted that the above expression for τ_B is valid as long as $l_e \gg w$.
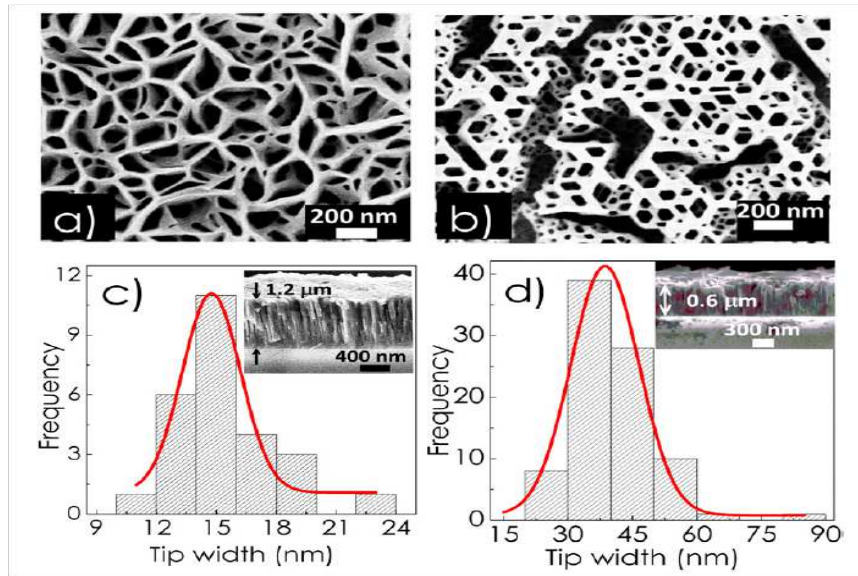
Figure 5.4: Cross section SEM image of sample E (a) before and (b) after etching in KOH solution for 50 minutes

In order to probe the electron transport at different areas in the nanowalls, etching was performed and measurements were made at different time intervals. A GaN nanowall structure grown for 4h (sample E) at a substrate temperature of 640°C was subjected to KOH etching for 50 minutes. The plan view FESEM image of the sample before etching

is shown in Figure 5.4 (a) while (b) shows the image after the etching. For clarity, let us call sample E as E-1 after the etching process. From the cross sectional images shown as insets in (c) and (d), it was observed that the height of the walls is reduced from 1.2 μm to 600 nm after the treatment. The histograms representing the nanowall tip width estimations are shown in (c) and (d) and it was observed that the peak width increases from $\approx$ 15 nm to $\approx$ 40 nm after the KOH treatment.
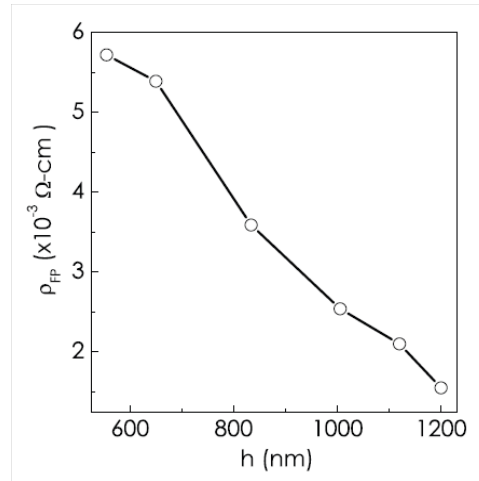
Figure 5.5: Variation of the four-probe resistivity ρ_{FP} of a square piece of the sample as a function of the wall height.

Resistance of sample E was calculated at different intervals during etching using the four-probe method and the ρ_{FP} values are plotted as a function of the wall height h in Figure 5.5. It was observed that ρ_{FP} increases as the wall height decreases through the 50 minutes of etching, implying that the top part of the walls is more conductive than the bottom part. This may indicate that the bottom part of the structure mimics the properties of an epilayer and is more defective than the top portion. Another reasonable assumption is that upon etching away the walls, regions of discontinuity emerge which may contribute to the increased resistivity of the system. However, since the conductivity does not rise by orders of magnitude, the most possible explanation remains that the top part of the nanowall is more conducting than the bottom layer.

Closer examination of the change of resistance revealed the existence of two clearly separate slopes in the resistance data. Figure 5.6 shows the variation of resistance (R) between two xed contact pads as a function of etching time for sample E. It can be observed that the rate of increase of R was initially at a slow rate [only 1.7 Ω/min] up to $\approx$ 14 min of etching time, beyond which it shows a rapid increase at a rate of 20 Ω/min.
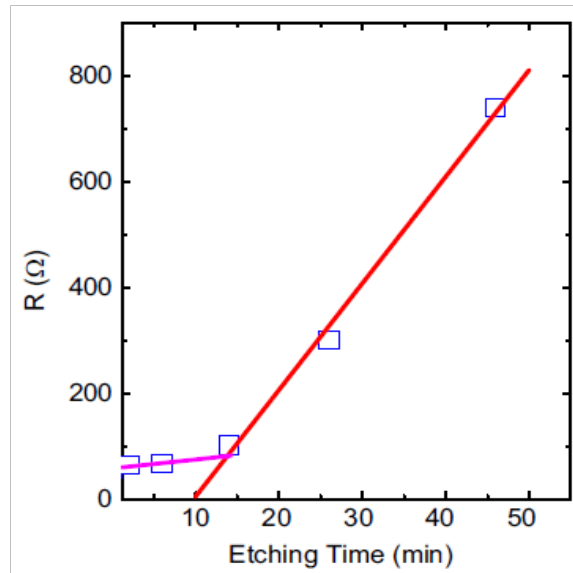
Figure 5.6: The variation of resistance (R) between two fixed contact pads as a function of etching time for sample E.

The rst regime of increase of R can be attributed to the etching of the tip of the nanowalls since the SEM images show that the etching affects the top portion first. Lower density of defects in the tip portion could be the possible reason behind its slower etching rate. Increase of R with the reduction of wall height implies that the conductivity decreases towards the bottom of the walls.
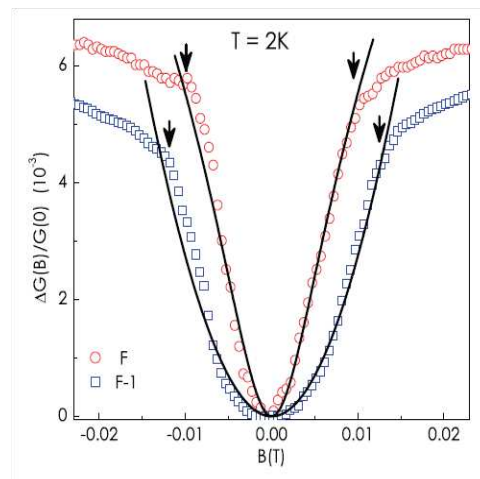
Figure 5.7: Compares the $\Delta G(B)/G(0)$ profiles recorded at 2 K for sample E before and after etching. Solid lines show the fitting of the data using equations (2) and (3) respectively.

Magnetoresistance measurements were carried out for sample E at 2K before and after etching, and are plotted in Figure 5.7. The $\Delta G(B)/G(0)$ profiles show the WL effect in both cases, though $\Delta G(B)/G(0)$ changes more rapidly for the unetched sample than

that for the etched one. In fact, the rapidity at which $\Delta G(B)/G(0)$ changes is found to decrease as the duration of etching increases. This observation is in accordance with that of Figure 5.6, noting that t_{av} has been found to increase with etching time.

Sample D and E-1 belong to the dirty metal regime [$l_e \ll w$], where τ_B is given as $\tau_B = 4hslash^2/w^2e^2B^2D$ [196]. Here, D is the diffusion coefficient, which is given for a thin film with diffuse boundary scattering as $D = \frac{1}{3}v_f l_e [1 - \frac{3l_e}{2w}\int_0^1 s(1-s^2)(1-\exp(-w/sl_e)ds)]$ [197,198]. Difference in conductance $\Delta G(B) = G(B)$ $G(0)$ for $l_e \gg w$ can now be expressed as

$$\Delta G^{wl}(B) = -N_{ch}\frac{e^2}{2\pi^2\hbar}[ln\{(\frac{l_e}{v_f\tau_\phi} + \frac{l_e w^3 e^2 B^2}{C_1\hbar^2})^{-1} + 1\} - ln\{(\frac{l_e}{v_f\tau_\phi})^{-1} + 1\}] \qquad (5.2)$$

and for $l_e \ll w$ (dirty metal regime) as

$$\Delta G^{wl}(B) = -N_{ch}\frac{e^2}{2\pi^2\hbar}[ln\{(\frac{l_e}{v_f\tau_\phi} + \frac{l_e w^2 e^2 DB^2}{4v_f\hbar^2})^{-1} + 1\} - ln\{(\frac{l_e}{v_f\tau_\phi})^{-1} + 1\}] \qquad (5.3)$$

Experimental data of $\Delta G(B)$ are fitted using Figure 5.1.1 for samples B, C, E and Figure 5.1.1 for sample D and E-1 with N_{ch}, τ_{phi} and l_e as fitting parameters. Here, the boundary scattering is considered to be diffusive, meaning the value of C_1 is taken to be 16, w is considered to be equal to t_{av}. Results of the fitting for different samples are shown in Figure 5.2 and Figure 5.7. Electron mobility $\mu_{MR}(2K)$ is estimated from l_e and v_f through $\mu_{MR}(2K) = (el_e/v_f m^*)$ $with$ $m^* = 0.2m_e$ being the electron effective mass for GaN. Note that these mobility values are quite comparable with the values estimated previously from room temperature conductivity data for these samples [182,194]. Moreover, $\mu_{MR}(2K)$ increases as t_{av} decreases, which is again in agreement with our previous observation [182,194]. The phase coherence length l_ϕ is also estimated following the relation $l_\phi = \sqrt{\tau_\phi D}$. Evidently, l_ϕ also increases as t_{av} decreases. Note that for small values of t_{av}, l_ϕ becomes as long as 60 μm. It should be mentioned that larger the value of l_ϕ faster will be the variation of $\Delta G(B)$ with B around B $= 0$. $\Delta G(B)/G(0)$ profiles

shown in Figure 5.2 and Figure 5.7 suggest an increase of l_ϕ with the reduction of t_{av}.
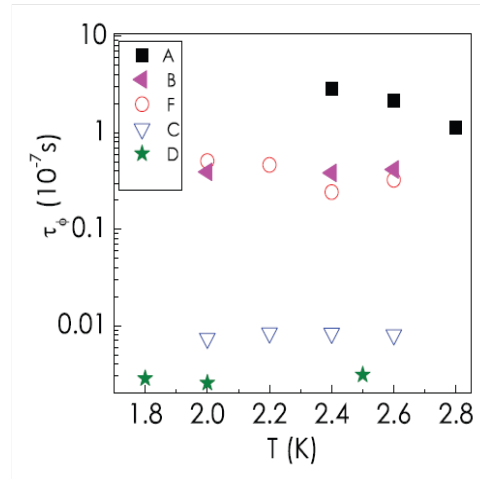
Figure 5.8: Compares the variation of phase coherence time (τ_ϕ) as a function of temperature for different samples.

The variation of phase coherence time (τ_ϕ) as a function of temperature was compared for different samples and is plotted in Figure 5.8. It is evident that τ_ϕ does not vary much with temperature within 23 K range for all samples. This is also clear from almost temperature independent nature of the shape of $\Delta G(B)/G(0)$ profiles around $B = 0$ for sample A within that temperature range as shown in Figure 5.2. Note that in semiconductors, the major source of dephasing is believed to be the electron-electron scattering, which should result in a monotonic decrease of τ_ϕ with increasing temperature. It should be mentioned that temperature independence of τ_ϕ has been reported in other systems such as narrow channels of GaAs/InGaAs heterostructures[199] and GaAs nanowires[200]. The mechanism has been ascribed to certain surface scattering process[201] and also to spinspin scattering by residual magnetic impurities[202]. It is interesting to note that τ_ϕ increases as t_{av} decreases. This could mean that the rate of inelastic scattering, which governs τ_ϕ, increases with t_{av}. Note that mobility is also found to increase with the decrease of t_{av} for these samples.

The photoconductivity (PC) spectra was recorded at room temperature for sample E at different time intervals of etching, and two of the data are shown in Figure 5.9 (a). Spectrum for the reference GaN sample is also shown for comparison. The PC spectrum, which represents the absorption prole[203,204], shows a signicant blue shift (≈ 150 meV) of the band edge for the unetched sample as compared to the typical band gap (3.45 eV) of bulk GaN at 300 K[205]. Interestingly, after 14 min of etching, the spectrum shows a
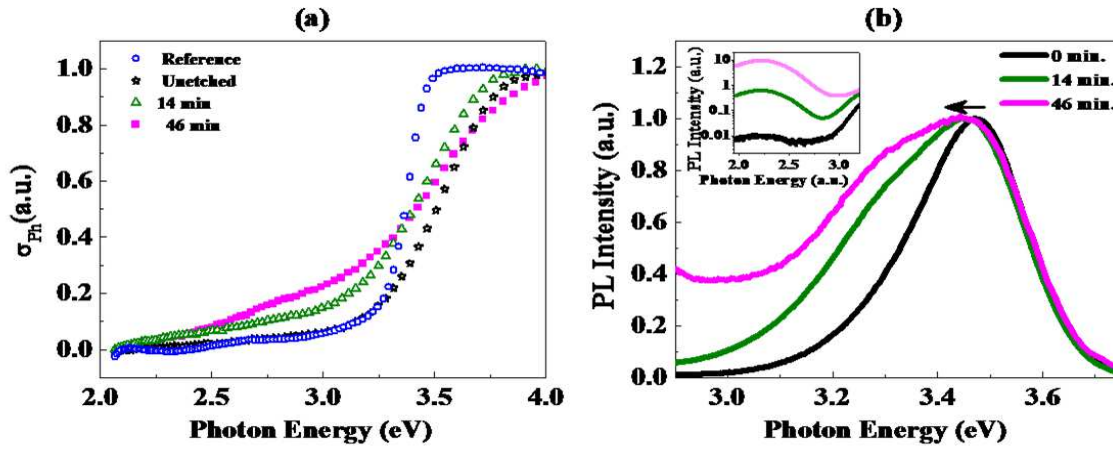
Figure 5.9: (a) compares the photoconductivity (PC) spectra recorded at room temperature for sample S-2 after different steps of etching. Spectrum for the reference GaN sample is also shown for comparison.(b)shows room temperature (300K) normalized PL spectra at the band edge for sample E after various stages of etching. PL spectrum for the reference sample is also shown for comparison.

red-shift. Note that the tips have all but completely removed after 7 minutes of etching. Further etching does not result in any signicant shift of the band gap. However, it has to be noted that the band gap remains to be blue shifted as compared to that of bulk GaN even after 48 min. of etching, when the height of the walls is reduced by more than 1.5 μm. It is also evident from the figure that the rise of the photoconductivity is much slower at the band edge for the nanowall sample as compared to the reference sample, suggesting the existence of a much higher density of tail states in the former. PC proles becomes slower at the band edge as the etching time increases. This shows that the density of defects, which are introducing tail states at the band edge, increases towards the base of the walls.

A complementary PL spectrum was also recorded at each step along with PC and the results are also shown in Figure 5.9 (b) along with a PL of the reference sample for comparison. The near band edge feature for the unetched sample is blue shifted by $\approx$ 85 meV as compared to the reference sample. It is evident that after 14 min of etching the feature shows a red shift. Further etching does not lead to any significant shift of the peak position. This finding is in full agreement with PC results shown in Figure 5.9. It is also noticeable that the band edge feature broadens as the etching duration increases, suggesting an increase in the trap states found at the conduction band minimum towards

the base of the walls.

5.1.2   Potoluminescence Enhancement:

Introduction:

In the previous chapter, it has been shown that GaN in the nanowall network morphology possesses a remarkably higher band edge luminescence compared to other nanostructures and flat films. Due to surface roughening, more light can be extracted from GaN surfaces[206] which is beneficial when fabricating optical emission devices. Hence, it is feasible to exploit the nanowalls for maximum light extraction. The current set of experiments describes two ways via which the photoluminescence from GaN nanowalls has been increased: (1) nitridation of substrate and (2) surface plasmon resonance (SPR) coupling using Ag nanoparticles. Nitridation is known to improve crystal quality[207,208] which affects the band edge luminescence by decreasing the scattering centers formed at the film interface. SPR coupling is a well known method to increase band edge emission (BEE) from semiconductors by coupling them with metal nanoparticles[209][210] which have plasmon resonances in the same frequency range as the BEE of semiconductors.

Experimental Details:

The GaN NWN films are grown in the same conditions as described in the chapter with experimental details. For the nitridation experiment, three films are grown at a substrate temperature of 630 °C. The first sample, S1 is a GaN film grown on bare c-plane sapphire for 2 hours while S2 is grown on a pre-nitrided c-plane sapphire substrate. The nitridation was carried out for 20 minutes at 730 °C via exposure to nitrogen plasma. The third sample S3 is also grown on a pre-nitrided c-sapphire surface, but the growth duration is 4h in this case. The films were characterized by RHEED, FESEM, HRXRD, Raman spectroscopy and PL spectroscopy.

Deposition of Ag was carried out on two GaN nanowall films with varying morphology. Different nanowall structures were obtained by changing the nitrogen plasma flow rate and the Ga k-cell temperature while keeping the other parameters same. For the first sample S1, the N_2 gas flow rate was 6 sccm and the Ga k-cell temperature was 1000

°C; while for the second sample S2 the corresponding values were 4.5 sccm and 1100 °C, respectively. Thin films of 0.6 μm thickness were grown to form wedge shaped nanowalls in both the cases, though the width of the apex of the walls was different. Surface coverage was calculated for both the morphologies using thresholding technique in Gwyddion (ver 2.34) software. Ag was deposited at room temperature using electron beam evaporation in a PVD system (SVT, USA) at a pressure of 2×10^{-6} Torr. A quartz crystal thickness monitor was utilized to estimate the amount of Ag deposited and the thickness in both the cases was 13 nm. The thickness was also confirmed with SEM images which showed a layer thickness of $\approx$ 20 nm which is within the expected error bar generated by limitations of image resolutions. Annealing of the samples was carried out in a tube furnace in a nitrogen environment to prevent oxidation. Prior to annealing, the furnace was purged with N_2 gas for 20 minutes to evacuate air. The ramp rate of the furnace was 20 °C per minute and the duration of annealing in each case was 1 hour. For both the samples, annealing was carried out at 200 °C and 500 °C. The morphology of the samples was determined by FESEM while the optical properties were examined by PL.

Finite Difference Time Domain (FDTD) simulations: 2D FDTD simulations (Lumerical Solutions Ltd.) were carried out in order to estimate the electromagnetic field strength around the Ag nanoparticles for both the samples. The simulation region was established using periodic boundary conditions along x- and y- axes and perfectly matched layers along the x-axis. A plane wave polarized light of wavelength range between 400-700 nm was used as the source along the y-axis while the monitor is placed in the z-normal configuration at the center of the nanoparticle group to obtain the maximum signal possible. To get the best resolution while limiting the simulation time, a mesh override region of 3 nm was selected while the simulation time was 2000 fs.

Results:

Figure 5.10 show the RHEED pattern obtained along $<10\bar{1}0>$ direction *in-situ* for clean and pre-nitrided (20 min) c-sapphire substrates, respectively. Figure 5.10 (c) is the RHEED pattern taken along $<2\bar{1}\bar{1}0>$ for a GaN film grown for 4 hours on a pre-nitrided surface (S3), and its morphology was obtained by FESEM and is shown in Figure 5.10 (d). The RHEED in Figure 5.10 (a) shows streaks characteristic of an atomically
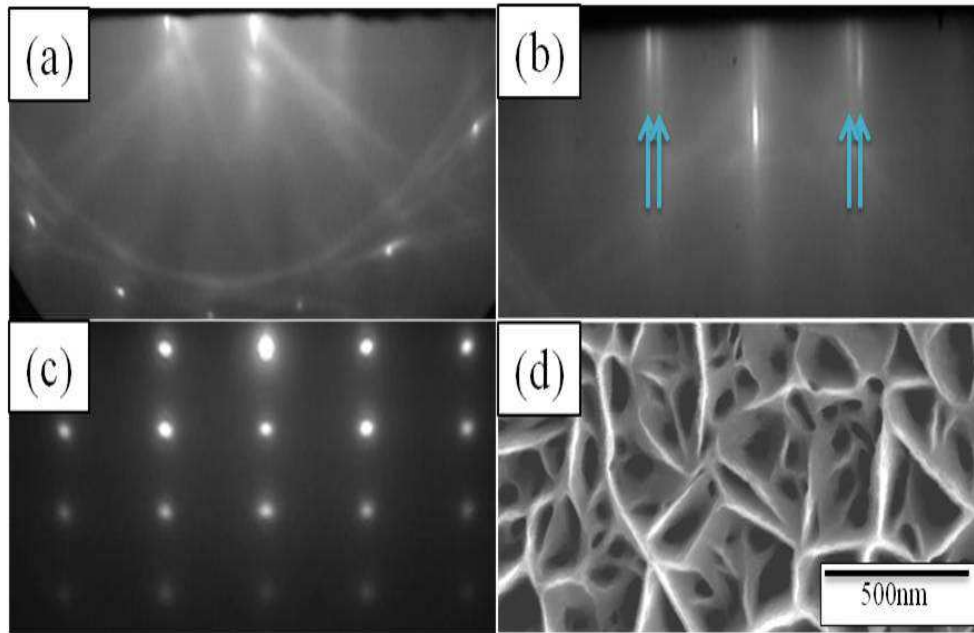
Figure 5.10: RHEED patterns recorded along $<10\bar{1}0>$ direction for (a) clean substrate, (b) post nitridation and along $<11\bar{2}0>$ direction (c) after growth, (d) Representative FESEM micrograph of S3 showing GaN nanowall network homogenously formed over the substrate

clean, uncontaminated, single crystalline c-sapphire with Kikuchi lines signifying the same being visible. In Figure 5.10 (b), two proximal parallel streaks with varying brightness are seen which indicate two separate lattice parameters. The ratio of distance between the streaks reveals that an AlN layer forms with a 30° in-plane rotation of its lattice with respect to Al_2O_3[211]. Since the estimated thickness of the AlN layer formed is $\approx$10 Å[207] for a 20-minute duration of nitridation and the grazing 10 keV electrons have a penetration depth $\approx$20 Å, we observe RHEED streaks pertaining to both AlN layer and the Al_2O_3 substrate. The epitaxial relationship between Al_2O_3 and AlN is established to be $[10\bar{1}0]_{AlN} \,||\, [11\bar{2}0]_{Al_2O_3}$[207]. Figure 5.10 (c) shows a sharp and spotty RHEED pattern of S3 due to the transmission of electrons through the 3-dimensional morphology of the GaN nanostructures. Similar patterns are obtained for S1 and S2 with c/a ratio of 1.63, characteristic of single phase wurtzite GaN. Figure 5.10 (d) is the plan view FESEM micrograph of sample S3, showing GaN NWN forming homogenously on the surface.

Figure 5.11 (a) shows the symmetric 2θ-ω scans for the three films. The plot shows two peaks belonging to (0002) and (0004) planes of wurtzite GaN, along with the (0006) reflection of the Al_2O_3 substrate. The GaN (0002) plane reflections from samples S1, S2
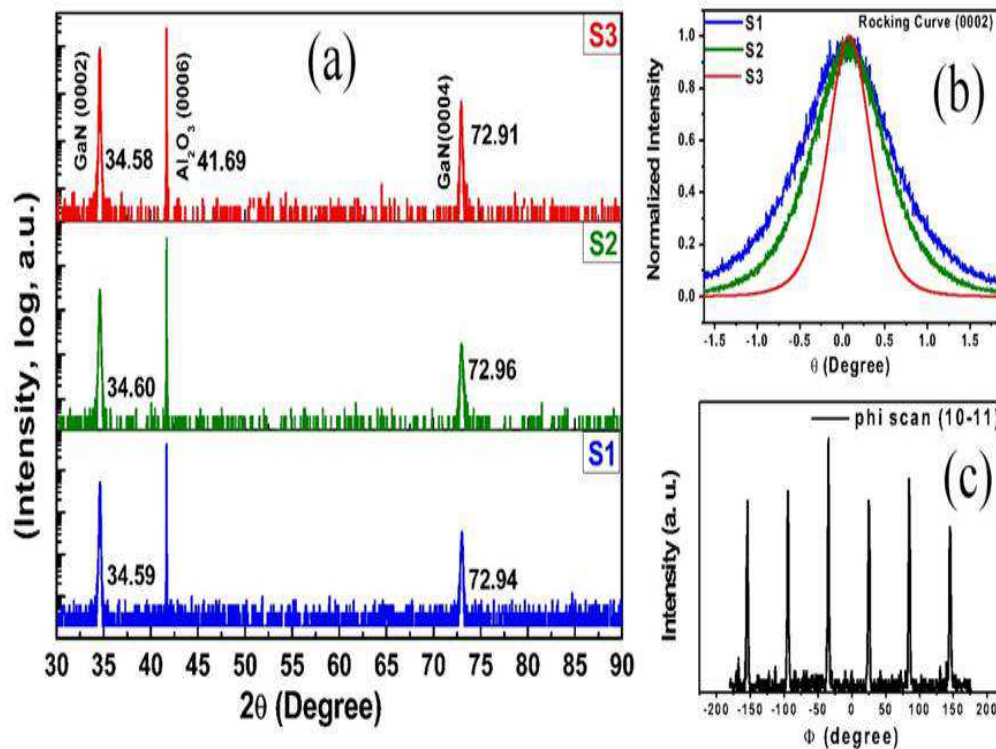
Figure 5.11: (a) 2θ-ω XRD scans with (b) rocking curves taken along (0002) direction for all films superimposed and (c) ϕ scan taken along $<10\bar{1}1>$ showing six-fold symmetry

and S3 are observed at 34.58°, 34.60° and 34.59°; while (0004) plane reflections are at 72.91°, 72.96° and 72.94°, respectively. The absence of any other reflections confirms that the samples are single phased, epitaxial and c-oriented. Rocking curves are obtained for the (0002) reflection, and are shown in Figure 5.11 (b) for the three films with normalized intensity. The GaN film grown for 2 hours on bare c-sapphire shows a high FWHM of 79.8 arc min, while that grown for the same duration on the nitrided surface showed a lower value of 65.4 arc min. After growing for 4h, the FWHM value decreases to 36.1 arc min, showing that the crystal quality of the films increases with growth time. ϕ-scan (Figure 5.11 (c)) measurements performed along $(10\bar{1}1)$ show six peaks at equal angles (60°) from each other which ascertain the six-fold symmetry orientation of the wurtzite structure of the nanowalls. Asymmetric 2θ-ω scans on the $(10\bar{1}5)$ off-axis plane (not shown here) yield a-lattice parameter values using Bragg's law. Stress and strain values are calculated with reference to the bulk lattice parameters of GaN (c = 5.1886 Å, a = 3.1891 Å) obtained from Powder X-ray Diffraction (PXRD) measurements on stress

Sample	Lattice parameter		Strain (x10^{-4})		Stress (GPa)		ν	σ_{XRD}^c	σ_{XRD}^a	σ_{Raman}^c
	c(Å)	a(Å)	ε_{zz}	ε_{xx}	Hydrostatic	Biaxial				
S1	5.1854	3.1926	-6.17	10.9	0.00036	0.28	0.22	-0.56	0.99	0.15
S2	5.1820	3.1889	-12.7	-0.63	0.59	0.14	0.95	-0.27	-0.01	-0.47
S3	5.1836	3.1860	-9.64	-9.41	46.4	0.72	0.51	-0.38	-0.37	-0.32

Table 5.1: Strain and stress values obtained from HRXRD and Raman

free GaN powder sample. Table 5.1 shows the lattice parameters "c" (obtained from the (0004) reflection positions) and "a" along with the corresponding strain values (ε_{zz} and ε_{xx}). Poisson's ratio is then calculated using the relation $\frac{\varepsilon_{zz}}{\varepsilon_{xx}} = -\left(\frac{2\nu}{1-\nu}\right)$ and stress (σ) is determined using Hooke's law; $\sigma_{ii} = \varepsilon_{ii}\left(\frac{E}{\nu}\right)$, where $i = z$ for out of plane and x for in plane stress and E = Young's modulus (200 GPa).

The Poisson's ratio is 0.23 for S1, similar to GaN nanowires[138] where it is attributed to a complex state involving combination of hydrostatic and tensile strains. Generally 2D films of GaN grown on bare c-sapphire have a compressive biaxial strain ($\varepsilon_{xx} < 0$ and $\varepsilon_{zz} > 0$). However, here the out-of-plane strain is observed to be compressive for all the samples, while the in-plane strain is tensile for S1 and compressive for S2 and S3. Separation of the biaxial and hydrostatic components of strain requires the solution of the stress tensor in terms of in-plane and out-of-plane strains. We use the form of the strain tensor utilizing the isotropic constants, which are known within moderate errors ($\approx 10\%$)[164] and the resulting values are shown in Table 5.1

$$\varepsilon_{ij} = \frac{1}{E}\left[\sigma_{ij} - \nu(\sigma_{kk}\delta_{ij} - \sigma_{ij})\right] \tag{5.4}$$

where δ_{ij} = Kröneckers delta function

Our films show a significant component of internal hydrostatic tensile stress in addition to the biaxial compressive stress[138]. Surface relaxation leading to internal strain has been suggested for stiffening of nanoparticles[212] which is a mechanism pertaining especially to nanostructures and may be the most suitable explanation for the dual strain state in our films. The hydrostatic component of the strain steadily increases in the direction S1<S2<S3, but the biaxial stress initially decreases from S1 to S2 before increasing slightly in S3. In nanostructures, since the hydrostatic component is known to stem from an internal strain due to surface relaxation, its increase suggests that our films are getting

increasingly surface relaxed.
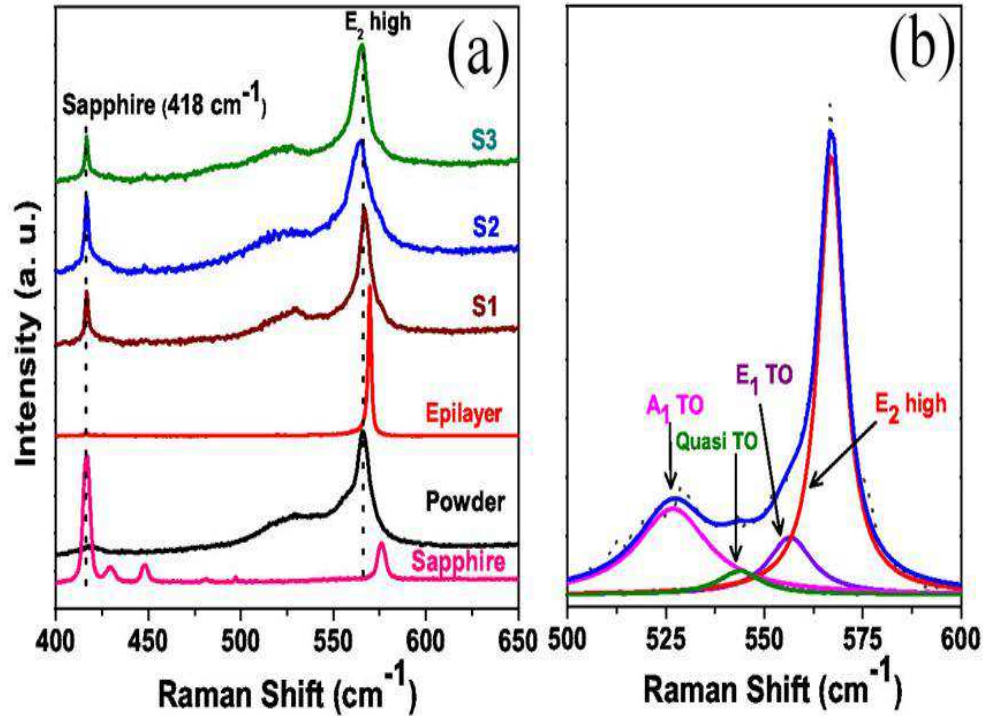
Figure 5.12: Raman spectra for all films taken along with epilayer, sapphire and powder GaN. E_2 high mode peak of S3 is resolved into various components

In order to further investigate the stress behaviour, Raman spectroscopy is carried out on our samples. Raman spectra shown in Figure 5.12 (a) are acquired in the backscattering geometry for the three nanostructured samples, a sapphire sample, a 2 μm thick GaN epilayer and a stress free GaN powder (reference). In this geometry, A_1(LO), E_2(high) and E_2(low) modes are Raman active. The E_2 high mode peak appearing at $\approx$570 cm^{-1} for all the samples manifests the vibration of the lighter N atoms of GaN and is sensitive to in-plane stress in the films[213]. In the figure, the epilayer shows only the E_2 high mode peak while for S1, S2 and S3 samples, an additional substrate related peak at 418 cm^{-1} and a broad band at $\approx$525 cm^{-1} are evident. The asymmetry and broadening of the E_2 high peak can be attributed to the confinement of phonons in the nanostructures[214] which leads to an uncertainty in the wavevector of the phonons causing a downshift and broadening of the Raman spectral lines. This is a well known behaviour of phonons in nanometric systems and is theorized in the phonon confinement model. The deconvoluted Raman features in the 485 to 590 cm^{-1} wavenumber range of S3 are

shown in Figure 5.12 (b). We observe, apart from the strong E_2 high mode, the presence of symmetry forbidden $A_1(TO)$ and $E_1(TO)$ modes at 526.78 cm^{-1} and 556.60 cm,$^{-1}$ respectively. These forbidden modes reported earlier in GaN nanowires were attributed either to a crystal lattice disorder or a deviation from true backscattering geometry[215,216] due to sidewall scattering[164]. For nanoporous materials, these forbidden modes have been observed[122] and are attributed to sidewall scattering in voids whose sizes are smaller than the incident wavelength. In our samples, since the void sizes (100-200 nm) are much lower than the wavelength of the incident light (514 nm), the forbidden TO modes appear to be excited. Another small, but broad peak at 543.81 cm^{-1} can be attributed to a quasi-TO mode which arises out of an intermixing of the A_1 and E_1 TO modes[217,218]. In-plane strain of a film is measured using shift in the line position of E_2(high) mode. With reference to the E_2 high mode peak position obtained for GaN powder, we calculate the stress values in our nanowall samples S1, S2 and S3 by using the Kozawa relation[138], ΔE_2 = σ_a x (4.2±0.3) cm^{-1}GPa,$^{-1}$ which are tabulated in Table 5.2.

For S1, the shift is very small ($\approx$0.64 cm^{-1}) in comparison to that for epilayer ($\approx$2.2 cm^{-1}), indicating that S1 is more relaxed. NWN samples grown on nitrided surfaces show peaks shifted by -1.34 and -1.9 cm $^{-1}$ for S3 and S2, respectively, indicating tensile stress. From the Raman stress values, the shift in band edge emission can also be predicted by the equation ΔE_{PL} = 27±2 meV/GPa and is shown in Table 2.

The PL spectra obtained for these samples is shown in Figure 5.13. The epilayer results in a very low band edge emission intensity at 3.4 eV and a very broad and high defect related peak at 2.2 eV. However, all the NWN samples show intense and broad band edge emission and no defect related peaks, as reported earlier[115,175,182]. The intensity ratios measured from the area under the PL peaks for the epilayer and the samples S1, S2 and S3; is 1:9:34:202. Comparing the intensity ratios of S1 and S2, where the only difference is the nitridation of the substrate prior to growth, it can be seen that reduced lattice mismatch enhances the band-edge emission. The shift in PL band edge compared to the bulk value calculated from E_2 high Raman peak position are listed in Table 5.2. The calculated (from Raman) and observed band edge shift match very well for S1 but not for S2 and S3 due to their larger hydrostatic strain component. Thus, the higher hydrostatic strain in these films does not quench photoluminescence and the increased tensile strain
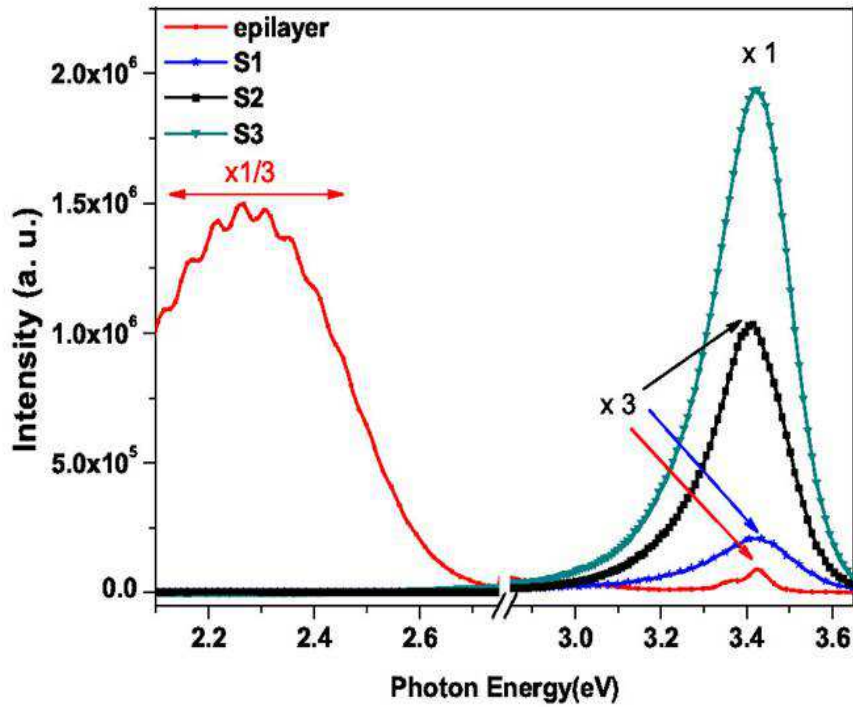
Figure 5.13: PL spectra of all samples plotted in the same graph with absolute intensity

causes blue shift in PL emission.

Sample	E_2 high (cm^{-1})	FWHM (eV)	E_g(PL) (eV)	ΔE_{Raman} (meV)	ΔE_{PL} (meV)
Bulk	566.40		3.420	-	-
Epilayer	568.59	0.04	-	14	-
S1	567.04	0.19	3.424	4.1	4
S2	564.41	0.18	3.417	-12	-3
S3	565.04	0.17	3.426	-8.7	6

Table 5.2: Raman peak shift and band edge peak predicted and compared with PL

Figure 5.14 (a) and (b) are the plan view FESEM images of samples S1 and S2 respectively, showing typical GaN nanowall network structure, with interconnected walls formed on the surface, though the thickness of the walls was different for both the samples. The higher Ga k-cell temperature employed during the growth of S2 increases the gallium flux on the substrate which leads to thickening of the apex of the walls, as also observed by Zhong *et al.*[115]. The reasoning behind this is that in a higher nitrogen rich environment, the Ga adatoms are able to diffuse to only short distances before being nitrided, promoting
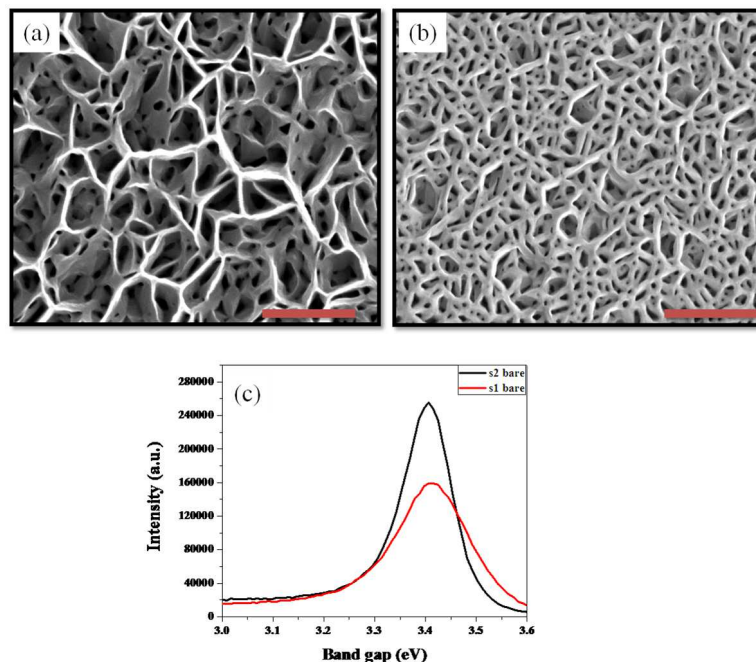
Figure 5.14: (a), (b) FESEM images showing S1 and S2 GaN nanowall network with different morphologies. All scale bars pertain to 500 nm. (c) Photoluminescence spectra of both the samples.

three dimensional growth. Hence, increasing Ga flux leads to an increase in diffusion lengths of Ga adatoms, thereby increasing the width of the nanowalls. Line scans were performed on the FESEM images in order to obtain an estimate of the thickness of the walls. The average thickness of the walls was 40 and 60 nm for S1 and S2, respectively. Although the values are limited by the resolution of FESEM and fitting parameters, they provide a relative comparison between the surface coverage of the two samples. The surface coverage estimation revealed that S1 is 20 % while S2 is 50 %, thereby providing a much more compact structure in S2. PL spectra of both the samples have been plotted in Figure 5.14 14 (c), which shows that S2 has a 20 % higher emission than S1, with a narrower FWHM of 117 meV compared to 164 meV for S1, which is attributed to a large density of band tail states[175,182]. Although nanowall structures show higher emission than flat films, it has been shown by Zhong *et al.* that a nanowall structure which has a sharper apex has a lower PL peak intensity and broader FWHM than the structure with thicker apex[115], which is concomitant with our observations.

Figure 5.15 compiles the plan view FESEM images of all the Ag-deposited samples studied in the present experiment. The as-deposited image of both the samples reveals the difference in the way Ag gets deposited on the surface. Since S1 is relatively more
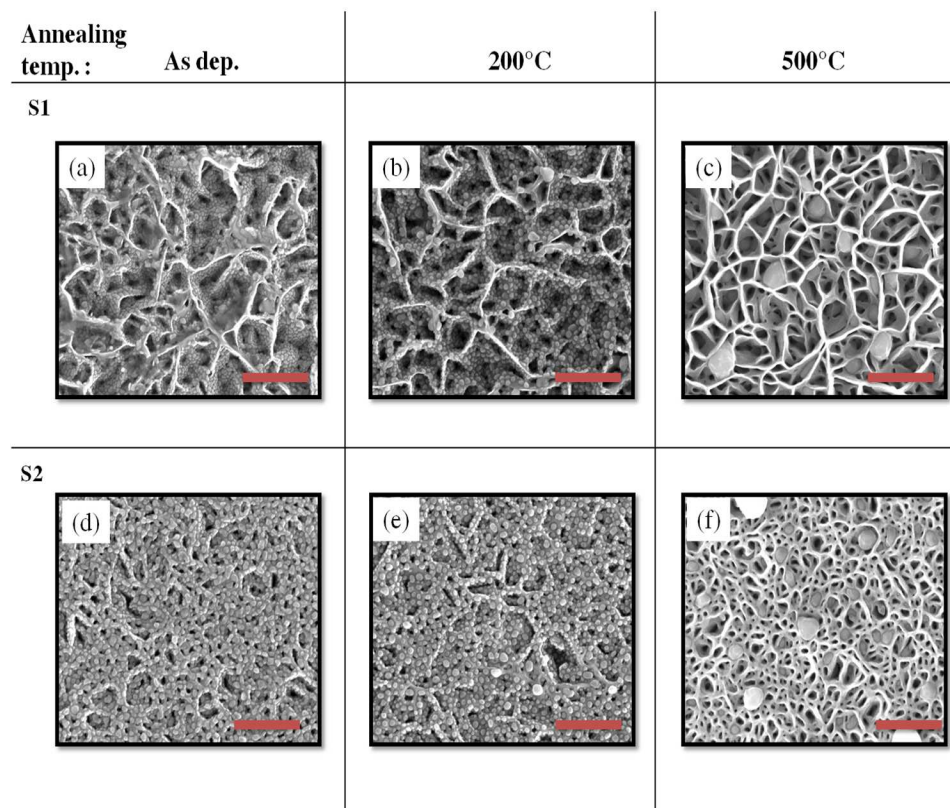
Figure 5.15: FESEM images showing the morphology of all the Ag-deposited and annealed samples studied in this experiment. From (a)-(c): S1 as-deposited, annealed to 200°C, annealed to 500°C; (d)-(f): S2 as-deposited, annealed to 200°C, annealed to 500°C. All scale bars pertain to a length of 500 nm.

porous and the walls are sharper at the apex, most of the Ag is deposited on the sides of the nanowalls. However, due to higher surface coverage of S2 and a thicker apex, most of the Ag is deposited on the flat surface at the top of the walls. In the two samples, the Ag average island sizes are 20 nm for S1 and 30 nm for S2. Annealing the samples to different temperatures results in an increase of the size of the Ag nanoparticles due to thermally assisted diffusion of the Ag and subsequent Ostwald ripening. The size of the particles for the 200 °C annealed sample for S1 and S2 was 30 and 45 nm, respectively. The 500 °C case for both the samples shows that the particles grow to a size where they are trapped in the voids between the nanowalls forming islands with average size 150 nm in both the samples. Many Ag particles become even larger clusters and deposit on the top surface with sizes ≈ 300 nm.

Figure 5.16 shows the PL spectra of S1 and S2 plotted alongside their respective Ag-deposited and annealed samples. The bare and as-deposited samples show similar spectra in both cases, but after annealing to 200 °C, the area under the PL curve increases by
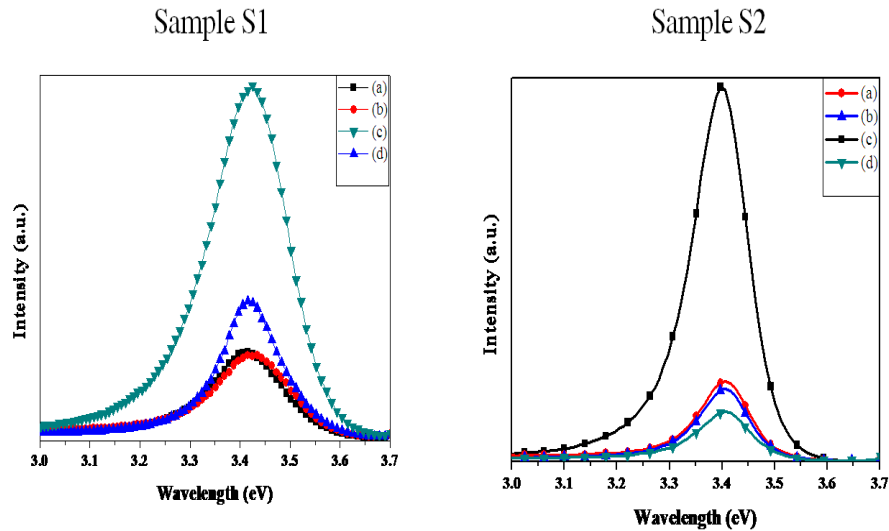
Sample S1   Sample S2

Figure 5.16: Photoluminescence spectra of both the samples with Ag-deposited and annealed spectra plotted simultaneously. For both samples S1 and S2, (a) is the bare sample spectrum, (b) is the spectrum taken after as-deposited condition, (c) is after annealing to 200 °C and (d) is after annealing to 500 °C

5.3 times the as-deposited case for S1 and 5.7 times for S2. Annealing further to 500 °C reduces the PL for both the samples. In case of S1, the area under the curve is now 1.83 times that of as-deposited PL. However, for S2 the area under the curve is only 0.7 times than the as-deposited sample. The FWHM of the band edge emission for S1 and S2 remains almost unchanged, indicating that only the intensity is modulated appreciably as a function of annealing temperature.

Earlier experiments on the concept of enhancing light emission from GaN based structures using Ag surface plasmons involved coating thin metal layers onto quantum well structures, using a spacer layer between the two to prevent complete scattering of emission[210]. Tuning the thickness of spacer layer would then result in maximizing of emission. In metal-semiconductor hybrid systems, primarily two distinct regimes of optical response are observed; enhancement and quenching of the excitonic emission. In the case of enhancement, energy transfer occurs from the excitonic system to the plasmons propagating on the surface of the metal, called as surface plasmon polaritons (SPPs). The coupled energy is then released in the form of photons into free space, leading to a SPP-coupled emission. Another possible route that has been suggested is through localized surface plasmons (LSPs) that absorb and scatter the band edge emission. Quenching occurs when the distance between the metal and the semiconductor reduces to an extent

that the excitonic emission couples to the surface lossy waves, which is a major incentive to incorporate dielectric spacer layers though it may not exploit the full potential of the excitonic emission. Okamoto *et al.* had suggested that in order to have an efficient extraction of light from the SP modes, roughening or nanostructuring of metal is very efficient since it allows the SPs of high momentum to lose the momentum and couple to the radiated emission[210]. In our case, since the material of choice is GaN, which has an emission quite far away from the plasmon emission of Ag, it is possible that metallic reflection of the band edge emission is resulting in an enhancement of the PL. However, since most of the Ag in S2 is deposited on the top surface, it is difficult to imagine multiple reflections occurring at the sides which can lead to enhancement in emission. Hence, the more probable explanation of BEE enhancement remains SPR coupling of GaN with Ag nanoparticles.
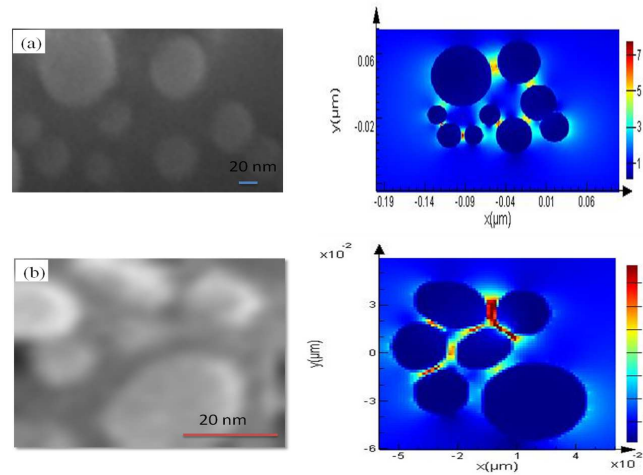
Figure 5.17: Zoomed in FESEM images of the as-deposited configuration of (a) sample 1 and (b) sample 2 with corresponding 2D-FDTD simulations using similar interparticle distances

In order to estimate strength of electromagnetic fields on the surface of the nanoparticle, 2D FDTD simulations have been carried out using the SEM images as a guide for the distribution of Ag nanoparticles on the GaN surface. A representative FDTD calculation done for the as-deposited case is shown in Figure 5.17. A higher electromagnetic field strength around the nanoparticles in S2 in comparison to S1 is observed. For S1, the nanoparticles have an interparticle spacing of around ≈ 50 nm, which gives a much lower electromagnetic field strength compared to S2, where the interparticle spacing reduces to ≈ 10 nm or lower. The corresponding $\mid E \mid^2$ values

for the two samples are 219.49 and 60.53 $(V/m)^2$ respectively. Hence, S2 shows an electromagnetic field 3.6 times stronger than S1. Since in S1 the majority of Ag is deposited on the sidewalls, which are believed to be oriented along m-plane[119], it is evident that nanoparticles when deposited on the top surface (c-plane) exhibit higher field strengths around them.

Inferences:

To summarize, this chapter initially explained the transport properties of GaN NWN which were studied by means of four-probe resistivity measurements, PC and MR. The conductance graph of MR indicated weak localization in the system which was removed at 3.1K. Etching of the nanowalls was carried out to probe the depth dependence of transport properties using KOH solution. Resistivity measurements conducted at various stages of etching suggested that there were two separate regions which got etched at different rates. PC and PL measurements showed that the spectrum begins to show signatures of band tail states which were understood as increasing towards the bottom of the walls. Hence, it was determined that the apex of nanowalls was defect free which led to a slower etching rate while the region of the walls closer to the substrate had higher density of defects.

Next, experiments pertaining to photoluminescence enhancement of the band edge emission of GaN were conducted using two methods, nitridation and SPR coupling with Ag. Nitridation is known to improve crystal quality and it was observed that reducing lattice mismatch not only improved the crystalline quality but also resulted in a two order magnitude increase in band edge emission. Raman measurements showed the presence of symmetry forbidden modes which arise in porous structures due to sidewall scattering resulting in a change in selection rules. The strain states showed a combination of biaxial and hydrostatic and it was seen that Raman based estimation of band gap shift is not accurate in all cases and it is difficult to predict a formula for the same. SPR coupling with Ag nanoparticles is known to increase band edge luminescence for GaN based structures, and it was seen that tuning the size and interparticle distance between Ag nanoparticles indeed resulted in a configuration wherein the BEE enhancement occurs. FDTD simulations showed an electric field intensity of 219.49 and 60.53 $(V/m)2$ between two nearest Ag nanoparticles for S1 and S2 respectively. This further confirmed the

higher photoluminescence enhancement observed in case of S2. The photon output for S2 was calculated to be 5.7 times more at maximum enhancement compared to the bare surface while the corresponding value for S1 was only 5.3 times. It can be deduced that S2 has more intense hot spots which provide higher electric field intensity. The multiple reflections afforded by the nanowall configuration may be more in S1 but the larger distance between the Ag nanoparticles in this case reduces the hot spot intensity.

Chapter 6

SERS studies using Ag-GaN NWN as a template

6.1 Introduction:

In recent times, SERS is emerging as a powerful tool for obtaining ultrasensitive vibrational spectra of molecules[219–222] and has great potential for biomolecular detection. To exploit the full potential of SERS for a variety of applications, a large number of plasmonic substrates have been fabricated. Apart from colloidal substrates in the solution phase, solid SERS substrates have been fabricated by forming clusters or islands of metal nanostructures[223,224] and nanostructured films[225]. Recently, three-dimensional (3D) nanostructures such as porous substrates[226], tips[227], channels[228], wires etc., have been fabricated by employing electron beam lithography[229], electroless deposition[230], nanosphere lithography[231], etc. Although sophisticated nanoscale patterning techniques have enhanced the versatility of this technique, it is limited with issues of lack of reproducibility and reduction in the enhancement factor arising due to several reasons such as inhomogeneous attachments, variable particle distribution, charge selectivity, etc. When colloidal nanoparticles are employed, the capping agent forms a barrier between the nanostructure and the analyte molecule leading to decreased enhancement and unwanted background signal. In addition to reproducibility, a biochemical sensor demands the fabrication of a large surface area substrate with a uniform enhancement

factor. Therefore, a uniformly distributed plasmonic nanostructure on a substrate would be ideal for use as a SERS substrate. Apart from the plasmonic nanostructures, it has been previously observed that the underlying substrate also plays an important role in the SERS enhancing capability[232]. The surface plasmons of the nanomaterials are known to be directly influenced by the physical environment, since the incident electromagnetic field induces charge polarization on the nanoparticles which is affected by that of the substrate and results in a shift in the surface plasmon resonance[233]. Formation of regions of high electric field intensities similar to hotspots between a metal coated nanowire and a dielectric substrate was reported by Glembocki *et al.*[234]. Plasmonic nanostructures on dielectric films have also been observed to induce optical interference based enhancement of SERS[235]. Thus, it is worthwhile to tailor-make SERS substrates of different nanoparticle-dielectric/semiconductor hybrid geometries that can enhance SERS signals.

In this chapter, two SERS experiments are described using Ag-GaN nanowall hybrid structure as a substrate. The first experiment explores the as-formed Ag-GaN structure as a potential template to study the SERS activity of various biomolecules such as Rhodamine 6G (R6G), Thiophenol, Human Serum Albumin (HSA) and Bovine Serum Albumin (BSA). Since in our case, the Ag nanoparticles are not stabilized by any external chemical capping agent, signals are obtained with a high degree of reproducibility and no background noise. The veracity of this novel substrate was tried by SERS experiments conducted on proteins of both positive and negative charges to evaluate the universal nature of the substrate, since it has been difficult to get SERS of all proteins using a single substrate. By finite-difference-time-domain (FDTD) simulations, it was shown that a higher near field intensity exists in the vicinity of the Ag nanoparticles over GaN compared to silicon, and that the nanowall configuration gives higher signal compared to flatter one. The second experiment comprised of examination of SERS response of different biomolecules by varying the porosity of the GaN nanowall structure as well as tuning the interparticle distance, size and nanoparticle distribution of Ag nanoparticles. The Ag-GaN structures were annealed to change the Ag nanoparticle size and distribution. It was observed that lowering the surface porosity leads to higher SERS signals, but higher porosity surfaces give SERS signals even after the annealing is carried out at high

temperatures. This was understood as the difference in the way Ag deposits in both cases. With more compact nanowalls, most of the Ag deposits on the top surface and hence at high temperatures the Ag nanoparticles are too far apart to give SERS enhancement. For thinner nanowalls, the higher porosity allows Ag nanoparticles to deposit on the sidewalls which do not diffuse as much as the ones on the top surface, which makes the template give SERS response even after the structure is annealed to a much higher temperature.

6.2 Experimental Details:

For the first experiment, the GaN nanowall network structure was grown on a c-plane sapphire substrate using molecular beam epitaxy (MBE) system (SVT Assoc.) in nitrogen rich conditions at 630°C substrate temperature. The experimental setup, conditions and growth details are the same as described in the chapter with experimental details. Ag deposition was carried out in the same way as explained in chapter 5. For the SERS studies, the samples were dipped in the biomolecule solution for 10 minutes before the spectra were acquired. The Raman and the SERS spectra were recorded in the 180° backscattering geometry, using a 532 nm excitation from a diode pumped frequency doubled Nd-YAG solid state laser (model GDLM-5015 L, Photop Suwtech Inc.) and a custom-built Raman spectrometer equipped with a SPEX TRIAX 550 monochromator and a liquid nitrogen cooled CCD (Spectrum One with CCD 3000 controller, ISA Jobin Yvon)[236]. Laser power at the sample was ≈ 8 mW, and a typical spectral acquisition time was 30 s.

The second experiment was carried out using two GaN nanowall network films which differed from the first experiment in the N_2 flow rate and Ga k-cell temperature. The first sample, S1, was grown keeping the N_2 gas flow rate at 6 sccm and the Ga source at 1000 °C; while for the second sample S2 the corresponding values were 4.5 sccm and 1100 °C, respectively. Ag deposition was carried out in the same way as described in chapter 5 and annealing was carried out in a tube furnace in a nitrogen environment to prevent oxidation. Prior to annealing, the furnace was purged with N_2 gas for 20 minutes to achieve inert atmosphere which prevent oxidation of Ag. The ramp rate of the furnace was 20 °C per minute and the duration of annealing in each case was 1 hour. For both the

samples, annealing was carried out at 200 °C and 500 °C. Surface coverage was calculated for both the morphologies using thresholding technique in Gwyddion (ver 2.34) software.

Finite-difference time domain (FDTD) simulations:

2D FDTD simulations (Lumerical Solutions Ltd.) were used to determine the near-field intensities around the silver nanoparticles deposited over the GaN substrate. The simulation zone consists of periodic boundary conditions along x-axis and along y-axis, perfectly matched layers (PML) which absorb the waves moving out of the zone and hence preventing the reintroduction of reflections. Electromagnetic field distribution was calculated for silver nano particles with a radius of 10 nm and inter-particle separation of 5 nm, on a GaN layer of thickness 3 m for a planar surface and for a triangular nanowall configuration. A plane wave polarized light of wavelength 532 nm was used along the y-axis. For minimum simulation time and to maximize field enhancement resolution, the mesh override region was set to 0.5 nm, and the overall simulation time was 2000 fs.

6.3   Results:
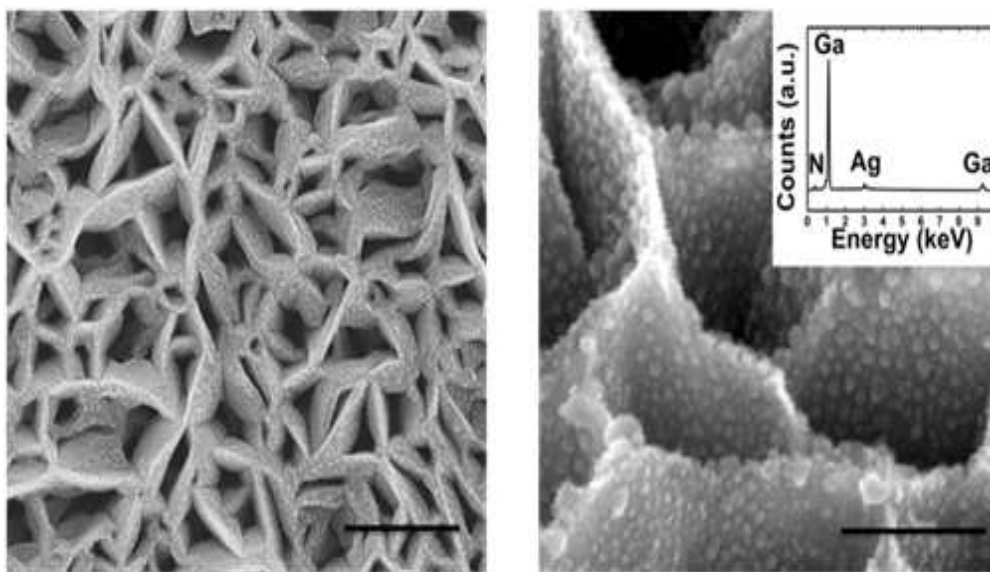
Figure 6.1: FESEM images of the 3D GaN nanowall substrate with silver nanoparticles deposited on them. The average size of the Ag nanoparticles was 20 nm with an average interparticle distance of 5 nm. The scale bars correspond to 500 nm (left) and 100 nm (right). The inset shows the EDS of the substrate to confirm the presence of silver.

Figure 6.1 shows the plan and 45° tilted view of the GaN film grown for the first experiment. Typical GaN nanowall network structure was observed to form

homogenously all over the surface. Though conventionally, flat surfaces have been used to deposit metal nanoparticles for SERS applications, a corrugated dielectric surface can provide two important possibilities: a) nanoparticle-dielectric interaction with very high contact angle, and b) large surface area, with high density of nanoparticles that can result in the enhancement of SERS intensity. Ag deposited on these well structured surfaces is uniformly distributed as spherically shaped Ag nanoparticles of size $\approx$20nm, with an interparticle spacing of $\approx$5nm. The PVD method to grow Ag on GaN nanowalls yields very clean samples, and it is also compatible with MBE growth (can be integrated in one system) and does not use stabilizing surfactants or capping layers. Energy Dispersive X-ray Spectroscopy (EDS) and X-ray Photoelectron Spectroscopy (XPS) was done on the sample to confirm that the particles are made of Ag. To demonstrate the effectiveness of this GaN nanowall-Ag nanoparticle configuration for SERS, we have compared similar experiments performed on commercial GaN epilayer (2 μm flat film), on Al_2O_3 (0001). Ag did not adsorb well on the c-plane GaN thin flat film, and its adherence was weak and patchy (not shown here).
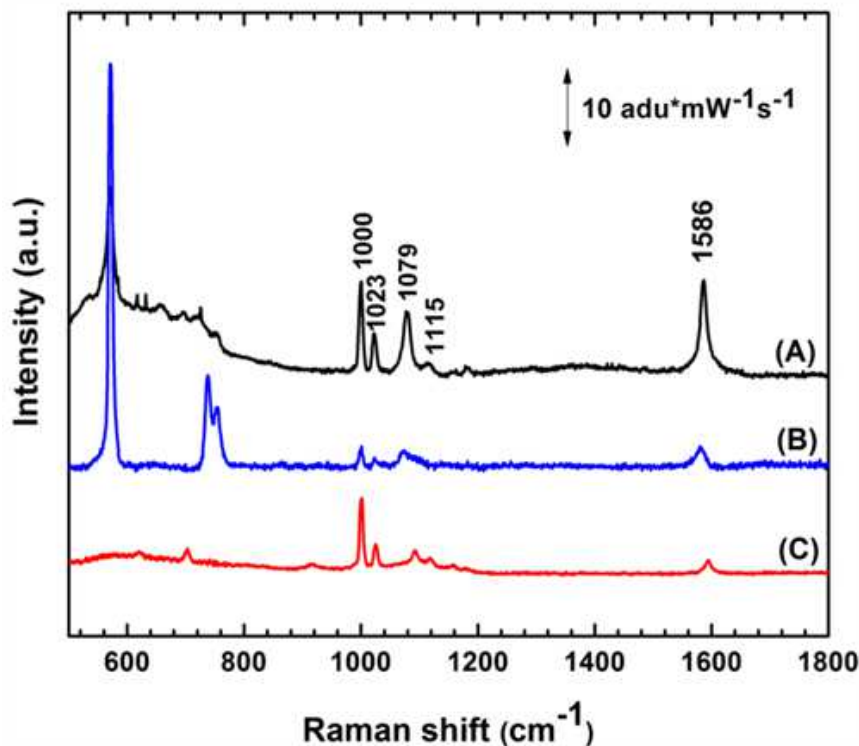
Figure 6.2: SERS spectra of (A) 1 mM thiophenol on the silver nanoparticles coated GaN nanowall substrate, (B) 1 mM thiophenol on the silver deposited GaN epilayer. (C) shows the normal Raman spectra of neat thiophenol using 532 nm wavelength laser. Note that below 800 cm^{-1} Raman spectrum is dominated by GaN related features.

Figure 6.2 shows the SERS enhancement of thiophenol adsorbed on the silver nanoparticles-GaN substrate and a significantly lower signal on the 2D flat epilayer. The SERS enhancement factor (G) was calculated by the method given by Yu *et al.*[237]:

$$G = \frac{I_{SERS}}{I_{NORM}} \frac{N_{BULK}}{N_{SURF}} \tag{6.1}$$

where I_{SERS} and I_{NORM} are the intensities of a specific band in SERS and normal Raman of the analyte molecule, respectively. N_{BULK} and N_{SURF} are the number of probe molecules which are illuminated under the laser beam in bulk and SERS experiments, respectively. N_{SURF} is given by CA, where C and A are the surface densities of thiophenol ($6.8 \times 10^{14} mol cm^{-2}$) and the laser spot area respectively[?]. N_{BULK} is given by Ahρ/m, where h, ρ and m are the penetration depth (100 μm), the density (1.079 g cm^{-3}) and the molecular weight (110.18 g mol^{-1}) of thiophenol respectively. The typical enhancement factor (EF) calculated for this substrate is 10^5. The stable SERS spectra of thiophenol is due to the binding of the thiol group to the silver nanoparticle surface, which corroborates with the frequency of the in-plane breathing mode coupled to the ν(C-S) mode decreases from 1092 to 1069 cm^{-1}[238]. This EF is comparable to the values in earlier reports of Ag nanoparticles on GaN substrates[239]. Since the nanoparticles are separated by a gap of 5 nm, which is much more than that required for creating hotspots of intense electromagnetic field, leading to EF a few orders of magnitude lower than that of other silver nanostructures reported in the literature that were successful in ultratrace detection of small molecules (Raman reporter molecules)[240,?,-242]. This is a trade-off considering that a gap of 5 nm between the nanoparticles is beneficial in obtaining spectra of large molecules like proteins which is demonstrated in this paper. The high SERS sensitive silver nanostructure reported earlier[240,?,-242] have not demonstrated SERS of proteins, because the hotspot regions are much less than sizes of the proteins used here.

The supporting substrate for metallic nanoparticles plays an important role in the surface plasmon resonance (SPR) of the nanoparticles. Charge polarization of the metal-semiconductor/dielectric system under external electromagnetic field affects the SPR of the nanoparticles[233]. The nanoparticle-semiconductor junction might also lead to Schottky barrier formation which is localized and not very large in our case due to

small Ag clusters not covering the surface fully[243]. However, the barrier, if any, is not expected to affect SERS enhancement[244]. The SERS enhancement is explained from the electromagnetic field distribution around the nanoparticles deposited on GaN substrate (shown in Figure 6.3). The Ag deposited GaN nanowall substrate showed highest electric field strength $| E |^2$ which is about 3 times more than that for silver deposited on flat GaN substrate as calculated by FDTD simulation. Larger near-field intensity in case of GaN is observed in comparison to silicon, which shows a maximum field intensity of 1.32 in the vicinity of silver nanoparticles adsorbed on a flat layer. Since the SERS enhancement factor is given by $| E |^4$, its values depend on the near field intensity in the vicinity of the nanoparticles. The near-field intensities are influenced as the incoming electromagnetic field experiences a change in dielectric constant due to the presence of the dielectric or semiconductor substrate, causing a change in the distribution of the electric field in the vicinity of the nanoparticles[233]. The electric field is focused in definite regions between the nanoparticle-dielectric junctions giving rise to active sites for SERS enhancement[234]. In the nanowall configuration the greater field intensity can be attributed to the increased focusing effect of the denser GaN dielectric medium or to the multiple reflections that the incoming radiation suffers inside the cavity surrounded by the nanowalls. The calculations also show that GaN as a substrate has better SERS enhancement than on traditionally used substrates like silicon in both the planar as well as nanowall form. Thus the GaN nanowall/Ag substrate has several advantages over other pristine metal nanoplates that have been grown on semiconductor substrates having high reflectivity[245,246], since it is difficult to maneuver the nanoplates to introduce multiple reflections or to control their orientation and introduce uniform surface distribution.

Another important aspect of the silver nanoparticle decorated GaN substrate is the reproducibility of SERS signals shown in Figure 6.4. SERS spectra obtained from nine different regions of the single substrate of size 2 mm x 2 mm showed good reproducibility with the little fluctuations in the enhancement factors coming from reminiscent thiophenol molecules in the cavities. Conventionally, SERS is marred by the problem of reproducibility since analyte signals show large fluctuations in the enhancement factor due to irregular hot spot distribution. The uniform distribution of the nanoparticles in our experiments leads to uniformity of hotspots resulting in high
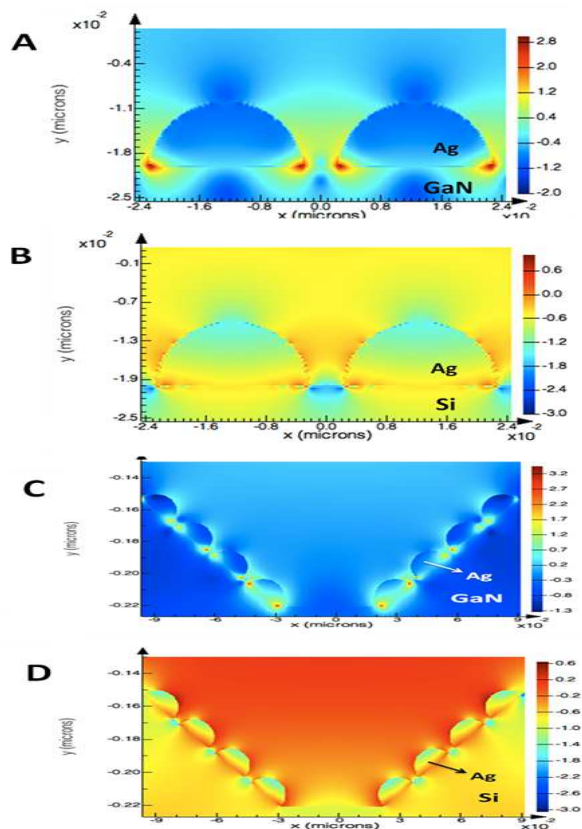
Figure 6.3: E-field amplitude patterns obtained from 2D FDTD calculations at wavelength 532 nm of silver nanoparticles on (A) a flat GaN layer, (B) a flat silicon layer, and (C) a GaN nanowall surface with 200 nm diameter pit and walls with a maximum thickness of 150 nm and (D) a silicon surface with similar morphology as C. The background material was taken as air with n = 1.

reproducibility. Since the enhancement factor depends upon the particle size of the silver nanostructure we have also fabricated different sized nanoparticles by annealing the substrate to 600°C and also by depositing more silver by PVD. In the present study, we chose the substrate with silver nanoparticles of 20 nm in diameter which are uniformly deposited on the GaN substrate, resulting in a uniform SERS enhancement over the entire surface area. This has a major advantage, especially when one tries to pattern the substrate for multiparameter detection. The roughness of the GaN substrate also plays an important role in preventing the *"coffee ring effect"* in which the analyte molecules on drying of the solution are deposited on the particle edge leading to uneven distribution[247]. This also happens in the case of colloidal nanoparticles when they are mixed with the analyte molecules and deposited on a surface to obtain SERS spectra. In the GaN nanowall substrate, the rough surface with hollow cavities prevents the

molecules from escaping to the edges on drying and therefore ensures even distribution. This has been demonstrated with the much mobile and small molecule thiophenol which shows uniform reproducibility in SERS spectra. The differential reflectivity due to the nonuniform nanoparticle aggregates also leads to nonuniform optical reflectivity causing irreproducible SERS[248]. Since the nanoparticles are firmly supported by the GaN substrate, there is no analyte induced aggregation taking place, and therefore the reproducibility of the substrate is maintained.
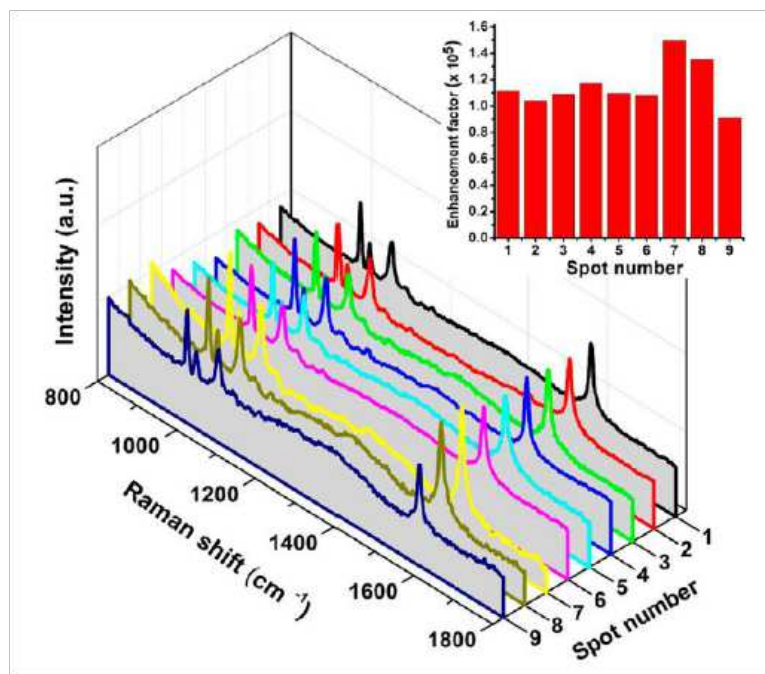
Figure 6.4: SERS spectra of 1 mM thiophenol on randomly selected nine spots of the silver deposited GaN nanowall substrate, demonstrating signal uniformity and reproducibility.

SERS is emerging as a powerful tool in bioanalysis as it provides information about the secondary structure of protein and can detect protein drug interactions[249–251]. In the past, SERS of biologically important proteins like Coactivator-Associated Arginine Methyltransferase and Human transcriptional co-activator p300[252,253] have been carried out. Protein-small molecule interactions were also investigated to understand the effect of inhibitors and activators of the proteins[254,255]. It should be noted that attachment of different proteins to SERS active substrates has always been challenging since the capping agent stabilizing the nanoparticle poses as a barrier for the protein to directly attach to the nanoparticle surface (e.g. PCAF, which is also a transcriptional co-activator like p300 failed to give SERS signal). Therefore, one of the most difficult aspects of using SERS in

proteins is that most of the substrates are selective to a particular type of protein only. Obtaining good and reproducible SERS spectra of proteins is most difficult among all other biomolecules. The diverse surface groups, properties, different shapes and sizes, and different manner of interaction with the nanostructure surface make the development of a universal substrate very difficult for proteins[256]. In view of this, developing a versatile SERS substrate for studying proteins of different charges is important and will have a strong impact in the field of drug development. Proteins are constituted by the zwitter-ionic amino acids, which are connected by peptide bonds, and therefore based on the composition; it may have a net charge, positive, negative or be charge neutral. In order to demonstrate the universality of the SERS substrate, we have shown here the SERS spectra of two oppositely charged proteins, lysozyme (pI of 11 in neutral pH) and human serum albumin (HSA with pI of 5.5) (Figure 6.5) obtained on the Ag NP/GaN substrates. Both of these proteins are bigger molecules with diameters of a few nanometers (HSA molecule in solution is an ellipsoid of around 11 nm in length[257]). Therefore protein molecules lying away from the hotspot might not give good SERS signals and can lead to background fluorescence. The average of 5 nm gaps between the nanoparticles allows the protein to settle between the hotspots and give reasonable SERS enhancement for sensing purposes. Proteins interact with nanostructures using adsorption with or without electrostatic attraction or form covalent bonds through cysteine-like moieties.

In the present case, the analyte is purely adsorbed on the Ag nanoparticles. In our earlier studies on P30042 and CARM143 proteins we have demonstrated that the protein activity is retained even in the presence of silver nanoparticles, hence the protein structures do not undergo large scale changes. The observed bands can be assigned to the proteins based on those reported in the literature[258,259]. It should be noted that many of the bands of the SERS spectra of proteins differ on changing the nature of the nanostructure, as the orientation and attachment region of the protein to the nanostructure change. The spectra of the proteins are dominated by the amide bands which provide information about the secondary structure of the protein and the bands corresponding to the aromatic amino acids. The spectra also contain modes corresponding to backbone chain vibrations. In the case of lysozyme the amide II and III modes can be seen at 1540 cm^{-1} and 1261 cm^{-1}, respectively, while the prominent amide
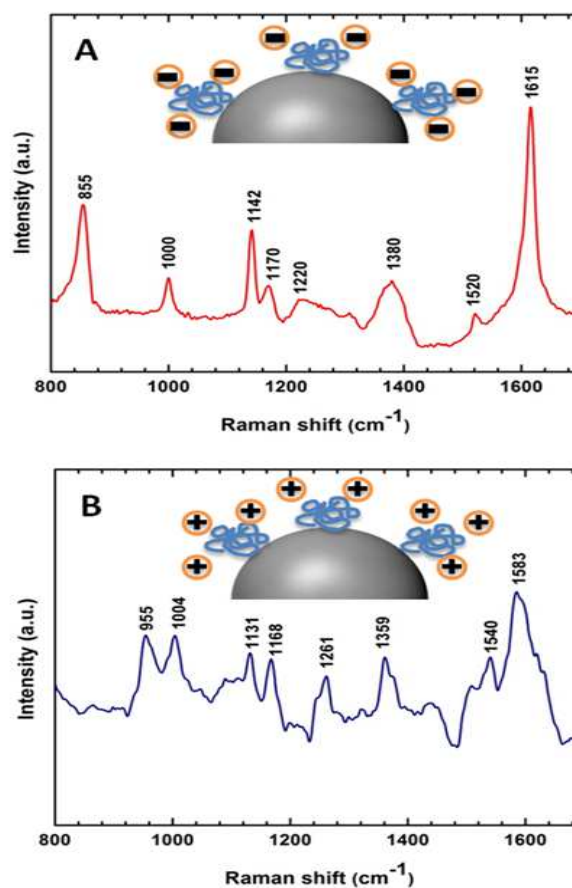
Figure 6.5: SERS spectra of proteins (A) 10^{-5} M Human Serum Albumin and (B) 10^{-5} M lysozyme, demonstrating charge independent detectability of the substrate

I band is either absent or dominated by bands from other aromatic amino acids. The bands at 887, 1004, 1359, and 1583 correspond to aromatic amino acids like phenylalanine, tyrosine, and tryptophan. In HSA, the amide I, II, and III bands can be seen at 1615, 1520, and 1220 cm^{-1}, while the aromatic amino acid bands lie at 855 and 1000, respectively. Some of the aromatic amino acid bands overlap with the amide bands of the proteins. In most cases, proteins have a set of SERS bands which are distinct from each other as shown in the spectra of lysozyme and HSA. This presents a proof of principle that proteins can be differentiated and can be detected by SERS using similar sample preparation techniques for differently charged proteins and with limited knowledge about the nature of the proteins using the GaN nanowall based plasmonic substrate.

Figure 6.6 (a) and (b) are the plan view FESEM images of samples S1 and S2 respectively grown as part of the second SERS experiment. Typical GaN nanowall
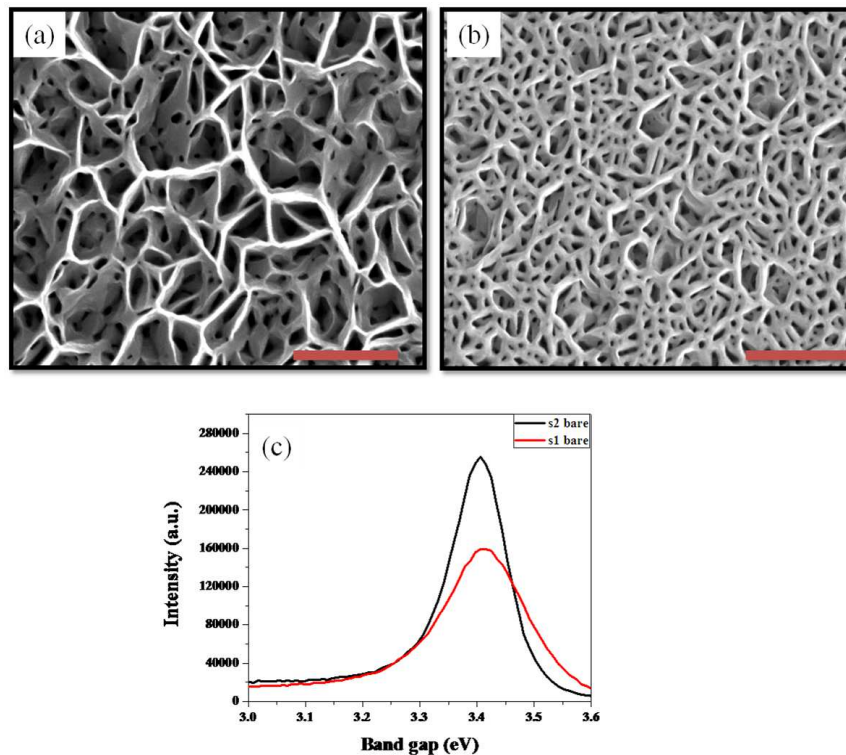
Figure 6.6: (a), (b) FESEM images showing S1 and S2 GaN nanowall network with different morphologies. All scale bars pertain to 500 nm. (c) Photoluminescence spectra of both the samples.

network structure is observed with interconnected walls formed on the surface, though the thickness of the walls was different for both the samples. The higher Ga k-cell temperature employed during the growth of S2 increases the gallium flux on the substrate which leads to thickening of the apex of the walls, as also observed by Zhong *et al.*[115]. The reasoning behind this is that in a higher nitrogen rich environment, the Ga adatoms are able to diffuse to only short distances before being nitrided, promoting three dimensional growth. Hence, increasing Ga flux leads to an increase in diffusion lengths of Ga adatoms, thereby increasing the width of the nanowalls. Line scans were performed on the FESEM images in order to obtain an estimate of the thickness of the walls. The average thickness of the walls was 40 and 60 nm for S1 and S2, respectively. Although the values are limited by the resolution of FESEM and fitting parameters, they provide a relative comparison between the surface coverage of the two samples. The surface coverage estimation revealed that S1 is 20 % while S2 is 50 %, thereby providing a much more compact structure in S2. PL spectra of both the samples have been plotted in Figure 6.6 (c), which shows that S2 has a 20 % higher emission than S1, with a narrower FWHM of 117 meV compared to

164 meV for S1, which is attributed to a large density of band tail states[182][?] . Although nanowall structures show higher emission than flat films, it has been shown by Zhong *et al.* that a nanowall structure which has a sharper apex has a lower PL peak intensity and broader FWHM than the structure with thicker apex[115], which is concomitant with our observations.
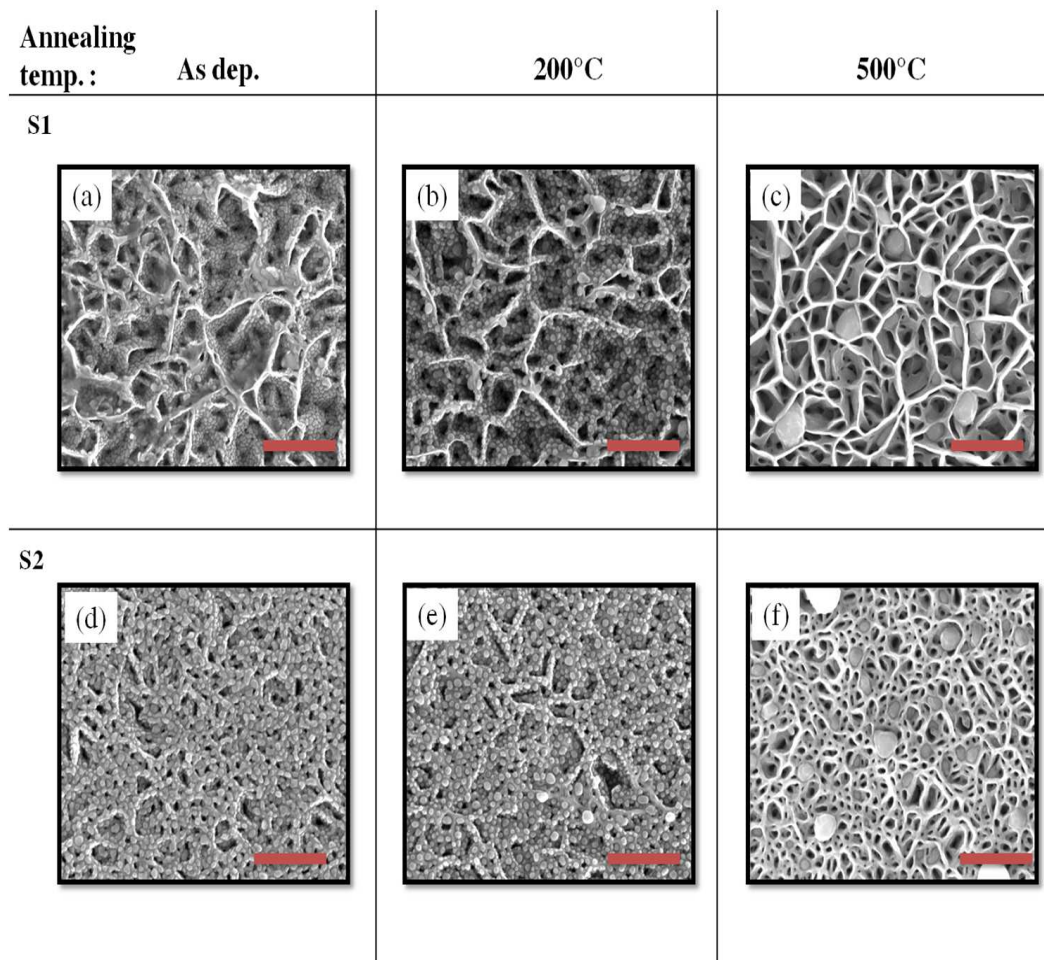
Figure 6.7: FESEM images showing the morphology of all the Ag-deposited and annealed samples studied in this experiment. From (a)-(c): S1 as-deposited, annealed to 200°C, annealed to 500°C; (d)-(f): S2 as-deposited, annealed to 200°C, annealed to 500°C. All scale bars pertain to a length of 500 nm.

Figure 6.7 compiles the plan view FESEM images of all the Ag-deposited and annealed samples studied in the present experiment. The Ag as-deposited image of both the samples reveals the difference in the way that Ag gets deposited on the surface. Since S1 is relatively more porous and the walls are sharper at the apex, most of the Ag is deposited on the sides of the nanowalls. However, due to higher surface coverage of S2 and a thicker apex, most of the Ag is deposited on the flat surface at the top of the

walls. In both the cases, the Ag average island sizes are 20 nm for S1 and 30 nm for S2. Annealing the samples to different temperatures results in an increase of the size of the Ag nanoparticles due to thermally assisted diffusion of the Ag and subsequent Ostwald ripening. The size of the particles for the 200 °C annealed sample for S1 and S2 was 30 and 45 nm, respectively. The 500 °C case for both the samples shows that the particles grow to a size where they are trapped in the voids between the nanowalls forming islands with average size 150 nm in both the samples. Since the voids are of different dimensions there is a distribution of large Ag island sizes from 70-300 nm.
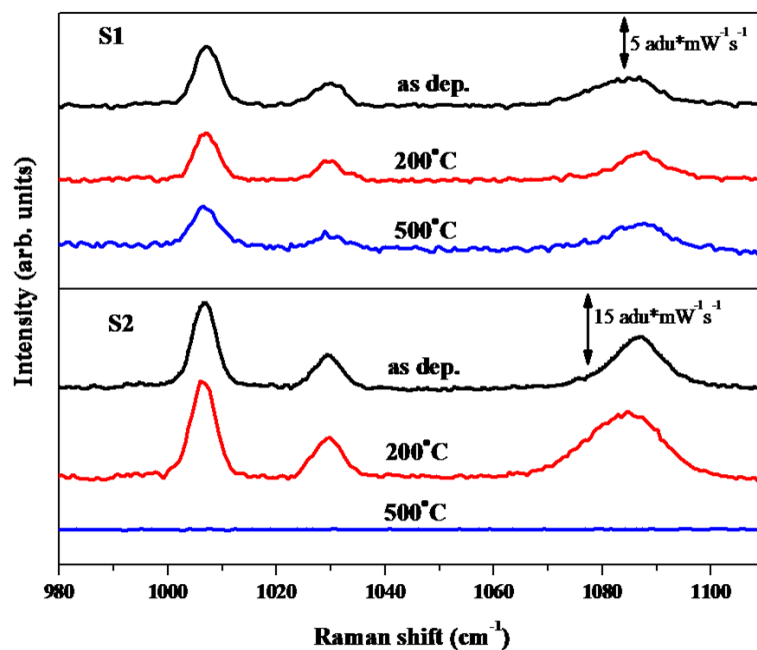
Figure 6.8: SERS spectra of all the samples acquired using thiophenol as analyte

After studying the application of GaN NWN as a SERS active substrate[158], we have carried out SERS on all the samples using thiophenol as the analyte. Figure 6.8 shows the SERS enhancement spectra of thiophenol for all the samples in the case of both S1 and S2. It is observed that S2 gave a higher SERS enhancement compared to S1 in the as deposited and 200 °C annealed samples. In the case of 500 °C annealed sample, there was no detectable signal for S2 though S1 still showed some peaks. S1 also shows a reduction in SERS enhancement with annealing of the sample while S2 showed an increase when the sample was annealed to 200°C. Since the nanoparticles are at their closest in the as deposited configuration for both the samples, the SERS enhancement

Sample name	Enhancement factor
Sample 1 as deposited	9.97×10^4
Sample 1 200°C	9.57×10^4
Sample 1 500°C	1.06×10^5
Sample 2 as deposited	4.73×10^5
Sample 2 200°C	5.51×10^5

Table 6.1: SERS enhancement factor calculated for all samples

is expected to be the largest in both samples. The reduction in the SERS signal of S1 when annealed to 200 °C is due to larger number of Ag nanoparticles diffusing into the voids reducing the number of potential hot spot sites on the top surface. However, in S2, due to the flatness of the apex the SERS signal increases because of the reduction in the interparticle distance between the Ag nanoparticles which increases intensity of electromagnetic signals arising between them. The residual signal seen for S1 after being annealed to 500 °C is due to Ag nanoparticles diffusing down the nanowalls and retaining a reasonable interparticle distance, indicating that S1 retains its sensitivity over a much higher range of temperature compared to S2. In case of S2, the particles are too large for the voids which are very small compared to S1 and hence no SERS signal is detected. The enhancement factor was calculated for the peak at 1086 cm^{-1} which corresponds to the in-plane breathing mode coupled to the ν(C-S) mode using the method given by Yu *et al.*[237]. Enhancement factor values for all the samples are provided in Table 6.1.

We have performed SERS on two biologically relevant molecules namely Rhodamine 6G and bovine serum albumin (BSA) and the spectra are shown in Figure 6.9. While R6G is used extensively to label, detect and image biomolecules like nucleotides and proteins[260], the protein BSA constitutes a class of serum albumins used to study drug-ligand interactions[261]. The SERS modes of these molecules could be discerned at low (micro and nano) molar concentrations which makes the SERS substrate useful for potential biological applications. The SERS band assignments for R6G and BSA are provided in Table 6.2 and Table 6.3. The band assignments have been done according to those reported in the literature[258,262,263]. R6G gives strong SERS signals due to presence of highly polarizable groups. On the other hand, proteins are complex and bulky molecules which have low Raman scattering cross section. The SERS substrate was able to enhance the BSA Raman signals efficiently and we could observe SERS
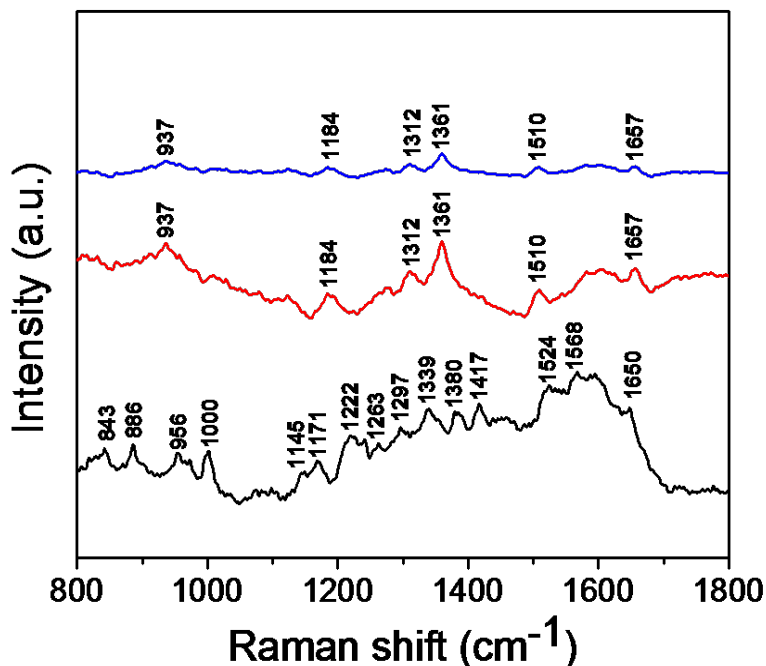
Figure 6.9: SERS spectra of bovine serum albumin (10^{-6}M, black) and Rhodamine 6G (10^{-6}M and 10^{-9}M in red and blue respectively).

Peak position (cm^{-1})	SERS band assignment
937	C_x-C_x-H bending
1184	C_x-C_x stretching
1312	C_x-H bending
1361	C_x-C_x stretching
1510	C_x-C_x stretching
1657	C_x-C_x stretching

Table 6.2: SERS band assignment for R6G

modes corresponding to the aromatic amino acids phenylalanine, tyrosine, tryptophan and histidine as well as modes from the peptide backbone and aliphatic side chains. We could also observe the amide modes which are a combination of C=O stretching combined with N-H bending vibrations[264]. The amide modes (mostly the amide I mode at around 1650 cm^{-1}) are indicative of the secondary structures of proteins and often used to elucidate different structural aspects of the proteins[249].

Peak position (cm^{-1})	SERS band assignment
843	Tyrosine
886	Tryptophan
956	Tyrosine
1000	Phenylalanine
1145	C-C stretching
1171	C-H in plane bending of Tyrosine
1222	Amide III
1263	Amide III/C-N stretch
1297	CH$_2$ deformation
1339	Tryptophan
1380	Tryptophan
1417	$\delta(CH_2)$
1524	Amide II
1568	Tryptophan, Histidine
1650	Amide I

Table 6.3: SERS band assignment for bovine serum albumin

6.4   Conclusions:

In conclusion, this chapter demonstrated Ag-GaN nanowall hybrid structure as a template for SERS studies. Apart from conventional molecules such as thiophenol and Rhodamine 6G, the template was used to sense proteins with varying surface charges which is extremely difficult for SERS substrates. FDTD simulations showed superior electromagnetic field strength at the Ag-GaN interface compared to Ag-Si while also proving the extra field strength in the nanowall configuration compared to a flat film. Tuning the size and interparticle distance between Ag was carried out on two nanowall samples with different porosity. It was seen that the nanowalls with lower porosity gave higher SERS signal compared to the structure with higher porosity. Increasing the interparticle distance by annealing, however, led to the SERS signal diminishing rapidly and at a annealing temperature of 500°C, no signal came from the sample with lower porosity. The nanowalls with higher porosity gave a good SERS response even at this temperature which was understood as the difference in the way Ag deposits on both the samples. Lower porosity nanowalls have thicker apex and Ag deposits on the top of the walls. Annealing this template initially leads to Ag diffusing across the surface and nucleating to give a marginally higher signal, but further agglomeration results in a quenching of the SERS response. For highly porous nanowalls, the Ag

nanoparticles deposit on the sidewalls as the apex regions are too narrow to allow a substantial deposition. Annealing in this case leads to diffusion on the sidewalls which is not as much as on the top of the walls and hence the SERS signal does not change by much. Even at higher annealing temperatures the only diffusion that takes place is on top regions of the walls and some Ag particles aggregate to form large clusters. The remaining Ag nanoparticles on the sidewalls still give SERS signals and hence this template is sensitive to higher temperatures.

Chapter 7

Conclusions and future directions

This chapter summarizes the thesis, giving a short description of each of the inferences drawn from the previous chapters, which are discussed briefly and conclusions drawn. Limitations of the present work are mentioned and directions for future research work in continuation of this thesis are also outlined. The work explained in this thesis concerns the fabrication and characterization of a GaN nanowall network. The nanowalls show filtering of threading dislocations which is another promising step in obtaining dislocation-free GaN template by homoepitaxial growth. Further, since nanostructuring of the surface of thin films results in the enhancement in light extraction from the semiconductor, it is an important area of research to improve LED efficiency, for which this work has made some modest contributions. The aim of this thesis is to understand how the morphology of nanowalls evolves and to compare its structural, optical and electrical properties with other nanostructures and flat films. The potential of the nanowalls in the areas of light emission and sensing applications has been particularly probed.

7.1 Growth and properties of GaN nanowall network

In this chapter, time dependent growth of GaN nanowall network has been carried out using plasma assisted molecular beam epitaxy and nanowalls grown to a height of 2 μm have been characterized to probe their structural, optical and electronic properties. At low coverages, it is interesting to understand how the morphology evolves from a rough surface to a nanowall structure. The formation of nanowalls appears to be

kinetically controlled, with the nitrogen rich conditions causing hindrance in the diffusion of Ga adatoms on the substrate surface leading to the nucleation and growth of 3-dimensional structures. 3-D nanostructural growth popularly uses the VLS mechanism, but our growth is catalyst free and the nanowall structure is self-assembled and forms spontaneously due to the growth conditions employed. The nanowalls of ZnO have also been grown by MOCVD, which has a completely different growth mechanism from MBE. However, a comprehensive understanding on the morphological evolution is lacking. In view of this, four samples with increasing coverage were grown under the previously optimized conditions for nanowall growth. The time of growth for the samples were varied from 20-80 minutes, which gave an insight into the various stages involved in the nanowall formation. The growth mechanism involved formation of individual grains between whom there is bridging, leading to the formation of a wall which grows further. However, it was also noticed that not all such walls grow continuously with time, since some did not grow to as much height as others which led to an interesting wall-within-a-wall morphology. This indicated a self assembly of the walls kinetically controlled by the growth parameters in the absence of any catalysts. Various characterizations carried out on the nanowalls revealed that the structural quality does not conform to the usual values of a flat GaN epilayer, since they possess broad PL and XRC FWHM values. Interestingly, this did not have any negative impact on the emission quality of the films, with the PL intensities increasing manifold compared to that of flat films. Additionally, the commonly found issue of yellow luminescence in GaN PL spectrum was also eliminated in the nanowall structure. Stress and strain values calculated from XRD showed that the nanowall structure was relaxed to a much higher degree than in the epilayer. There was also evidence towards there being a mix of biaxial and hydrostatic strain in the nanowalls, which is unusual for a GaN structure grown on c-sapphire substrate. A high density of band tail states were observed with large Stokes shifts which indicate the presence of trap states around the conduction band minimum. The bond strengths were deduced to be stronger in the nanowall structure from XPS data, which is in accordance with it being a more relaxed single crystalline structure. Thus, growing GaN at high temperatures in nitrogen rich conditions enables the formation of a self organized single crystalline nanowall structure that has got superior structural and optical qualities and is also strain relieved.

7.2 Transport properties and photoluminescence enhancement of GaN nanowall network

The next chapter of the thesis is concerned with probing the electron transport properties and photoluminescence enhancement of the nanowall network of GaN, which is an optolectronically potential candidate in the electronics industry since it possesses several qualities that qualify it to be an exceptional material for device fabrication. Some of its most important qualities include stability at high temperatures and the ability to work at much higher voltages and frequencies, which gives it an advantage over GaAs. In order to evaluate the nanowall network as a potential structure in electronic devices, the electron transport properties were probed. Our previous results on the same material indicated an extremely high mobility in the walls which were speculated to arise in the apex region of the structure. In order to further understand the properties, more experiments were needed to satisfactorily establish the observation. Towards that goal, more electrical measurements of the nanowalls were made which are described in the first part of this section. Nanowall networks with varying morphologies were taken and their magnetoresistance (MR), resistivity and photoconductivity (PC) were measured. Magnetoresistance in semiconductors with a single carrier type are proportional to $(1 + (\mu B)^2)$, where μ is the semiconductor mobility and B the magnetic field. Therefore, semiconductors with high electron mobility would show large magnetoresistance. In our case, it was observed that thinner nanowalls showed a more prominent MR compared to thicker ones, and it was negative. The origin of negative MR is widely accepted to be due to weak localization (WL), which provides a quantum correction to the resistivity at low temperatures. Temperature dependent measurements made on the thinner nanowall showed that the MR diminished with increasing temperature and at 3.1K, the curve becomes flat. The values of magnetic fields at which MR is observed is in the range of 0.02 T which is an order of magnitude less compared to conventional heterostructures which are used to fabricate 2 dimensional electron gas (2DEG). The next experiment performed was the measurement of resistivity of the samples using four probe method. Since the conductivity of the structure was quite high as established from Hall measurements, a

depth dependence of the same was performed by etching away the material along c-direction using chemical means and measuring resistivity at different wall heights. Two different slopes were seen in the resistance vs etching time graph which increased linearly. This was speculated to arise due to the top part of the nanowalls being more conducting compared to the bottom part. As the top part is etched away, there is slow increase in resistance, beyond which the slope is higher. The MR is present even after etching, though the rate of decrease of the conductance ratio diminishes after etching. Fitting the graph to obtain various other parameters such as mobility and phase coherence time reveals that nanowalls have a higher value of both compared to other MBE grown films. The PC spectra were recorded before and after etching the nanowalls. Etching resulted in a slower rise of the photocurrent which is indicative of increasing band tail states at the absorption edge. Based on earlier observations, the slower increase in PC was understood as due to larger defects being present near the interface compared to the top of the nanowalls.

The second part of the chapter consists of experiments conducted to improve the photoluminescence from the nanowalls. Two methods were employed in order to achieve the same; the first being nitridation of the substrate which reduces the lattice mismatch induced defects and lowers the concentration of non radiative defects in the structure, and the second being deposition of Ag to take advantage of surface plasmon coupling. Nitridation resulted in a three fold enhancement in band edge emission and structural improvement was confirmed using rocking curve measurements. Ag was deposited on two nanowall structures with different morphologies using electron beam deposition in PVD and annealing was carried out to tune the size and interparticle distance of the Ag nanoparticles. It was observed that at one particular temperature the emission increases by more than five times than that of the bare sample. Metals are known to cause both enhancement as well as quenching of luminescence in semiconductors. Further, the Ag nanoparticles in our case are well stabilized by the GaN nanowall surface with very high contact angles and hence no additional coating is required, but still the emission enhancement is stronger.

7.3   SERS studies using Ag-GaN NWN as a template

The Ag-GaN nanowall hybrid structure fabricated in the previous section also holds promise as a SERS substrate. This section describes SERS measurements performed on this Ag-GaN NWN structure using both common biomolecules as well as large proteins. Metal nanoparticles are commonly used to enhance Raman signals, and depositing Ag on GaN nanowalls forms a substrate which can detect large molecules such as proteins because of large surface area of network and the SPR coupling. Further, it has been proved that Ag-GaN nanowall hybrid is capable of detecting proteins which have pI levels in both acidic and basic regions, which has not been achieved previously. Although the enhancement factor (EF) is substantially lower than what has been reported in recent literature, due to the separation between Ag nanoparticles being as large as 5 nm, it is beneficial when sensing bigger molecules such as proteins. Changing the nanowall morphology and the Ag size and distribution also impacts the SERS results. It was observed that although thinner nanowalls show a slightly lesser EF compared to thicker nanowalls, they give SERS signals even after Ag grows to large sizes. This was understood from the way Ag deposits on different sample surfaces; on thinner walls Ag primarily sticks to the sidewalls while on the thicker walls all the Ag is on the top surfaces. At higher temperatures, there is still some Ag on the sidewalls of thinner nanowalls which gives SERS signals, but for thicker nanowalls all the Ag agglomerates into clusters on the top surface which results in a quenching of the signal.

7.4   Contributions from this Thesis work

This thesis has explored a novel three dimensional nanostructure of GaN, termed as a nanowall network, which holds potential in many important fields such as sensing and optoelectronics. The growth of GaN nanowall structure is studied using plasma-assisted molecular beam epitaxy and its various morphology dependent properties are probed using different characterization tools. Finally, an Ag-GaN nanowall hybrid structure is fabricated and its potential as a SERS biosensor is demonstrated.

- The nanowall structure of GaN has a strong band edge luminescence which can be harnessed to fabricate high emission devices.

- No catalysts are used in the growth process which makes the structure free of external contaminants.

- The nanowalls have the same property of filtering dislocations as nanowires and hence they are more relaxed and electronically stable.

- Electrical measurements are concomitant with the observations that the top surface, which is free of electrons, transports electrons more easily compared to the lower part.

- Due to the high surface area, sensing is an attractive application of nanowalls. Ag-GaN NWN has been demonstrated to be a biosensor with the unique property of being able to sense large proteins with varying pI values.

7.4.1 Limitation of the current work and future directions

The work carried out in this thesis also has its own limitations, which are discussed in this section. Possible improvements are suggested; as well as the future directions of this research work are predicted.

- In order to probe the electrical properties, proper contacts are a must for any measurement. For a porous nanowall structure, it is very difficult to make contacts and hence the results are relative at best. A possible solution to this is to fabricate contacts using PVD systems by masking the edges of the samples.

- The XRC FWHM values are very large compared to conventional flat films, the reason for which is still unclear. Nitridation and buffer layers reduce the FWHM, though it is still large. More X-ray measurements may be required to ascertain the reason behind this.

- Since the nanowalls are unintenionally n-doped and the carrier concentrations are of the order of 10^{20}, it is difficult to achieve p-doping to fabricate a device structure. Surface passivation can be tried to reduce the carrier concentrations, but actual p-doping is only possible during growth for which many experiments would be

needed.

- The observations of high mobility were not confirmed with MR, which showed fields an order of magnitude less than conventional 2DEG heterostructures. More experiments and calculations would be needed to conclusively state whether the nanowalls possess a high mobility of electrons confined to the top of the walls.

Biosensing is a good application of the Ag-GaN hybrid structure, but has low EF values. With EF values in many recently fabricated SERS substrates reaching in excess of 10^{13}, the values obtained using this substrate range in 10^5 which is quite modest in comparison. This also puts a limit on the detection efficiency of the substrate and a minimum requirement of the analyte concentration. The electromagnetic fields obtained in the vicinity of Ag nanoparticles are significantly larger than Si, but are still less in comparison to other semiconductors such as TiO_2. Thus, optimization of the nanoparticle size and position distribution and the morphology of the network have to be made to get higher performance SERS substrates.

In the field of LEDs, nanowalls are an important advantage when light extraction efficiencies (LEE) need to be increased. Fabrication of devices with nanowall surfaces which can be fabricated in such a way that scattering losses are minimized and LEE maximized is highly desirable. The filtering of dislocations by the nanowall structure also makes it an attractive candidate for growth of homoepitaxial GaN epilayers with low defect density.

The large surface area is also advantageous in solar cells apart from sensing, and fabrication of such devices using a nanowall surface can result in higher efficiency devices. Since the work described in this thesis pertains to GaN nanowalls, alloying with In and Al to give InGaN and AlGaN nanowalls can be explored which would then prove advantageous in obtaining solar cells made of purely nanowall structures. Further work on p-doping of these nanowalls is very critical to form useful device structures with high performance.

Bibliography

[1] H. P. Maruska and J. J. Tietjen. The preparation and properties of vapor-deposited single-crystal-line GaN. *Appl. Phys. Lett.*, 15:327–329, 1969.

[2] J I Pankove, E A Miller, D Richman, and J E Berkeyheiser. Electroluminescence in GaN. *J. Lumin.*, 4:63–66, 1971.

[3] H P Maruska, D A Stevenson, and J I Pankove. Violet luminescence of Mg-doped GaN. *Appl. Phys. Lett.*, 22(6):303–305, 1973.

[4] M Ilegems and R Dingle. Luminescence of Be- and Mg-doped GaN. *J. Appl. Phys.*, 44(9):4234–4235, 1973.

[5] O Lagerstedt and B Monemar. Luminescence in epitaxial GaN: Cd. *J. Appl. Phys.*, 45:2266–2272, 1974.

[6] H P Maruska and D A Stevenson. Mechanism of light production in metal-insulator-semiconductor diodes; GaN:Mg violet light-emitting diodes. *Solid. State. Electron.*, 17:1171–1179, 1974.

[7] S Yoshida, S Misawa, and S Gonda. Improvements on the electrical and luminescent properties of reactive molecular beam epitaxially grown GaN films by using AlN-coated sapphire substrates. *Appl. Phys. Lett.*, 42(5):427–429, 1983.

[8] Hiroshi Amano, N Sawaki, I Akasaki, and Y Toyoda. Metalorganic vapor phase epitaxial growth of a high quality GaN film using an AlN buffer layer. *Appl. Phys. Lett.*, 48:353, 1986.

[9] Hiroshi Amano, Masahiro Kito, Kazumasa Hiramatsu, and Isamu Akasaki. P-Type Conduction in Mg-Doped GaN Treated with Low-Energy Electron Beam Irradiation (LEEBI) . *Jpn. J. Appl. Phys.*, 28:L2112–L2114, 1989.

[10] Shuji Nakamura. GaN Growth Using GaN Buffer Layer. *Jpn. J. Appl. Phys.*, 30(10A):L1705, 1991.

[11] S Nakamura, M Senoh, and T Mukai. P-GaN / N-InGaN / N-GaN Double-Heterostructure Blue-Light-Emitting Diodes. *Jpn. J. Appl. Phys.*, 32:L8—-L11, 1993.

[12] J. F. Muth, J. H. Lee, I. K. Shmagin, R. M. Kolbas, H. C. Casey, B. P. Keller, U. K. Mishra, and S. P. DenBaars. Absorption coefficient, energy gap, exciton

binding energy, and recombination lifetime of GaN obtained from transmission measurements. *Appl. Phys. Lett.*, 71(18):2572, 1997.

[13] R Bell Zetterstrom. Synthesis and Growth of Single Crystals of Gallium Nitride. *J. Mater. Sci.*, 5:1103–1104, 1970.

[14] J Karpiski, J Jun, and S Porowski. Equilibrium pressure of N2 over GaN and high pressure solution growth of GaN. *J. Cryst. Growth*, 66:1–10, 1984.

[15] I Grzegory, J Jun, M Bockowski, and S Porowski. Crystal Growth of III-N compounds under high nitrogen pressure. *Phys. B Condens. Matter*, 185:99–102, 1993.

[16] J N Kuznia, M Asif Khan, D T Olson, Ray Kaplan, and Jamie Freitas. Influence of buffer layers on the deposition of high quality single crystal GaN over sapphire substrates. *J. Appl. Phys.*, 73(9):4700–4702, 1993.

[17] K Uchida, A Watanabe, F Yano, M Kouguchi, T Tanaka, and S Minagawa. Nitridation process of sapphire substrate surface and its effect on the growth of GaN. *J. Appl. Phys.*, 79(7):3487, 1996.

[18] S Keller, B P Keller, Y F Wu, B Heying, D Kapolnek, J S Speck, U K Mishra, and S P Denbaars. Influence of sapphire nitridation on properties of gallium nitride grown by metalorganic chemical vapor deposition. *Appl. Phys. Lett.*, 68:1525–1527, 1996.

[19] N. Grandjean, J. Massies, and M. Leroux. Nitridation of sapphire. Effect on the optical properties of GaN epitaxial overlayers. *Appl. Phys. Lett.*, 69(14):2071, 1996.

[20] O-H. Nam, M.D. Bremser, T.S. Zheleva, and R.F. Davis. Lateral epitaxy of low defect density GaN layers via organometallic vapor phase epitaxy. *Appl. Phys. Lett.*, 2638(18):2638, 1997.

[21] A. Strittmatter, S. Rodt, L. Reiß mann, D. Bimberg, H. Schröder, E. Obermeier, T. Riemann, J. Christen, and A. Krost. Maskless epitaxial lateral overgrowth of GaN layers on structured Si(111) substrates. *Appl. Phys. Lett.*, 78(111):727–729, 2001.

[22] Kazumasa Hiramatsu, Katsuya Nishiyama, Masaru Onishi, Hiromitsu Mizutani, Mitsuhisa Narukawa, Atsushi Motogaito, Hideto Miyake, Yasushi Iyechika, and Takayoshi Maeda. Fabrication and characterization of low defect density GaN

using facet-controlled epitaxial lateral overgrowth (FACELO). *J. Cryst. Growth*, 221:316–326, 2000.

[23] T.S. Zheleva, S.A. Smith, D.B. Thomson, K.J. Linthicum, P. Rajagopal, and R.F. Davis. Pendeo-epitaxy: A new approach for lateral growth of gallium nitride films. *J. Electron. Mater.*, 28(4):L5–L8, 1999.

[24] Z W Pan, Z R Dai, and Z L Wang. Nanobelts of semiconducting oxides. *Science*, 291(5510):1947–1949, 2001.

[25] Y. Inoue, T. Hoshino, S. Takeda, K. Ishino, a. Ishida, H. Fujiyasu, H. Kominami, H. Mimura, Y. Nakanishi, and S. Sakakibara. Strong luminescence from dislocation-free GaN nanopillars. *Appl. Phys. Lett.*, 85:2340–2342, 2004.

[26] R. Colby, Z. Liang, I.H. Wildeson, D.A. Ewoldt, T.D. Sands, R.E. Garcia, and E.A. Stach. Dislocation filtering in GaN nanostructures. *Nano Lett.*, 10:1568–1573, 2010.

[27] X. Duan and C.M. Lieber. Laser-Assisted Catalytic Growth of Single Crystal GaN Nanowires Herein we report the bulk synthesis of single crystalline GaN nanowires . Laser ablation of a composite target of GaN and a catalytic metal generates liquid nanoclusters that serve as reactiv. *J. Am. Chem. Soc.*, 122:188–189, 2000.

[28] Stephen D Hersee, Xinyu Sun, and Xin Wang. The controlled growth of GaN nanowires. *Nano Lett.*, 6(8):1808–1811, 2006.

[29] Maoqi He, Peizhen Zhou, S. Noor Mohammad, Gary L. Harris, Joshua B. Halpern, Randy Jacobs, Wendy L. Sarney, and Lourdes Salamanca-Riba. Growth of GaN nanowires by direct reaction of Ga with NH3. *J. Cryst. Growth*, 231(3):357–365, 2001.

[30] R Songmuang, O Landré, and B Daudin. From nucleation to growth of catalyst-free GaN nanowires on thin AlN buffer layer. *Appl. Phys. Lett.*, 91(25):251902, 2007.

[31] Yu Huang, Xiangfeng Duan, Yi Cui, and Charles M Lieber. Gallium Nitride Nanowire Nanodevices. *Nano Lett.*, 2:101–104, 2002.

[32] Paul T Blanchard, Kris A Bertness, Todd E Harvey, Lorelle M Mansfield, Aric W Sanders, and Norman A Sanford. MESFETs made from individual GaN nanowires. *IEEE Trans. Nanotechnol.*, 7(6):760–765, 2008.

[33] Song Han, Wu Jin, Daihua Zhang, Tao Tang, Chao Li, Xiaolei Liu, Zuqin Liu,

Bo Lei, and Chongwu Zhou. Photoconduction studies on GaN nanowire transistors under UV and polarized UV illumination. *Chem. Phys. Lett.*, 389:176–180, 2004.

[34] J.C. Johnson, H-J. Choi, K.P. Knutsen, R.D. Schaller, P. Yang, and R.J. Saykally. Single gallium nitride nanowire lasers. *Nat. Mater.*, 1(2):106–10, 2002.

[35] Silvija Gradečak, Fang Qian, Yat Li, Hong Gyu Park, and Charles M Lieber. GaN nanowire lasers with low lasing thresholds. *Appl. Phys. Lett.*, 87(17):173111, 2005.

[36] Heon-Jin Choi, Justin C. Johnson, Rongrui He, Sang-Kwon Lee, Franklin Kim, Peter Pauzauskie, Joshua Goldberger, Richard J. Saykally, and Peidong Yang. Self-Organized GaN Quantum Wire UV Lasers. *J. Phys. Chem. B*, 107:8721–8725, 2003.

[37] Zhaohui Zhong, Fang Qian, Deli Wang, and Charles M. Lieber. Synthesis of p-type gallium nitride nanowires for electronic and photonic nanodevices. *Nano Lett.*, 3(3):343–346, 2003.

[38] Jonathan J Wierer Jr, Qiming Li, Daniel D Koleske, Stephen R Lee, and George T Wang. III-nitride coreshell nanowire arrayed solar cells. *Nanotechnology*, 23:194007, 2012.

[39] Yong Zhang, Lin Wang Wang, and Angelo Mascarenhas. "Quantum coaxial cables" for solar energy harvesting. *Nano Lett.*, 7:1264–1269, 2007.

[40] M. Hiramatsu, K. Shiji, H. Amano, and M. Hori. Fabrication of vertically aligned carbon nanowalls using capacitively coupled plasma-enhanced chemical vapor deposition assisted by hydrogen radical injection. *Appl. Phys. Lett.*, 84(23):4708–4710, 2004.

[41] Y Wu, P Qiao, T Chong, and Z Shen. Carbon nanowalls grown by microwave plasma enhanced chemical vapor deposition. *Adv. Mater.*, 14(1):64–67, 2002.

[42] Alfred T H Chuang, John Robertson, Bojan O Boskovic, and Krzysztof K K Koziol. Three-dimensional carbon nanowall structures. *Appl. Phys. Lett.*, 90(12):123107, 2007.

[43] J Y Lao, J Y Huang, D Z Wang, Z F Ren, D Steeves, B Kimball, and W Porter. ZnO nanowalls. *Appl. Phys. A Mater. Sci. Process.*, 78(4):539–542, 2004.

[44] M Q Israr, J R Sadaf, O Nur, M Willander, S Salman, and B Danielsson. Chemically fashioned ZnO nanowalls and their potential application for potentiometric

cholesterol biosensor. *Appl. Phys. Lett.*, 98(25):253705, 2011.

[45] B Q Cao, T Matsumoto, M Matsumoto, M Higashihata, D Nakamura, and T Okada. ZnO nanowalls grown with PLD and their field emission and UV detector properties. *Pacific Rim Conf. Lasers Electro-Optics, CLEO - Tech. Dig.*, pages 10975–10980, 2009.

[46] Y D Wang, K Y Zang, S J Chua, S Tripathy, P Chen, and C G Fonstad. Nanoair-bridged lateral overgrowth of GaN on ordered nanoporous GaN template. *Appl. Phys. Lett.*, 87(25):251915, 2005.

[47] H Hartono, C B Soh, S Y Chow, S J Chua, and E A Fitzgerald. Reduction of threading dislocation density in GaN grown on strain relaxed nanoporous GaN template. *Appl. Phys. Lett.*, 90, 2007.

[48] Z. Liang, R. Gao, J-L. Lan, O. Wiranwetchayan, Q. Zhang, C. Li, and G. Cao. Growth of vertically aligned ZnO nanowalls for inverted polymer solar cells. *Sol. Energy Mater. Sol. Cells*, 117:34–40, 2013.

[49] Omid Akhavan, Elham Ghaderi, and Reza Rahighi. Toward Single-DNA Electrochemical biosensing by graphene nanowalls. *ACS Nano*, 6(4):2904–2916, 2012.

[50] S.D. Lester, F.A. Ponce, M.G. Craford, and D.A. Steigerwald. High dislocation densities in high efficiency GaN-based light-emitting diodes. *Appl. Phys. Lett.*, 66(10):1249–1251, 1995.

[51] S Chichibu, T Azuhata, T Sota, and S Nakamura. Recombination of Localized Excitons in InGaN Single- and Multi quantum-Well Structures. *MRS Proc.*, 449:14–17, 1996.

[52] S Y Karpov and Y N Makarov. Dislocation effect on light emission efficiency in gallium nitride. *Appl. Phys. Lett.*, 81(25):4721, 2002.

[53] H Marchand, J P Ibbetson, P T Fini, S Keller, S P Den Baars, J S Speck, and U K Mishra. Mechanisms of lateral epitaxial overgrowth of gallium nitride by metalorganic chemical vapor deposition. *J. Cryst. Growth*, 195:328–332, 1998.

[54] T. Gehrke, K.J. Linthicum, D.B. Thomson, P. Rajagopal, A.D. Batchelor, and R.F. Davis. Pendeo-Epitaxy of Gallium Nitride and Aluminum Nitride Films and Heterostructures on Silicon Carbide Substrate. In *Symp. G GaN Relat. Alloy.*,

volume 537 of *MRS Online Proceedings Library*, 1998.

[55] H-M. Kim, D.S. Kim, D.Y. Kim, T.W. Kang, Y-H. Cho, and K.S. Chung. Growth and characterization of single-crystal GaN nanorods by hydride vapor phase epitaxy. *Appl. Phys. Lett.*, 81(12):2193, 2002.

[56] A Kikuchi, M Kawai, M Tada, and K Kishino. InGaN/GaN Multiple Quantum Disk Nanocolumn Light-Emitting Diodes Grown on (111) Si Substrate. *Jpn. J. Appl. Phys.*, 43:L1524–L1526, 2004.

[57] T Kuykendall, P Pauzauskie, S Lee, Y Zhang, J Goldberger, and P Yang. Metalorganic chemical vapor deposition route to GaN nanowires with triangular cross sections. *Nano Lett.*, 3:1063–1066, 2003.

[58] H W Huang, C C Kao, J T Chu, W D Liang, H C Kuo, S C Wang, and C C Yu. Improvement of InGaN/GaN light emitting diode performance with a nano-roughened p-GaN surface by excimer laser-irradiation. *Mater. Chem. Phys.*, 99(5):414–417, 2006.

[59] C.F. Lin, Z.J. Yang, J.H. Zheng, and J.J. Dai. Enhanced light output in nitride-based light-emitting diodes by roughening the mesa sidewall. *IEEE Photonics Technol. Lett.*, 17(10):2038–2040, 2005.

[60] M A Mastro, B-J. Kim, Y Jung, J K Hite, C R Eddy, and J Kim. Gallium nitride light emitter on a patterned sapphire substrate for improved defectivity and light extraction efficiency. *Curr. Appl. Phys.*, 11(3):682–686, 2011.

[61] H. Kim, S-J. Park, and H. Hwang. Design and Fabrication of Highly Efficient GaN-Based Light-Emitting Diodes. *IEEE Trans. Electron Devices*, 49(10):1715–1722, 2002.

[62] K. McGroddy, A. David, E. Matioli, M. Iza, S. Nakamura, S. DenBaars, J.S. Speck, C. Weisbuch, and E.L. Hu. Directional emission control and increased light extraction in GaN photonic crystal light emitting diodes. *Appl. Phys. Lett.*, 93(10):103502, 2008.

[63] A David, T Fujii, R Sharma, K McGroddy, S Nakamura, S P DenBaars, E L Hu, C Weisbuch, and H Benisty. Photonic-crystal GaN light-emitting diodes with tailored guided modes distribution. *Appl. Phys. Lett.*, 88(6):061124, 2006.

[64] A. David, T. Fujii, B. Moran, S. Nakamura, S.P. DenBaars, C. Weisbuch, and

H. Benisty. Photonic crystal laser lift-off GaN light-emitting diodes. *Appl. Phys. Lett.*, 88(13):133514, 2006.

[65] A. David, H. Benisty, and C. Weisbuch. Optimization of light-diffracting photonic-crystals for high extraction efficiency LEDs. *IEEE/OSA J. Disp. Technol.*, 3(2):133–148, 2007.

[66] W. Han, S. Fan, Q. Li, and Y. Hu. Synthesis of Gallium Nitride Nanorods Through a Carbon Nanotube-Confined Reaction. *Science*, 277(5330):1287–1289, 1997.

[67] X. Chen, J. Li, Y. Cao, Y. Lan, H. Li, M. He, C. Wang, Z. Zhang, and Z. Qiao. Straight and smooth GaN nanowires. *Adv. Mater.*, 12(19):1432–1434, 2000.

[68] R S Wagner and W C Ellis. Vapor Liquid Solid mechanism of single crystal growth. *Appl. Phys. Lett.*, 4(5), 1964.

[69] C.-C. Chen and C.-C. Yeh. Large-Scale Catalytic Synthesis of Crystalline Gallium Nitride Nanowires. *Adv. Mater.*, 12(10):738–741, 2000.

[70] J Y Li, C G Lu, B Maynor, S M Huang, and J Liu. Controlled growth of long GaN nanowires from catalyst patterns fabricated by 'Dip-Pen' nanolithographic techniques. *Chem. Mater.*, 16(17):1633–1636, 2004.

[71] J Su, G Cui, M Gherasimova, H Tsukamoto, J Han, D Ciuparu, S Lim, L Pfefferle, Y He, A V Nurmikko, C Broadbridge, and A Lehman. Catalytic growth of group III-nitride nanowires and nanostructures by metalorganic chemical vapor deposition. *Appl. Phys. Lett.*, 86(1):013105, 2005.

[72] M S Gudiksen and C M Lieber. Diameter-selective synthesis of semiconductor nanowires. *J. Am. Chem. Soc.*, 122(36):8801–8802, 2000.

[73] A Morales and C Lieber. A laser ablation method for the synthesis of crystalline semiconductor nanowires. *Science*, 279(5348):208–211, 1998.

[74] Y Xia and P Yang. Chemistry and physics of nanowires. *Adv. Mater.*, 15(5):351–352, 2003.

[75] D K T Ng, L S Tan, and M H Hong. Synthesis of GaN nanowires on gold-coated substrates by pulsed laser ablation. *Curr. Appl. Phys.*, 6:403–406, 2006.

[76] R Calarco, R J Meijers, R K Debnath, T Stoica, E Sutter, and H Lüth. Nucleation and growth of GaN nanowires on Si(111) performed by molecular beam epitaxy. *Nano Lett.*, 7(111):2248–2251, 2007.

[77] K.A. Bertness, A. Roshko, L.M. Mansfield, T.E. Harvey, and N.A. Sanford. Nucleation conditions for catalyst-free GaN nanowires. *J. Cryst. Growth*, 300:94–99, 2007.

[78] R Meijers, T Richter, R Calarco, T Stoica, H-P Bochem, Michel Marso, and H Lüth. GaN-nanowhiskers: MBE-growth conditions and optical properties. *J. Cryst. Growth*, 289(1):381–386, 2006.

[79] E Calleja, M A Sánchez-García, F J Sánchez, F Calle, F B Naranjo, E Muñoz, U Jahn, and K Ploog. Luminescence properties and defects in GaN nanocolumns grown by molecular beam epitaxy. *Phys. Rev. B*, 62(24):16826–16834, December 2000.

[80] K A Bertness, N A Sanford, J M Barker, J B Schlager, A Roshko, A V Davydov, and I Levin. Catalyst-free growth of GaN nanowires. *J. Electron. Mater.*, 35(4):576–580, 2006.

[81] K.A. Bertness, A. Roshko, L.M. Mansfield, T.E. Harvey, and N.A. Sanford. Mechanism for spontaneous growth of GaN nanowires with molecular beam epitaxy. *J. Cryst. Growth*, 310(13):3154–3158, 2008.

[82] K A Bertness, A Roshko, N A Sanford, J M Barker, and A V Davydov. Spontaneously grown GaN and AlGaN nanowires. *J. Cryst. Growth*, 287(2):522–527, 2006.

[83] Liverios Lymperakis and Jorg Neugebauer. Large anisotropic adatom kinetics on nonpolar GaN surfaces: Consequences for surface morphologies and nanowire growth. *Phys. Rev. B*, 79(24):241308, 2009.

[84] Jelena Ristić, Enrique Calleja, Sergio Fernández-Garrido, Laurent Cerutti, Achim Trampert, Uwe Jahn, and Klaus H Ploog. On the mechanisms of spontaneous growth of III-nitride nanocolumns by plasma-assisted molecular beam epitaxy. *J. Cryst. Growth*, 310(18):4035–4045, 2008.

[85] C T Foxon, T S Cheng, N J Jeffs, J Dewsnip, L Flannery, J W Orton, I Harrison, S V Novikov, B Ya Ber, and Yu A Kudriavtsev. Studies of p-GaN grown by MBE on GaAs (111) B. *J. Cryst. Growth*, 189:516–518, 1998.

[86] R K Debnath, R Meijers, T Richter, T Stoica, R Calarco, and H Lüth. Mechanism of molecular beam epitaxy growth of GaN nanowires on Si (111). *Appl. Phys. Lett.*,

90(12):123117, 2007.

[87] M Tchernycheva, C Sartel, G Cirlin, L Travers, G Patriarche, J-C. Harmand, L S Dang, J Renard, B Gayral, L Nevou, and F Julien. Growth of GaN free-standing nanowires by plasma-assisted molecular beam epitaxy: structural and optical characterization. *Nanotechnology*, 18:385306, 2007.

[88] R Mata, K Hestroffer, J Budagosky, A Cros, C Bougerol, H Renevier, and B Daudin. Nucleation of GaN nanowires grown by plasma-assisted molecular beam epitaxy: The effect of temperature. *J. Cryst. Growth*, 334(1):177–180, 2011.

[89] J.S. Wright, W. Lim, D.P. Norton, S.J. Pearton, F. Ren, J.L. Johnson, and A. Ural. Nitride and oxide semiconductor nanostructured hydrogen gas sensors. *Semicond. Sci. Technol.*, 25:024002, 2010.

[90] B Dawoud, E Amer, and D Gross. Experimental investigation of an adsorptive thermal energy storage. *Int. J. energy Res.*, 31(2):135–147, 2007.

[91] H. T. Ng, J. Li, M.K. Smith, P. Nguyen, A. Cassell, J. Han, and M. Meyyappan. Growth of Epitaxial Nanowires at the Junctions of Nanowalls. *Science*, 300(5623):1249, 2003.

[92] J-J. Wu and C-C. Yu. Aligned TiO2 Nanorods and Nanowalls. *J. Phys. Chem. B*, 108(11):3377–3379, 2004.

[93] T Yu, Y W Zhu, X J Xu, Z X Shen, P Chen, C.-T. Lim, J.T.-L. Thong, and C.-H. Sow. Controlled Growth and Field-Emission Properties of Cobalt Oxide Nanowalls. *Adv. Mater.*, 17:1595–1599, 2005.

[94] J.Q. Qi, W.P. Chen, M. Lu, Y. Wang, H.Y. Tian, L.T. Li, and H.L.W. Chan. Fabrication of copper ferrite nanowalls on ceramic surfaces by an electrochemical method. *Nanotechnology*, 16:3097–3100, 2005.

[95] U.K. Gautam, S.R.C. Vivekchand, A. Govindaraj, and C.N.R. Rao. GaS and GaSe nanowalls and their transformation to Ga2O3 and GaN nanowalls. *Chem. Commun.*, (37):3995, 2005.

[96] X. Feng, Y. Li, H. Liu, Y. Li, S. Cui, N. Wang, L. Jiang, X. Liu, and M. Yuan. Controlled growth and field emission properties of CuS nanowalls. *Nanotechnology*, 18:145706, 2007.

[97] D Liu, Q Zhang, P Xiao, B B Garcia, Q Guo, R Champion, and G Cao.

Hydrous manganese dioxide nanowall arrays growth and their Li+ ions intercalation electrochemical properties. *Chem. Mater.*, 20(14):1376–1380, 2008.

[98] B. Varghese, M.V. Reddy, Z. Yanwu, C.S. Lit, T.C. Hoong, G.V.S. Rao, B.V.R. Chowdari, A.T. Shen Wee, C.T. Lim, and C.H. Sow. Fabrication of NiO nanowall electrodes for high performance lithium ion battery. *Chem. Mater.*, 20(4):3360–3367, 2008.

[99] S-W. Kim, H-K. Park, M-S. Yi, N-M. Park, J-H. Park, S-H. Kim, S-L. Maeng, C-J. Choi, and S-E. Moon. Epitaxial growth of ZnO nanowall networks on GaN/sapphire substrates. *Appl. Phys. Lett.*, 90(3):33107, 2007.

[100] W Xudong, D Yong, L Zhou, S Jinhui, and L W Zhong. Single-crystal mesoporous ZnO thin films composed of nanowalls. *J. Phys. Chem. C*, 113:1791–1794, 2009.

[101] C-H. Lee, Y-J. Kim, J Lee, Y J Hong, J-M. Jeon, M Kim, S Hong, and G-C. Yi. Scalable network electrical devices using ZnO nanowalls. *Nanotechnology*, 22(5):55205, 2011.

[102] B. Kumar, K.Y. Lee, H-K. Park, S.J. Chae, Y.H. Lee, and S-W. Kim. Controlled growth of semiconducting nanowire, nanowall, and hybrid nanostructures on graphene for piezoelectric nanogenerators. *ACS Nano*, 5(5):4197–204, 2011.

[103] F. Fang, D.X. Zhao, B.H. Li, Z.Z. Zhang, J.Y. Zhang, and D.Z. Shen. The enhancement of ZnO nanowalls photoconductivity induced by CdS nanoparticle modification. *Appl. Phys. Lett.*, 93:233115, 2008.

[104] L. Schmidt-Mende and J.L. MacManus-Driscoll. ZnO nanostructures, defects, and devices. *Mater. Today*, 10(5):40–48, 2007.

[105] Z Yin, N Chen, R Dai, L Liu, X Zhang, X Wang, J Wu, and C Chai. On the formation of well-aligned ZnO nanowall networks by catalyst-free thermal evaporation method. *J. Cryst. Growth*, 305:296–301, 2007.

[106] X. Zhang, X. Shan, J. Zhang, L Chen, J. Xu, L. You, and D. Yu. In situ study of epitaxial growth of ZnO nanowires at the junctions of nanowall networks on zinc particles. *Micron*, 40(3):302–307, 2009.

[107] J. Shi, S. Grutzik, and X. Wang. Zn cluster drifting effect for the formation of ZnO 3D nanoarchitecture. *ACS Nano*, 3(6):1594–1602, 2009.

[108] H.J. Fan and M. Zacharias. Manipulation of Crawling Growth for the Formation of

Sub-millimeter Long ZnO Nanowalls. *J. Mater. Sci. Technol.*, 24(4):589–593, 2009.

[109] E-S. Jang, X. Chen, J-H. Won, J-H. Chung, D-J. Jang, Y-W. Kim, and J-H. Choy. Soft-solution route to ZnO nanowall array with low threshold power density. *Appl. Phys. Lett.*, 97(4):043109, 2010.

[110] B Kumar, K-S. Shin, M-S. Yi, S Y Lee, and S-W. Kim. Synthesis of Functional ZnO Nanowall Networks Using Simple Solution Etching. *J. Nanosci. Nanotechnol.*, 14(7):5207–5211, 2014.

[111] C C Wu, D S Wuu, T N Chen, T E Yu, P R Lin, R H Horng, and S Sun. Characteristics of ZnO Nanowall Structures Grown on GaN Template Using Organometallic Chemical Vapor Deposition. *J. Nanosci. Nanotechnol.*, 8(8):3851–3856, 2008.

[112] X.H. Zhang, Y.C. Liu, X.H. Wang, S.J. Chen, G.R. Wang, J.Y. Zhang, Y.M. Lu, D.Z. Shen, and X.W. Fan. Structural properties and photoluminescence of ZnO nanowalls prepared by two-step growth with oxygen-plasma-assisted molecular beam epitaxy. *J. Phys. Condens. Matter*, 17(19):3035–3042, 2005.

[113] B.Q. Cao, T. Matsumoto, M. Matsumoto, M. Higashihata, D. Nakamura, and T. Okada. ZnO nanowalls grown with high-pressure PLD and their applications as field emitters and UV detectors. *J. Phys. Chem. C*, 113:10975–10980, 2009.

[114] N H Alvi, S M Usman Ali, S Hussain, O Nur, and M Willander. Fabrication and comparative optical characterization of n-ZnO nanostructures (nanowalls, nanorods, nanoflowers and nanotubes)/p-GaN white-light-emitting diodes. *Scr. Mater.*, 64(8):697–700, 2011.

[115] A. Zhong and K. Hane. Growth of GaN nanowall network on Si (111) substrate by molecular beam epitaxy. *Nanoscale Res. Lett.*, 7(1):686, 2012.

[116] A. Zhong and K. Hane. Characterization of GaN Nanowall Network and Optical Property of InGaN / GaN Quantum Wells by Molecular Beam Epitaxy Characterization of GaN Nanowall Network and Optical Property of InGaN / GaN Quantum Wells by Molecular Beam Epitaxy. *Jpn. J. Appl. Phys.*, 13:08JE13, 2013.

[117] D. Poppitz, A. Lotnyk, J.W. Gerlach, and B. Rauschenbach. Microstructure of porous gallium nitride nanowall networks. *Acta Mater.*, 65:98–105, 2014.

[118] M. Kesaria, S. Shetty, and S.M. Shivaprasad. Evidence for Dislocation Induced

Spontaneous Formation of GaN Nanowalls and Nanocolumns on Bare C-Plane Sapphire. *Cryst. Growth Des.*, 11(11):4900–4903, 2011.

[119] M Kesaria and S M Shivaprasad. Nitrogen flux induced GaN nanostructure nucleation at misfit dislocations on Al2O3(0001). *Appl. Phys. Lett.*, 99(14):143105, 2011.

[120] V. Popa, I. Tiginyanu, O. Volciuc, A. Sarua, M. Kuball, and P. Heard. Fabrication of GaN nanowalls and nanowires using surface charge lithography. *Mater. Lett.*, 62:4576–4578, 2008.

[121] M. M. Brewster, M-Y. Lu, S. K. Lim, M. J. Smith, X. Zhou, and S. Grade. The Growth and Optical Properties of ZnO Nanowalls. *J. Phys. Chem. Lett.*, 2:1940–1945, 2011.

[122] T L Williamson, D J Daz, P W Bohn, and R J Molnar. Structureproperty relationships in porous GaN generated by Pt-assisted electroless etching studied by Raman spectroscopy. *J. Vac. Sci. Technol. B Microelectron. Nanom. Struct.*, 22(3):925, 2004.

[123] Younan Xia, Yujie Xiong, Byungkwon Lim, and Sara E Skrabalak. Cover Picture: Shape-Controlled Synthesis of Metal Nanocrystals: Simple Chemistry Meets Complex Physics? (Angew. Chem. Int. Ed. 1/2009). *Angew. Chemie Int. Ed.*, 48(1):1, 2009.

[124] Song Jin, Matthew J Bierman, and Stephen A Morin. A New Twist on Nanowire Formation: Screw-Dislocation-Driven Growth of Nanowires and Nanotubes. *J. Phys. Chem. Lett.*, 1(9):1472–1480, 2010.

[125] W. K. Burton, N. Cabrera, and F. C. Frank. The Growth of Crystals and the Equilibrium Structure of their Surfaces. *Philos. Trans. R. Soc. A Math. Phys. Eng. Sci.*, 243:299–358, 1951.

[126] I V Markov. Crystal growth for beginners. ed, 1995.

[127] Josiah Willard Gibbs. On the equilibrium of heterogeneous substances. *Am. J. Sci.*, (96):441–458, 1878.

[128] Matthew J Bierman, Y K Albert Lau, Alexander V Kvit, Andrew L Schmitt, and Song Jin. Dislocation-driven nanowire growth and Eshelby twist. *Science*, 320(5879):1060–1063, 2008.

[129] Y K Albert Lau, Davin J Chernak, Matthew J Bierman, and Song Jin. Formation of PbS nanowire pine trees driven by screw dislocations. *J. Am. Chem. Soc.*, 131(45):16461–16471, 2009.

[130] Stephen A Morin, Matthew J Bierman, Jonathan Tong, and Song Jin. Mechanism and kinetics of spontaneous nanotube growth driven by screw dislocations. *Science*, 328(5977):476–480, 2010.

[131] Stephen A Morin and Song Jin. Screw dislocation-driven epitaxial solution growth of ZnO nanowires seeded by dislocations in GaN substrates. *Nano Lett.*, 10(9):3459–3463, 2010.

[132] Fei Meng, Stephen A Morin, and Song Jin. Rational solution growth of α-FeOOH nanowires driven by screw dislocations and their conversion to α-Fe2O3 nanowires. *J. Am. Chem. Soc.*, 133(22):8408–8411, 2011.

[133] Stephen A Morin, Audrey Forticaux, Matthew J Bierman, and Song Jin. Screw dislocation-driven growth of two-dimensional nanoplates. *Nano Lett.*, 11(10):4449–4455, 2011.

[134] James D Plummer. *Silicon VLSI technology: fundamentals, practice, and modeling.* Pearson Education India, 2000.

[135] M Cardona. Topics in Applied Physics Vol. 50, Light Scattering in Solids II, ed. by M. Cardona and G. Giintherodt, 1982.

[136] R Loudon. The Raman effect in crystals. *Adv. Phys.*, 13(52):423–482, 1964.

[137] V Yu Davydov, N S Averkiev, I N Goncharuk, D K Nelson, I P Nikitina, A S Polkovnikov, A N Smirnov, M A Jacobson, and O K Semchinova. Raman and photoluminescence studies of biaxial strain in GaN epitaxial layers grown on 6H–SiC. *J. Appl. Phys.*, 82(10):5097–5102, 1997.

[138] C. Kisielowski, J. Krüger, S. Ruvimov, T. Suski, J. W. Ager III, E Jones, Z Liliental-Weber, M Rubin, E. R. Weber, M. D. Bremser, and R. F. Davis. Strain-related phenomena in GaN thin films. *Phys. Rev. B. Condens. Matter*, 54(24):17745–17753, December 1996.

[139] Katrin Kneipp, Yang Wang, Harald Kneipp, Lev T Perelman, Irving Itzkan, Ramachandra R Dasari, and Michael S Feld. Single molecule detection using surface-enhanced Raman scattering (SERS). *Phys. Rev. Lett.*, 78(9):1667, 1997.

[140] Jon P Camden, Jon A Dieringer, Yingmin Wang, David J Masiello, Lawrence D Marks, George C Schatz, and Richard P Van Duyne. Probing the structure of single-molecule surface-enhanced Raman scattering hot spots. *J. Am. Chem. Soc.*, 130(38):12616–12617, 2008.

[141] Lasse Jensen, Christine M Aikens, and George C Schatz. Electronic structure methods for studying surface-enhanced Raman scattering. *Chem. Soc. Rev.*, 37(5):1061–1073, 2008.

[142] Paul L Stiles, Jon A Dieringer, Nilam C Shah, and Richard P Van Duyne. Surface-enhanced Raman spectroscopy. *Annu. Rev. Anal. Chem.*, 1:601–626, 2008.

[143] Adam D. McFarland, Matthew A. Young, Jon A. Dieringer, , and Richard P. Van Duyne. Wavelength-Scanned Surface-Enhanced Raman Excitation Spectroscopy. *J. Phys. Chem. B*, 109(22):11279–11285, 2005.

[144] Gerd Bergmann. Physical interpretation of weak localization: A time-of-flight experiment with conduction electrons. *Phys. Rev. B*, 28(6):2914, 1983.

[145] C V Reddy, K Balakrishnan, H Okumura, and S Yoshida. The origin of persistent photoconductivity and its relationship with yellow luminescence in molecular beam epitaxy grown undoped GaN. *Appl. Phys. Lett.*, 73:244, 1998.

[146] C Johnson, J Y Lin, H X Jiang, M Asif Khan, and C J Sun. Metastability and persistent photoconductivity in Mg-doped p-type GaN. *Appl. Phys. Lett.*, 68(13):1808–1810, 1996.

[147] J Z Li, J Y Lin, H X Jiang, A Salvador, A Botchkarev, and H Morkoc. Nature of Mg impurities in GaN. *Appl. Phys. Lett.*, 69(10):1474–1476, 1996.

[148] J Z Li, J Y Lin, H X Jiang, M Asif Khan, and Q Chen. Persistent photoconductivity in a two-dimensional electron gas system formed by an AlGaN/GaN heterostructure. *J. Appl. Phys.*, 82(3):1227–1230, 1997.

[149] G Beadie, W S Rabinovich, A E Wickenden, D D Koleske, S C Binari, and J A Freitas Jr. Persistent photoconductivity in n-type GaN. *Appl. Phys. Lett.*, 71(8):1092–1094, 1997.

[150] Michele T Hirsch, J A Wolk, W Walukiewicz, and E E Haller. Persistent photoconductivity in n-type GaN. *Appl. Phys. Lett.*, 71(8), 1997.

[151] W Rieger, R Dimitrov, D Brunner, E Rohrer, O Ambacher, and M Stutzmann.

Defect-related optical transitions in GaN. *Phys. Rev. B*, 54(24):17596, 1996.

[152] H M Chen, Y F Chen, M C Lee, and M S Feng. Yellow luminescence in n-type GaN epitaxial films. *Phys. Rev. B*, 56(11):6942, 1997.

[153] H M Chen, Y F Chen, M C Lee, and M S Feng. Persistent photoconductivity in n-type GaN. *J. Appl. Phys.*, 82(2):899–901, 1997.

[154] V V Ursaki, I M Tiginyanu, P C Ricci, A Anedda, S Hubbard, and D Pavlidis. Persistent photoconductivity and optical quenching of photocurrent in GaN layers under dual excitation. *J. Appl. Phys.*, 94(6):3875–3882, 2003.

[155] M Mynbaeva, A Titkov, A Kryganovskii, V Ratnikov, K Mynbaev, H Huhtinen, R Laiho, and V Dmitriev. Structural characterization and strain relaxation in porous GaN layers. *Appl. Phys. Lett.*, 76(9):1113, 2000.

[156] Joan J Carvajal and J Carlos Rojo. Morphology Control in As-Grown GaN Nanoporous Particles. *Cryst. Growth Des.*, 9:320–326, 2009.

[157] F K Yam and Z Hassan. Schottky diode based on porous GaN for hydrogen gas sensing application. *Appl. Surf. Sci.*, 253:9525–9528, 2007.

[158] Soumik Siddhanta, Varun Thakur, Chandrabhas Narayana, and S M Shivaprasad. Universal metal-semiconductor hybrid nanostructured SERS substrate for biosensing. *ACS Appl. Mater. Interfaces*, 4:5807–5812, 2012.

[159] A. Zhong, T. Sasaki, and K. Hane. Platinum/porous GaN nanonetwork metal-semiconductor Schottky diode for room temperature hydrogen sensor. *Sensors Actuators A Phys.*, 209:52–56, 2014.

[160] Oleksandr V Bilousov, Joan J Carvajal, Hugh Geaney, Vitaly Z Zubialevich, Peter J Parbrook, Oscar Mart, Juan Jime, D Francesc, Magdalena Aguilo, and Colm O Dwyer. Fully Porous GaN p n Junction Diodes Fabricated by Chemical Vapor Deposition. 6(20), 2014.

[161] J Lothe and J P Hirth. Dislocation Dynamics at Low Temperatures. *Phys. Rev.*, 115(3):543–550, 1959.

[162] Hee Won Seo, Seung Yong Bae, Jeunghee Park, Hyunik Yang, Kwang Soo Park, and Sangsig Kim. Strained gallium nitride nanowires. *J. Chem. Phys.*, 116(2002):9492–9499, 2002.

[163] Seung Yong Bae, Hee Won Seo, Jeunghee Park, Hyunik Yang, Hyunsuk Kim, and

Sangsig Kim. Triangular gallium nitride nanorods. *Appl. Phys. Lett.*, 82(25):4564–4566, 2003.

[164] G Kipshidze, B Yavich, A Chandolu, J Yun, V Kuryatkov, I Ahmad, D Aurongzeb, M Holtz, and H Temkin. Controlled growth of GaN nanowires by pulsed metalorganic chemical vapor deposition. *Appl. Phys. Lett.*, 86(3):33104, 2005.

[165] W.R.L.Lembrecht and B.Segall. X-ray photoelectron spectroscopy and theory of the valence band and semicore Ga 3d states in GaN. *Phys. Rev. B*, 50(19):155–160, 1994.

[166] C. I. Wu and a. Kahn. Electronic states and effective negative electron affinity at cesiated p-GaN surfaces. *J. Appl. Phys.*, 86(6):3209, 1999.

[167] S M Zhou, Y S Feng, and L D Zhang. A physical evaporation synthetic route to large-scale GaN nanowires and their dielectric properties. *Chem. Phys. Lett.*, 369(5):610–614, 2003.

[168] G Atanasova, A Og Dikovska, M Stankova, P Stefanov, and P A Atanasov. XPS study of ZnO nanostructures prepared by laser ablation. *J. Phys. Conf. Ser.*, 356:12036, 2012.

[169] D.R. Baer and M.H. Engelhard. XPS analysis of nanostructured materials and biological surfaces. *J. Electron Spectros. Relat. Phenomena*, 178-179:415–432, 2010.

[170] Sven Tougaard. Quantitative XPS : non-destructive analysis of surface. *Appl. Surf. Sci.*, 100(101), 1996.

[171] C.T. Foxon, S.V. Novikov, J.L. Hall, R.P. Campion, D. Cherns, I. Griffiths, and S. Khongphetsak. A complementary geometric model for the growth of GaN nanocolumns prepared by plasma-assisted molecular beam epitaxy. *J. Cryst. Growth*, 311(13):3423–3427, 2009.

[172] Kris A Bertness, Norman A Sanford, and Albert V Davydov. GaN Nanowires Grown by Molecular Beam Epitaxy. *IEEE J. Sel. Top. Quantum Electron.*, 17(4):847–858, 2011.

[173] U. Kaufmann, M. Kunzer, C. Merz, I. Akasaki, and H. Amano. Light Generating Carrier Recombination and Impurities in Wurtzite GaN/Al2O3 Grown by MOCVD. *MRS Proc.*, 395:633, 2011.

[174] V. A. Joshkin, C. A. Parker, S. M. Bedair, J. F. Muth, I. K. Shmagin, R. M. Kolbas,

E. L. Piner, and R. J. Molnar. Effect of growth temperature on point defect density of unintentionally doped GaN grown by metalorganic chemical vapor deposition and hydride vapor phase epitaxy. *J. Appl. Phys.*, 86(1):281, 1999.

[175] Varun Thakur, Manoj Kesaria, and S. M. Shivaprasad. Enhanced band edge luminescence from stress and defect free GaN nanowall network morphology. *Solid State Commun.*, 171:8–13, 2013.

[176] S Fischer, C Wetzel, W L Hansen, E D BourretCourchesne, B K Meyer, and E E Haller. Properties of GaN grown at high rates on sapphire and on 6HSiC. *Appl. Phys. Lett.*, 69(18), 1996.

[177] Minseo Park, J.-P. Maria, J J Cuomo, Y C Chang, J F Muth, R M Kolbas, R J Nemanich, E Carlson, and J Bumgarner. X-ray and Raman analyses of GaN produced by ultrahigh-rate magnetron sputter epitaxy. *Appl. Phys. Lett.*, 81(10), 2002.

[178] V Srikant, J S Speck, and D R Clarke. Mosaic structure in epitaxial thin films having large lattice mismatch Mosaic structure in epitaxial thin films having large lattice mismatch. *J. Appl. Phys.*, 82(9):4286–4295, 1997.

[179] H Strite, S., Morkoç. GaN, AlN, and InN: A review. *J. Vac. Sci. Technol. B*, 10(4):1237–1266, 1992.

[180] W Rieger, T Metzger, H Angerer, R Dimitrov, O Ambacher, and M Stutzmann. Influence of substrateinduced biaxial compressive stress on the optical properties of thin GaN films. *Appl. Phys. Lett.*, 68(7), 1996.

[181] V Ramesh, a. Kikuchi, K Kishino, M Funato, and Y Kawakami. Strain relaxation effect by nanotexturing InGaN/GaN multiple quantum well. *J. Appl. Phys.*, 107(11):114303, 2010.

[182] H. P. Bhasker, S. Dhar, A. Sain, Manoj Kesaria, and S. M. Shivaprasad. High electron mobility through the edge states in random networks of c-axis oriented wedge-shaped GaN nanowalls grown by molecular beam epitaxy. *Appl. Phys. Lett.*, 101(13):132109, 2012.

[183] Elias Burstein. Anomalous Optical Absorption Limit in InSb. *Phys. Rev.*, 93(3):632–633, 1954.

[184] Sejoon Lee, Youngmin Lee, and Deuk Young Kim. Residual strain effects on the

luminescence properties of self-organized GaN vertical nanorods grown by using HVPE. *J. Korean Phys. Soc.*, 62(3):518–522, 2013.

[185] Hee-sung Kang, M Siva Pratap Reddy, Dong-seok Kim, and Ki-won Kim. Effect of oxygen species on the positive flat-band voltage shift in Al 2 O 3 / GaN metal insulator semiconductor capacitors with post-deposition annealing. *J. Phys. D, Appl. Phys.*, 46(15):155101, 2013.

[186] Wei Wei, Zhixin Qin, Shunfei Fan, Zhiwei Li, Kai Shi, Qinsheng Zhu, and Guoyi Zhang. Valence band offset of β-Ga2O3/wurtzite GaN heterostructure measured by X-ray photoelectron spectroscopy. *Nanoscale Res. Lett.*, 7(1):562, 2012.

[187] S D Wolter, B P Luther, D L Waltemyer, C Onneby, S E Mohney, and R J Molnar. X-ray photoelectron spectroscopy and x-ray diffraction study of the thermal oxide on gallium nitride. *Appl. Phys. Lett.*, 70(16):2156, 1997.

[188] Nahlah Elkashef, R S Srinivasa, S Major, S C Sabharwal, and K P Muthe. Sputter deposition of gallium nitride films using a GaAs target. *Thin Solid Films*, 333(1-2):9–12, 1998.

[189] M Bellardita, M Addamo, A Di Paola, L Palmisano, and a M Venezia. Preparation of N-doped TiO(2): characterization and photocatalytic performance under UV and visible light. *Phys. Chem. Chem. Phys.*, 11(20):4084–93, 2009.

[190] N Jiang, H X Wang, H Zhang, H Sasaoka, and K Nishimura. Characterization and surface modification of carbon nanowalls. *J. Mater. Chem.*, 20(24):5070, 2010.

[191] Martin Magnuson, Maurizio Mattesini, Carina Höglund, Jens Birch, and Lars Hultman. Electronic structure of GaN and Ga investigated by soft x-ray spectroscopy and first-principles methods. *Phys. Rev. B*, 81(8):085125, 2010.

[192] T E H Walker, J Berkowitz, J L Dehmer, and J T Weber. Nonstatistical Ratios of Photoionization Cross Sections for States Split by Spin-Orbit Coupling. *Phys. Rev. Lett.*, 31(11):0–3, 1973.

[193] Y. Takakuwa S. Fujimori T. Okane Y. Ogura T. Miura S. Sato A. Kakizaki S. Kono H. W. Yeom, T. Abukawa. Anisotropy of the spin-orbit branching ratio in angle-resolved photoemission from adsorbate layers. *Surf. Sci.*, 395(2-3):L236–L241, 1998.

[194] H P Bhasker, Varun Thakur, Manoj Kesaria, S M Shivaprasad, and S Dhar. Transport and optical properties of c-axis oriented wedge shaped GaN nanowall

network grown by molecular beam epitaxy. *AIP Conf. Proc.*, 1583(1), 2014.

[195] Subhabrata Dhar and Subhasis Ghosh. Low field electron mobility in GaN. *J. Appl. Phys.*, 86(5), 1999.

[196] C W J Beenakker and H van Houten. Boundary scattering and weak localization of electrons in a magnetic field. *Phys. Rev. B*, 38(5):3232–3240, 1988.

[197] K Fuchs. The conductivity of thin metallic films according to the electron theory of metals. *Math. Proc. Cambridge Philos. Soc.*, 34(01):100–108, 1938.

[198] E H Sondheimer. The mean free path of electrons in metals. *Adv. Phys.*, 1(1):1–42, 1952.

[199] Toshiro Hiramoto, Kazuhiko Hirakawa, Yasuhiro Iye, and Toshiaki Ikoma. Phase coherence length of electron waves in narrow AlGaAs/GaAs quantum wires fabricated by focused ion beam implantation. *Appl. Phys. Lett.*, 54(21), 1989.

[200] A E Hansen, M T Björk, C Fasth, C Thelander, and L Samuelson. Spin relaxation in InAs nanowires studied by tunable weak antilocalization. *Phys. Rev. B*, 71(20):205328, 2005.

[201] R P Taylor, M L Leadbeater, G P Whittington, P C Main, L Eaves, S P Beaumont, I McIntyre, S Thoms, and C D W Wilkinson. Universal conductance fluctuations in the magnetoresistance of submicron-size n+-GaAs wires and laterally confined n-GaAs/(AlGa)As heterostructures. *Surf. Sci.*, 196(1):52–58, 1988.

[202] J J Lin and N Giordano. Electron scattering times from weak localization studies of Au-Pd films. *Phys. Rev. B*, 35(3):1071–1075, 1987.

[203] K Kornitzer, K Thonke, R Sauer, M Mayer, M Kamp, and K J Ebeling. Photocurrent and photoluminescence measurements in the near-band-edge region of 6H GaN. *J. Appl. Phys.*, 83(8), 1998.

[204] A Castaldini, A Cavallini, and L Polenta. Thickness-related features observed in GaN epitaxial layers. *Appl. Phys. Lett.*, 84(24), 2004.

[205] Michael E Levinshtein, Sergey L Rumyantsev, and Michael S Shur. *Properties of Advanced Semiconductor Materials: GaN, AIN, InN, BN, SiC, SiGe.* John Wiley & Sons, 2001.

[206] T. Fujii, Y. Gao, R. Sharma, E. L. Hu, S. P. DenBaars, and S. Nakamura. Increase in the extraction efficiency of GaN-based light-emitting diodes via surface roughening.

Appl. Phys. Lett., 84(6):855–857, 2004.

[207] G Namkoong, W A Doolittle, A S Brown, M Losurdo, P Capezzuto, and G Bruno. Role of sapphire nitridation temperature on GaN growth by plasma assisted molecular beam epitaxy: Part I. Impact of the nitridation chemistry on material characteristics. *J. Appl. Phys.*, 91(4):2499, 2002.

[208] Y. Nakada, I. Aksenov, and H. Okumura. GaN heteroepitaxial growth on silicon nitride buffer layers formed on Si (111) surfaces by plasma-assisted molecular beam epitaxy. *Appl. Phys. Lett.*, 73(6):827, 1998.

[209] T Chen, G Z Xing, Z Zhang, H Y Chen, and T Wu. Tailoring the photoluminescence of ZnO nanowires using Au nanoparticles. *Nanotechnology*, 19:435711, 2008.

[210] Koichi Okamoto, Isamu Niki, Alexander Shvartser, Yukio Narukawa, Takashi Mukai, and Axel Scherer. Surface-plasmon-enhanced light emitters based on InGaN quantum wells. *Nat. Mater.*, 3(9):601–5, 2004.

[211] Z. X. Mei, X. L. Du, Y. Wang, M. J. Ying, Z. Q. Zeng, H. Zheng, J. F. Jia, Q. K. Xue, and Z. Zhang. Controlled growth of Zn-polar ZnO epitaxial film by nitridation of sapphire substrate. *Appl. Phys. Lett.*, 86(11):112111, 2005.

[212] Benjamin Gilbert, Feng Huang, Hengzhong Zhang, Glenn A Waychunas, and Jillian F Banfield. Nanoparticles: strained and stiff. *Science*, 305(5684):651–4, 2004.

[213] H Harima. Properties of GaN and related compounds studied by means of Raman scattering. *J. Phys. Condens. Matter*, 967(14):R967, 2002.

[214] H-L. Liu, C-C. Chen, C-T. Chia, C-C. Yeh, C-H. Chen, M-Y. Yu, S Keller, and S P DenBaars. Infrared and Raman-scattering studies in single-crystalline GaN nanowires. *Chem. Phys. Lett.*, 345(3-4):245–251, 2001.

[215] I. Tiginyanu, A. Sarua, G. Irmer, J. Monecke, S. Hubbard, D. Pavlidis, and V. Valiaev. Fröhlich modes in GaN columnar nanostructures. *Phys. Rev. B*, 64(23):233317, 2001.

[216] K Jeganathan, R K Debnath, R Meijers, T Stoica, R Calarco, D Grutzmacher, and H Luth. Raman scattering of phonon-plasmon coupled modes in self-assembled GaN nanowires. *J. Appl. Phys.*, 105(12):123707, 2009.

[217] R M Feenstra and C E C Wood. *Porous Silicon Carbide and Gallium Nitride.* John

Wiley and Sons, Ltd, Chichester, UK, March 2008.

[218] Ruey-Chi Wang, Chuan-Pu Liu, Jow-Lay Huang, and Shu-Jen Chen. ZnO symmetric nanosheets integrated with nanowalls. *Appl. Phys. Lett.*, 87(5):053103, 2005.

[219] Janina Kneipp, Harald Kneipp, and Katrin Kneipp. SERS–a single-molecule and nanoscale tool for bioanalytics. *Chem. Soc. Rev.*, 37:1052–1060, 2008.

[220] Katharina Hering, Dana Cialla, Katrin Ackermann, Thomas Dörfer, Robert Möller, Henrik Schneidewind, Roland Mattheis, Wolfgang Fritzsche, Petra Rösch, and Jürgen Popp. SERS: a versatile tool in chemical and biochemical diagnostics. *Anal. Bioanal. Chem.*, 390:113–124, 2008.

[221] Katrin Kneipp, Martin Moskovits, and Harald Kneipp. *Surface-enhanced Raman scattering: physics and applications*, volume 103. Springer Science & Business Media, 2006.

[222] Ricardo Aroca. *Surface-enhanced vibrational spectroscopy*. John Wiley & Sons, 2006.

[223] Wu Yuan, Ho Pui Ho, Rebecca K Y Lee, and Siu Kai Kong. Surface-enhanced Raman scattering biosensor for DNA detection on nanoparticle island substrates. *Appl. Opt.*, 48(22):4329–4337, 2009.

[224] Ricardo Aroca and Fernando Martin. Tuning metal island films for maximum surface-enhanced Raman scattering. *J. Raman Spectrosc.*, 16(3):156–162, 1985.

[225] Roberta Brayner, Ruth Iglesias, Stéphanie Truong, Zyed Beji, Nordin Felidj, Fernand Fiévet, and Jean Aubard. Surface-Enhanced Raman Scattering on Silver Nanostructured Films Prepared by Spray-Deposition. *Langmuir*, 26(22):17465–17469, 2010.

[226] Lehui Lu, Alexander Eychmüller, Atsuko Kobayashi, Yoshiaki Hirano, Kenichi Yoshida, Yasuo Kikkawa, Keiko Tawa, and and Yukihiro Ozaki*. Designed Fabrication of Ordered Porous Au/Ag Nanostructured Films for Surface-Enhanced Raman Scattering Substrates. *Langmuir*, 22(6):2605–2609, 2006.

[227] Nicholas C Linn, Chih-Hung Sun, Ajay Arya, Peng Jiang, and Bin Jiang. Surface-enhanced Raman scattering on periodic metal nanotips with tunable sharpness. *Nanotechnology*, 20(22):225303, 2009.

[228] Hyunhyub Ko and Vladimir V Tsukruk. Nanoparticle-decorated nanocanals for surface-enhanced Raman scattering. *Small*, 4(11):1980–4, 2008.

[229] Catalina David, Nicolas Guillot, Hong Shen, Timothée Toury, and Marc Lamy de la Chapelle. SERS detection of biomolecules using lithographed nanoparticles towards a reproducible SERS biosensor. *Nanotechnology*, 21(47):475501, 2010.

[230] T Bhuvana, G V Pavan Kumar, Chandrabhas Narayana, and G U Kulkarni. Nanogranular Au films deposited on carbon covered Si substrates for enhanced optical reflectivity and Raman scattering. *Nanotechnology*, 18(14):145702, 2007.

[231] Lisa A. Dick, Adam D. McFarland, Christy L. Haynes, and and Richard P. Van Duyne*. Metal Film over Nanosphere (MFON) Electrodes for Surface-Enhanced Raman Spectroscopy (SERS): Improvements in Surface Nanostructure Stability and Suppression of Irreversible Loss. *J. Phys. Chem. B*, 106(4):853–860, 2002.

[232] A Roguska, A Kudelski, M Pisarek, M Lewandowska, M Dolata, and M Janik-Czachor. Raman investigations of TiO2 nanotube substrates covered with thin Ag or Cu deposits. *J. Raman Spectrosc.*, 40(11):1652–1656, 2009.

[233] C Noguez. Surface Plasmons on Metal Nanoparticles: The Influence of Shape and Physical Environment. *J. Phys. Chem. C*, 111:3806–3819, 2007.

[234] O J Glembocki, R W Rendell, D A Alexson, S M Prokes, A Fu, and M A Mastro. Dielectric-substrate-induced surface-enhanced Raman scattering. *Phys. Rev. B*, 80(8):85416, 2009.

[235] Lian C T Shoute, Adam Johan Bergren, Amr M Mahmoud, Ken D Harris, and Richard L McCreery. Optical Interference Effects in the Design of Substrates for Surface-Enhanced Raman Spectroscopy. *Appl. Spectrosc.*, 63(2):133–140, 2009.

[236] G V Pavan Kumar and Chandrabhas Narayana. Adapting a Fluorescence Microscope To Perform Surface Enhanced Raman Spectroscopy. *Curr. Sci.*, 93:778, 2007.

[237] Hua-Zhong Yu, Jin Zhang, Hao-Li Zhang, and and Zhong-Fan Liu. Surface-Enhanced Raman Scattering (SERS) from Azobenzene Self-Assembled Sandwiches. *Langmuir*, 15(1):16–19, 1999.

[238] Mark A Bryant, Susan L Joa, and Jeanne E Pemberton. Raman scattering from monolayer films of thiophenol and 4-mercaptopyridine at platinum surfaces.

Langmuir, 8(3):753–756, 1992.

[239] Todd L. Williamson, Xiaoying Guo, Andrew Zukoski, Aditya Sood, Diego J. Díaz, and and Paul W. Bohn. Porous GaN as a Template to Produce Surface-Enhanced Raman Scattering-Active Surfaces. *J. Phys. Chem. B*, 109(43):20186–20191, 2005.

[240] Stephen B Chaney, Saratchandra Shanmukh, Richard a. Dluhy, and Y P Zhao. Aligned silver nanorod arrays produce high sensitivity surface-enhanced Raman spectroscopy substrates. *Appl. Phys. Lett.*, 87:20–22, 2005.

[241] Steven M Asiala and Zachary D Schultz. Characterization of Hotspots in a Highly Enhancing SERS Substrate, 2011.

[242] Seung Joon Lee, Andrew R. Morrill, and and Martin Moskovits*. Hot Spots in Silver Nanowire Bundles for Surface-Enhanced Raman Spectroscopy. *J. Am. Chem. Soc.*, 128(7):2200–2201, 2006.

[243] Praveen Kumar, Mahesh Kumar, and S M Shivaprasad. (77) reconstruction as barrier for Schottky-barrier formation at the Ga/Si(111) interface. *Appl. Phys. Lett.*, 97(12), 2010.

[244] Ruijun Wang, Duo Liu, Zhiyuan Zuo, Qian Yu, Zhaobin Feng, Hong Liu, and Xiangang Xu. Surfactantless photochemical growth of Ag nanostructures on GaN epitaxial films with controlled morphologies and their application for SERS. *J. Mater. Chem.*, 22(6):2410–2418, 2012.

[245] Yugang Sun and Matthew Pelton. Laser-Driven Growth of Silver Nanoplates on p-Type GaAs Substrates and Their Surface-Enhanced Raman Scattering Activity. *J. Phys. Chem. C*, 113(15):6061–6067, 2009.

[246] Yugang Sun. Metal Nanoplates on Semiconductor Substrates. *Adv. Funct. Mater.*, 20(21):3646–3657, 2010.

[247] Xiaoying Shen, Chih-Ming Ho, and Tak-Sing Wong. Minimal Size of Coffee Ring Structure. *J. Phys. Chem. B*, 114(16):5269–5274, 2010.

[248] Xiu-Mei Lin, Yan Cui, Yan-Hui Xu, Bin Ren, and Zhong-Qun Tian. Surface-enhanced Raman spectroscopy: substrate-related issues. *Anal. Bioanal. Chem.*, 394:1729–1745, 2009.

[249] Soumik Siddhanta and Chandrabhas Narayana. Surface Enhanced Raman Spectroscopy of Proteins : Implications for Drug Designing. *Nanomater.*

Nanotechnol., 2:1–13, 2012.

[250] Zuzana Jurasekova, Giancarlo Marconi, Santiago Sanchez-Cortes, and Armida Torreggiani. Spectroscopic and molecular modeling studies on the binding of the flavonoid luteolin and human serum albumin. *Biopolymers*, 91(11):917–927, 2009.

[251] Pavol Miškovský , Daniel Jancura, Santiago Sánchez-Cortés, Eva Kočišová, and and Laurent Chinsky. Antiretrovirally Active Drug Hypericin Binds the IIA Subdomain of Human Serum Albumin: Resonance Raman and Surface-Enhanced Raman Spectroscopy Study. *J. Am. Chem. Soc.*, 120(25):6374–6379, 1998.

[252] G. V. Pavan Kumar, B. A. Ashok Reddy, Mohammed Arif, Tapas K. Kundu, and and Chandrabhas Narayana. Surface-Enhanced Raman Scattering Studies of Human Transcriptional Coactivator p300. *J. Phys. Chem. B*, 110(33):16787–16792, 2006.

[253] G V Pavan Kumar, Ruthrotha Selvi, A Hari Kishore, Tapas K Kundu, and Chandrabhas Narayana. Surface-Enhanced Raman Spectroscopic Studies of Coactivator-Associated Arginine Methyltransferase 1. *J. Phys. Chem. B*, 112(21):6703–6707, 2008.

[254] K Mantelingu, B A Ashok Reddy, V Swaminathan, A Hari Kishore, Nagadenahalli B Siddappa, G V Pavan Kumar, G Nagashankar, Nagashayana Natesh, Siddhartha Roy, Parag P Sadhale, Udaykumar Ranga, Chandrabhas Narayana, and Tapas K Kundu. Specific Inhibition of p300-HAT Alters Global Gene Expression and Represses {HIV} Replication. *Chem. Biol.*, 14(6):645–657, 2007.

[255] K. Mantelingu, A. Hari Kishore , K. Balasubramanyam, G. V. Pavan Kumar, M. Altaf, S Nanjunda Swamy, Ruthrotha Selvi, Chandrima Das, Chandrabhas Narayana, K. S. Rangappa, and and Tapas K. Kundu. Activation of p300 Histone Acetyltransferase by Small Molecules Altering Enzyme Structure: Probed by Surface-Enhanced Raman Spectroscopy. *J. Phys. Chem. B*, 111(17):4527–4534, 2007.

[256] XiaoX Han, Bing Zhao, and Yukihiro Ozaki. Surface-enhanced Raman scattering for protein detection. *Anal. Bioanal. Chem.*, 394(7):1719–1727, 2009.

[257] M A Kiselev, IuA Gryzunov, G E Dobretsov, and M N Komarova. [Size of a human

serum albumin molecule in solution]. *Biofizika*, 46(3):423–427, 2001.

[258] Edyta Podstawka, Yukihiro Ozaki, and Leonard M Proniewicz. Adsorption of S8211;S Containing Proteins on a Colloidal Silver Surface Studied by Surface-Enhanced Raman Spectroscopy. *Appl. Spectrosc.*, 58(10):1147–1156.

[259] S Stewart and P M Fredericks. Surface-enhanced Raman spectroscopy of peptides and proteins adsorbed on an electrochemically prepared silver surface. *Spectrochim. Acta Part A Mol. Biomol. Spectrosc.*, 55(78):1615–1640, 1999.

[260] Y Charles Cao, Rongchao Jin, Jwa-min Nam, C Shad Thaxton, and Chad a Mirkin. Raman-Dye-Labeled Nanoparticle Probes For Proteins. *J. Am. Chem. Soc.*, 125:14676–14677, 2003.

[261] Pavol Miskovsky, Jozef Hritz, Santiago Sanchez-cortes, Gabriela Fabriciova, Jozef Ulicny, and Laurent Chinsky. Symposium-in-Print Interaction of Hypericin with Serum Albumins : Surface-enhanced Raman Spectroscopy , Resonance Raman Spectroscopy and Molecular Modeling. *Photochem. Photobiol.*, 74:172–183, 2001.

[262] Amy M. Michaels, M. Nirmal, and L. E. Brus. Surface Enhanced Raman Spectroscopy of Individual Rhodamine 6G Molecules on Large Ag Nanocrystals. *J. Am. Chem. Soc.*, 121(16):9932–9939, 1999.

[263] Soumik Siddhanta, Dhanasekaran Karthigeyan, Partha P. Kundu, Tapas K. Kundu, and Chandrabhas Narayana. Surface enhanced Raman spectroscopy of Aurora kinases: direct, ultrasensitive detection of autophosphorylation. *RSC Adv.*, 3:4221, 2013.

[264] Andreas Barth and Christian Zscherp. What vibrations tell about proteins. *Q. Rev. Biophys.*, 35(4):369–430, 2002.

List of Publications

- **Varun Thakur**, Soumik Siddhanta, C. Narayana and S. M. Shivaprasad, *Size and distribution control of surface plasmon enhanced photoluminescence and SERS signal in Ag-GaN hybrid systems* **RSC Advances** 5, 106832, (2015).

- H. P. Bhasker, **Varun Thakur**, S. M. Shivaprasad and S. Dhar, *Role of quantum confinement in giving rise to high electron mobility in GaN nanowall networks* **Solid State Communications** 220, 72, (2015).

- H. P. Bhasker, **Varun Thakur**, S. M. Shivaprasad and S. Dhar, *Quantum coherence of electrons in random networks of c-axis oriented wedge-shaped GaN nanowalls grown by molecular beam epitaxy* **J. Phys. D: Appl. Phys.** 48, 255302, (2015).

- **Varun Thakur**, Sanjay Kumar Nayak, K. K. Nagaraja and S. M. Shivaprasad, *Improved structural quality of GaN nanowall network grown on pre-nitrided c-sapphire* **IEEE Explore** 1 (2015).

- **Varun Thakur**, Sanjay Kumar Nayak, K. K. Nagaraja and S. M. Shivaprasad, *Surface modification induced photoluminescence enhancement of GaN nanowall network grown on c-sapphire* **Electronic Materials Letters** 11, 398 (2015).

- **Varun Thakur** and S.M. Shivaprasad, *X-ray photoelectron spectroscopy analysis of bonding changes in GaN nanowall network* **Appl. Surf. Sci.** 327, 389 (2015).

- H.P. Bhaskar, **Varun Thakur**, Manoj Kesaria, S. M. Shivaprasad and S. Dhar, *Transport and optical properties of c-axis oriented wedge shaped GaN nanowall network grown by molecular beam epitaxy*, **AIP Conf. Proc.** 1583, 252 (2014).

- **Varun Thakur**, Manoj Kesaria and S.M. Shivaprasad, *Enhanced band edge luminescence in stress and defect free GaN nanowall network morphology* **Solid State Comm.** 171, 8 (2013).

- **Varun Thakur**, Soumik Siddhanta, Chandrabhas Narayana and S.M. Shivaprasad, *A universal metal-semiconductor hybrid nanostructured SERS substrate for biosensing* , **ACS Applied Materials and Interfaces** 4, 5807 (2012).